CATALYTIC STUDIES OF NOBLE METAL NANOCATALYSTS USING SINGLE-MOLECULE FLUORESCENCE MICROSCOPY

A Dissertation

Presented to the Faculty of the Graduate School

of Cornell University

In Partial Fulfillment of the Requirements for the Degree of

Doctor of Philosophy

by

Eric A Choudhary

August 2014

CATALYTIC STUDIES OF NOBLE METAL NANOCATALYSTS USING SINGLE-MOLECULE FLUORESCENCE MICROSCOPY

Eric A Choudhary, Ph. D.

Cornell University 2014

Noble metal nanoparticles are an important class of catalysts. However they are inherently heterogeneous, which makes studying them at the single-particle level desirable, as it then becomes possible to quantify these differences. A high-throughput fluorescence microscopy technique was developed in which a non-fluorescent reactant gets catalyzed to a fluorescent product on a gold catalyst surface. By recording the fluorescence signals at the single-molecule level from many particles on a camera and fitting the emitted point spread function to a two-dimensional Gaussian function, sub-diffraction spatial resolution of ~25 nm was achieved. By overlaying the optical imaging results onto a scanning electron microscopy (SEM) image of the same nanoparticles, correlation of structure and activity was achieved for individual nanoparticles. Since this technique can monitor the activity of many particles simultaneously, it was used to resolve sub-populations of both size and activity within a heterogeneous sample. This can be used to aid in future catalyst design.

Also, bimetallic catalysts made from combinations of Au, Pt, and Pd were produced in order to study the effects of a bimetallic junction on catalytic activity. By making and studying catalysts larger than the spatial resolution of this technique, it

becomes possible to resolve intraparticle activity distributions. Bimetallic segmented Au/Pt nanorods were prepared so that the catalytic activity could be mapped onto each of the domains and the interface region between the two metal domains, enabling the quantification of the effect the interface has on activity. Additionally, orthogonal, intersecting Au and Pt microstripe arrays were fabricated using photolithography to study the interface effect as well. Finally, a series of AuPd core-shell particles were synthesized using colloidal growth to study the effect of the shell thickness on catalytic activity, thus enabling the measurement of the effect of the core metal on the shell.

BIOGRAPHICAL SKETCH

Eric Choudhary grew up in Massachusetts before moving to Troy, NY to attend Rensselaer Polytechnic Institute where he received his B.S. in Chemistry with a minor in Economics in 2008. There he performed undergraduate research on chemically modifying furan monomers with Prof. James Moore and on separating conducting oligomers with interaction chromatography under Prof. Chang Ryu. He decided to work under Prof. Ryu for an additional year to earn his M.S. in 2009 where he researched the effects of high temperatures on gel permeation chromatography (GPC) for polymer analysis.

Later in 2009, he moved to Cornell University to pursue his Ph.D. with Prof. Peng Chen. There he learned how to apply single-molecule fluorescence microscopy to study catalytic behaviors on noble metal particles. In his early work he applied this technique to different sized gold nanoparticles to find the spatial limits of the method. Later he worked on synthesizing various bimetallic particles to study in order to spatially resolve catalytic activity between the different metal domains and at the interface.

Outside the lab, Eric is an avid runner. He trained with the High Noon Athletic Club on campus while at Cornell for various races ranging from the mile to the marathon.

ACKNOWLEDGMENTS

First, I would like to thank my girlfriend, Nikki, and my family for supporting and encouraging me through my time here while working towards my Ph.D. I also would like to thank all of the people at Cornell who have made my time here productive and rewarding. I want to thank my fellow class-mates for their support and for the time we spent sharing our research experiences together.

I would also like to thank the other members of the Chen group. They have helped me a countless number of times by sharing their expertise with me. Because of them, I learned how to carefully set up and conduct single-molecule microscopy experiments. They also have helped me to learn computer coding for data analysis. Finally, their friendship has made the lab enjoyable and is much appreciated.

I also want to thank my committee members, Richard Robinson and Frank Disalvo, for their conversations with me about my research; it was nice to get comments on my work from a different perspective. I'd like to thank Prof. Robinson for his help with editing my NSF IGERT proposal and for serving as my secondary advisor, and I'd like to thank Prof. Disalvo for his comments on my NRC postdoc proposal.

Finally, I would especially like to thank my thesis advisor, Peng Chen. He is the one who first got me interested in this line of research and recruited me to his group. His guidance has helped steer me through various projects. I have learned much from him about the field of heterogeneous catalysis and about being a good scientist in general.

TABLE OF CONTENTS

LIST OF FIGURES

LIST OF TABLES

CHAPTER ONE

Scalable Parallel Screening of Catalyst Activity at the Single-Particle Level and Subdiffraction Resolution[1]

1.1 Abstract

High-throughput and quantitative screening of catalyst activity is crucial for guiding the work cycles of catalyst improvements and optimizations. For nanoparticle catalysts, their inherent heterogeneity makes it desirable to screen them at the single-particle level. Here, we report a single-molecule fluorescence microscopy approach that can screen the activity quantitatively of a large number of catalyst particles in parallel at the single-particle level and with subdiffraction spatial resolution. It can identify directly high activity catalyst particles and resolve subpopulations in mixtures of catalysts. It is readily scalable and broadly applicable to heterogeneous catalysts. Using ensemble measurements to establish activity correlations between different reactions, we further show that this approach can be extended to assess catalysts in reactions that do not involve fluorescent molecules. Coupled with high throughput catalyst preparation and high-resolution structural/compositional analysis, this screening approach has promise in accelerating the development and discovery of new or better catalysts.

[1] Reprinted with permission from Zhou, X.; Choudhary, E.; Andoy, N. M.; Zou, N.; Chen, P., Scalable Parallel Screening of Catalyst Activity at the Single-Particle Level and Subdiffraction Resolution. *ACS Catalysis* **2013,** *3* (7), 1448-1453. © 2014 American Chemical Society. Author contributed by performing some of the experiments and analysis leading to the data points in Figure 1.2E and also with some of the TEM and SEM imaging.

1.2 Introduction

Nanoparticles are among the most important industrial catalysts. They can be made of many different materials, such as metals and metal oxides, and can catalyze a variety of chemical transformations. Developing better and less expensive nanoparticle catalysts remains a major goal of catalysis research. Many efforts have been directed to making nanoparticles of various morphologies and compositions. For example, advances in colloidal chemistry have made it possible to prepare nanoparticles of well-controlled size, shape, and composition, in which the shape control renders the control of surface facets.[1–5] Parallel methods[6] have also been developed that can produce nanoparticles[7] or (electro)catalysts of tremendous diversity in composition and structure for catalyzing reactions such as hydrogen oxidation,[8] thiophene oxidation,[9] fuel cell reactions,[10–15] gasoline processing,[16] and photocatalysis[17] (see also reviews 18 and 19).

Regardless of their preparation methods, precisely controlled or diversity-oriented, nanoparticle catalysts always need to be screened in reaction measurements to confirm or test their catalytic activity in various chemical transformations of interest. Here, high-throughput and quantitative methods are always desirable to quickly feed the activity information back to the next round of catalyst improvements and optimizations. To this end, thermographic imaging,[8] laser-induced resonance-enhanced multiphoton ionization,[20] fluorescence microscopy,[10,12,21,22] scanning electrochemical microscopy (SECM),[11–13,15,17] and multichannel reactor vessels[16] have been used to screen the catalyst activity in parallel.

Moreover, the activity screening of nanoparticle catalysts is preferentially done at the single-particle level because, above all, they are highly heterogeneous.[23–26] Even

for size- and shape-controlled nanocrystals, individual particles differ from one another. For diversity-orientated preparations, the catalyst heterogeneity is more pronounced. Several approaches that are capable of studying the (electro)catalytic activity of nanoparticles at the single-particle level have been developed. These include scanning probe microscopy (e.g., scanning tunneling microscopy and SECM),[27−31] detecting collision induced current transients on microelectrodes,[32−36] using single particles as electrodes,[37−40] and localized surface plasmon resonance (LSPR) microscopy.[41−46] Although powerful, each has limitations: the scanning probe approaches have low data throughput; the electrical-current-based measurements not only have low data throughput but also are limited to electrocatalysts; the LSPR microscopy is generally limited to plasmonic metal catalysts and has diffraction-limited spatial resolution (about 200−300 nm).

Single-molecule fluorescence microscopy recently has emerged as an effective approach to study catalytic reactions on individual catalyst particles.[26,47−51] In this approach, a fluorogenic reaction is used, and fluorescence microscopy is used to detect the fluorescence signal of a reaction product on immobilized catalyst particles at the single-molecule level (Figure 1.1A). Quantitative activity of single catalyst particles can be obtained readily. With sufficient fluorescence signals, the positions of individual product molecules can further be localized to nanometer precision,[52,53] allowing imaging beyond the diffraction-limited resolution to tens of nanometers (i.e., subdiffraction resolution).[50,54−64]

Here, we demonstrate that this single-molecule subdiffraction imaging approach can be scaled up to screen the activity of a large number of catalyst particles in parallel. Quantitative activity can be obtained at the single-particle level that

enables identification of high activity particles. By using activity correlations between different reactions, we further show that this approach can assess catalyst activity beyond fluorogenic reactions. Coupled with high-throughput synthetic methods of catalysts and high-resolution structural and compositional analysis, this approach has the potential to accelerate catalyst development and discovery.

1.3 Materials and Methods

Catalyst preparation/characterization, single-molecule fluorescence microscopy, ensemble activity assays, and data analysis are described in the Supporting Information (SI), sections 1.8.1− 1.8.3. All catalysis experiments were performed at room temperature in aqueous solution.

1.4 Results and Discussion

1.4.1 Single-Molecule Subdiffraction Imaging of Single-Particle Catalysis.

We first demonstrate the subdiffraction spatial resolution of our approach in imaging catalysis on single catalyst particles. To do so, we used two types of pseudospherical particles as model catalysts. One type is bare Au particles of 6−14 nm in diameter (here "bare" means that they do not have strong capping ligands such as CTAB or additional shells); the other is mesoporous silica-coated Au particles (i.e., Au@mSiO_2 particles) with variable core diameters and shell thicknesses (SI, Table S1). We used two fluorogenic reactions as our probe catalytic reactions: one a reductive N-deoxygenation of resazurin to resorufin by NH_2OH and the other an oxidative N-deacetylation of amplex red to resorufin by H_2O_2. Resorufin is a highly fluorescent molecule (Figure 1.1B). Using wide-field total-internal-reflection single-

molecule fluorescence microscopy, we imaged and localized the product molecules catalytically generated on individual particles one at a time in real time (Figure 1.1A).

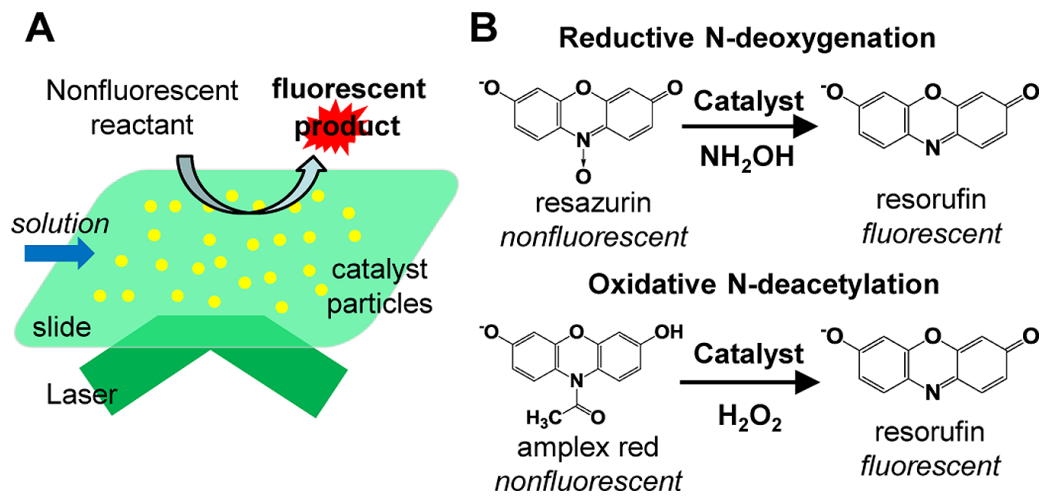

Figure 1.1 Single-molecule fluorescence microscopy of fluorogenic reactions. (A) Schematic of using wide-field total internal reflection fluorescence microscopy to image fluorogenic catalytic reactions by a large number of catalyst particles immobilized on a quartz slide. The reactant solution is supplied in a continuous flow in a microfluidic reactor, resulting in steady-state reaction kinetics. (B) The two fluorogenic probe reactions for catalysis: a reductive N-deoxygenation of resazurin to resorufin by NH_2OH, and an oxidative N-deacetylation of amplex red to resorufin by H_2O_2.

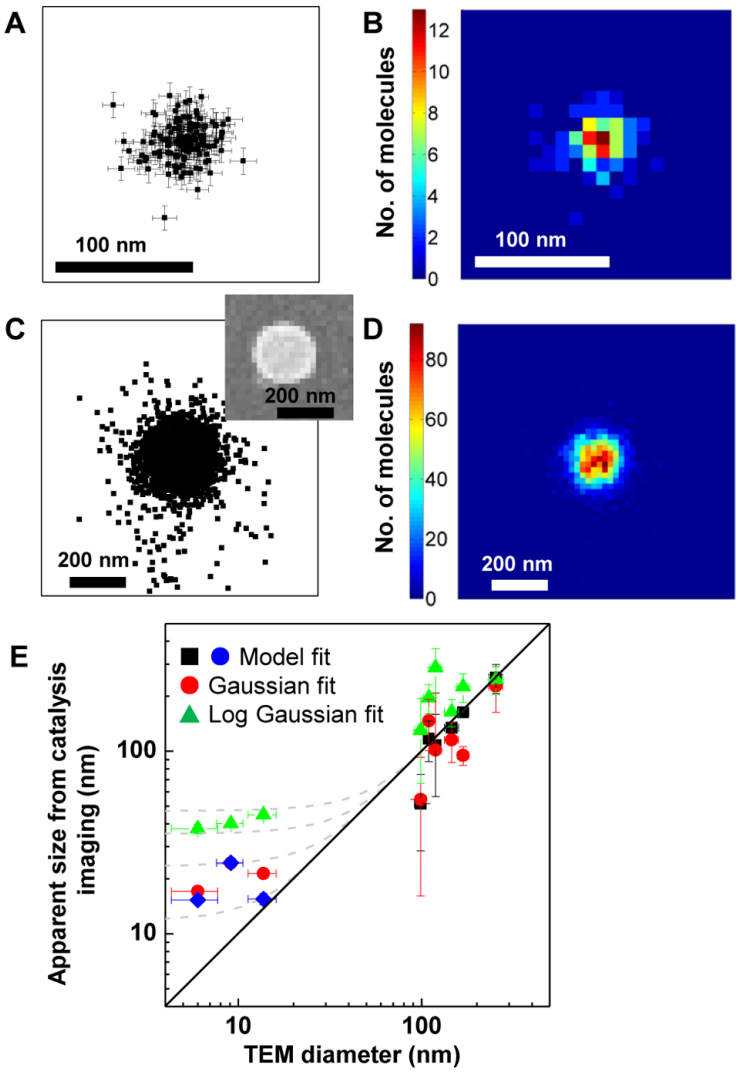

Figure 1.2 Single-molecule subdiffraction imaging of single-particle catalysis. (A) Locations of 141 product molecules from a 6-nm bare Au particle catalyzing the N-deoxygenation reaction of resazurin. (B) Image plot of the 2-D histogram of A with 10 × 10 nm^2 bin. (C, D) Same as A and B, but for a 102@33 nm (core-diameter@shellthickness) Au@mSiO_2 particle with ~4900 product molecules in catalyzing the N-deacetylation reaction of amplex red. Inset in C is the particle's SEM image. (E) Correlation between the TEM (outer) diameter and the apparent size from subdiffraction catalysis imaging over a series of catalyst samples. The apparent sizes from the subdiffraction catalysis imaging are extracted using three different methods, as described in the SI, section S4. These methods are referred to as model fit, Gaussian fit, and log Gaussian fit, respectively. Each data point is an average of many particles in one catalyst sample. The catalyst samples here include pseudospherical bare Au particles 6, 9, and 14 nm in diameter, and Au@mSiO_2 particles 42@28, 42@38, 60@25, 60@42, 60@97, and 102@33 nm in size. The four dashed lines are simulations assuming that reactions occur evenly on a spherical surface of a certain diameter; the resulting product distributions on the spheres are then projected into 2-D or 1-D and further convoluted with a Gaussian broadening function that has a standard deviation of 10, 15, 20, or 25 nm, respectively. The FWHMs of the convoluted distribution functions are then plotted here. See simulation details in the SI, section S4.1. Error bars are all standard deviations.

Figure 1.2A shows the locations of the catalytic products from a single 6-nm bare Au particle catalyzing the N-deoxygenation reaction. The fwhm of the 2-D histogram of these locations is ~30 nm (Figure 1.2B, and Figure 1.14C), which is 10 times smaller than the diffraction-limited resolution (~300 nm). Because this 2-D histogram can be plotted in an image format (i.e., Figure 1.2B), we refer to this type of plot as "subdiffraction catalysis images". Nevertheless, the object in Figure 1.2B is still larger than the physical size of the 6-nm particle, which reflects the resolution limit of our approach. Depending on the number of the detected fluorescence photons of individual catalytic products, our effective spatial resolution is ~15 nm at best, but is typically 30−40 nm when all product molecules that differ in photon counts are included in the analysis (SI, section S4). Consistent with this spatial resolution, for a pseudospherical Au@mSiO_2 particle that is significantly larger than our spatial resolution, the FWHM of the 2-D histogram of its product locations is about the same as its physical size (Figure 1.2C, D).

Knowing the effective spatial resolution of our approach, we used three analysis methods to extract the apparent sizes of individual catalyst particles from their subdiffraction catalysis images over a series of Au and Au@mSiO_2 particles. One method involves fitting the data with a model; the other two use empirical fittings (details in the SI, section 1.8.4). Figure 1.2E plots the apparent sizes of these particles from the subdiffraction catalysis imaging against their diameters determined from TEM. For larger particles, their apparent sizes are about the same as their true physical sizes. With decreasing particle size to smaller than 30−40 nm, the apparent sizes from subdiffraction catalysis imaging deviate toward the larger side of the true sizes and

eventually flatten out to a limiting value, which reflects our approach's resolution limit. Overall, these results demonstrate that we can image the catalysis of individual catalyst particles at tens of nanometer resolution, that is, subdiffraction resolution.

1.4.2 Screening Mixtures of Pseudo-spherical Au@mSiO$_2$ Particles

To demonstrate that our approach is capable of screening and differentiating the activities of a large number of catalyst particles in parallel, we applied it to a mixture of 21@ 42 nm and 102@32 nm pseudospherical Au@mSiO$_2$ particles (Table 1.1). Figure 1.3A presents the subdiffraction catalysis image of ~1000 particles on a slide in catalyzing the N-deoxygenation reaction, alongside the SEM image of the same sample (Figure 1.3B). Individual particles are clearly resolved in the subdiffraction catalysis image, including those within aggregates (Figure 1.3A, inset). More important, this subdiffraction catalysis image immediately reports the activities of individual particles, quantified by the number of product molecules detected on them. For example, particle 1 is clearly more active than particle 2 because it generated more product molecules during the same reaction time (Figure 1.3A inset), even though the two particles are similar in size (Figure 1.3B, inset). Overall, large heterogeneity in activity is clear among individual particles, which corroborates the need for single particle level screening.

Pooling the results from many particles together, we obtained the distributions of their sizes and activities (Figure 1.3C, D and the SI, section S5). Here, the activities are represented by v, the rate of turnovers per particle. We also excluded the aggregates in these distributions for convenience in automated data analysis. Two subpopulations are clear in the 2-D histogram of size and activity, corresponding to

the 21@42 nm and 102@32 nm Au@mSiO$_2$ particles (Figure 1.3D). The larger 102@32 nm particles have higher activity, likely due to their larger Au surface areas per particle.

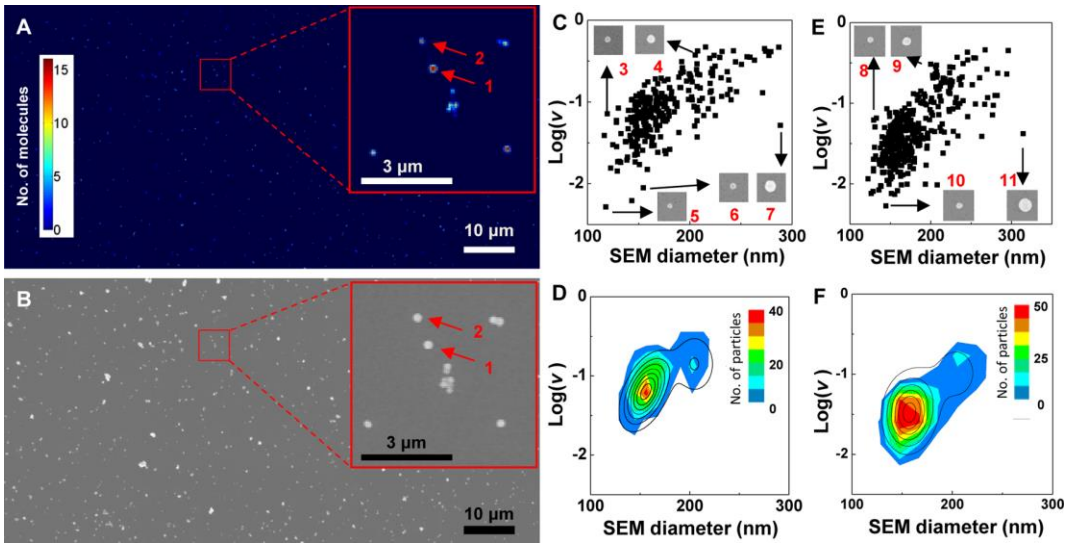

Figure 1.3 Parallel activity screening of a mixture of pseudospherical 21@42 nm and 102@32 nm Au@mSiO$_2$ particles. (A) Subdiffraction catalysis image of ~1000 particles in catalyzing the reductive N-deoxygenation of resazurin to resorufin. This image is generated with 20 × 20 nm^2 bins. Inset: a zoom-in. Reaction conditions in the SI, section S5. (B) SEM image of the same set of particles as in A with a zoom-in inset. (C) Scatter plot of individual catalyst particles against their respective SEM diameters and rates of turnovers (v, in s^{-1} particle^{-1} in log scale) from A and B. Each point represents one particle. Insets: SEM images of selected particles. (D) Contour plot of the 2-D histogram of C. Bin size: 20 nm ×0.25. The solid black lines are fits with two 2-D Gaussian functions. (E, F) Same as C and D , but for a different batch of samples in catalyzing the oxidative Ndeacetylation of amplex red to resorufin. Reaction conditions are in the SI, section S6.

Among all particles in this mixture, the general trend is, unsurprisingly, that larger particles are more active on a perparticle basis, with a Pearson's correlation coefficient of ~0.68 between size and activity (Figure 1.3C). However, some smaller particles show significantly higher activities (e.g., particle 3, Figure 1.3C), whereas some larger ones show lower activities (e.g., particle 7, Figure 1.3C), compared with those of similar sizes. This direct identification of catalyst activity at the singleparticle level is exciting because one can now pinpoint the particle of desired activity for

subsequent structural characterizations, although our structural characterization is currently just at the SEM level, which is insufficient to identify the structural basis of activity differences (Figure 1.3C insets).

We also examined this mixture of the two types of Au@mSiO_2 particles in catalyzing the N-deacetylation reaction. We again were able to screen and quantify the activity of a large number of particles in parallel at the single-particle level and subdiffraction resolution, as well as resolve their subpopulations (Figure 1.3E, F, and the SI, section S6).

1.4.3 Screening Mixtures of Different-Shaped Catalyst Particles

Here, we demonstrate that our approach can screen and differentiate the activity of not only mixtures of different sized catalyst particles, but also mixtures of different-shaped ones. We used a mixture of Au@mSiO_2 particles with pseudospherical, triangular, and rod-shaped Au cores as our model catalysts (Figure 1.8) in catalyzing the Ndeacetylation reaction of amplex red. Because of the mSiO_2 shell, those with small triangular cores are difficult to distinguish by shape in SEM from those with pseudospherical cores. We thus grouped them together as "pseudo-spherical" particles that have two subpopulations differing in size (outer diameter: 158.3 ± 47.0 nm and 243.3 ± 44.5 nm; the larger ones are those with triangular cores; Figure 1.30B). The Au@mSiO_2 rods are ~160 nm in outer diameter and have outer lengths ranging from ~260 to ~860 nm, as we previously reported[62] (Figure 1.30A).

Figure 1.4A shows the subdiffraction catalysis image of ~900 of these differently shaped catalyst particles, alongside the SEM image of the same sample (Figure 1.4B). Individual catalyst particles, as well as their pseudosphere or rod

shapes, are clearly resolved in the subdiffraction catalysis image, even within aggregates. Again, the most important information from the subdiffraction catalysis image is the catalytic activities of individual particles, reflected by the number of reaction products detected on them. A large heterogeneity of activity is clear among particles: even for those of similar sizes, some are more active and some less (e.g., particle 12 vs particle 13 in Figure 1.4A inset). This large activity heterogeneity again corroborates the need for single-particle level activity screening.

We further analyzed the pseudospherical and rod-shaped particles separately. Figure 1.4C shows the distribution of size and activity of the pseudospherical catalyst particles (we again excluded those in aggregates for convenience in data analysis; see also section 1.8.7). Two subpopulations are clearly resolved in the distribution, with the larger particles having higher activities on a per-particle basis. Figure 1.4D shows the correlation between activity and aspect ratio of individual rods. Here, no clear subpopulations are visible, although large activity heterogeneity is apparent. This direct identification of catalyst activity at the single-particle level again allows us to pinpoint specific particles of high or low activity, for example, those in the Figure 1.4D insets.

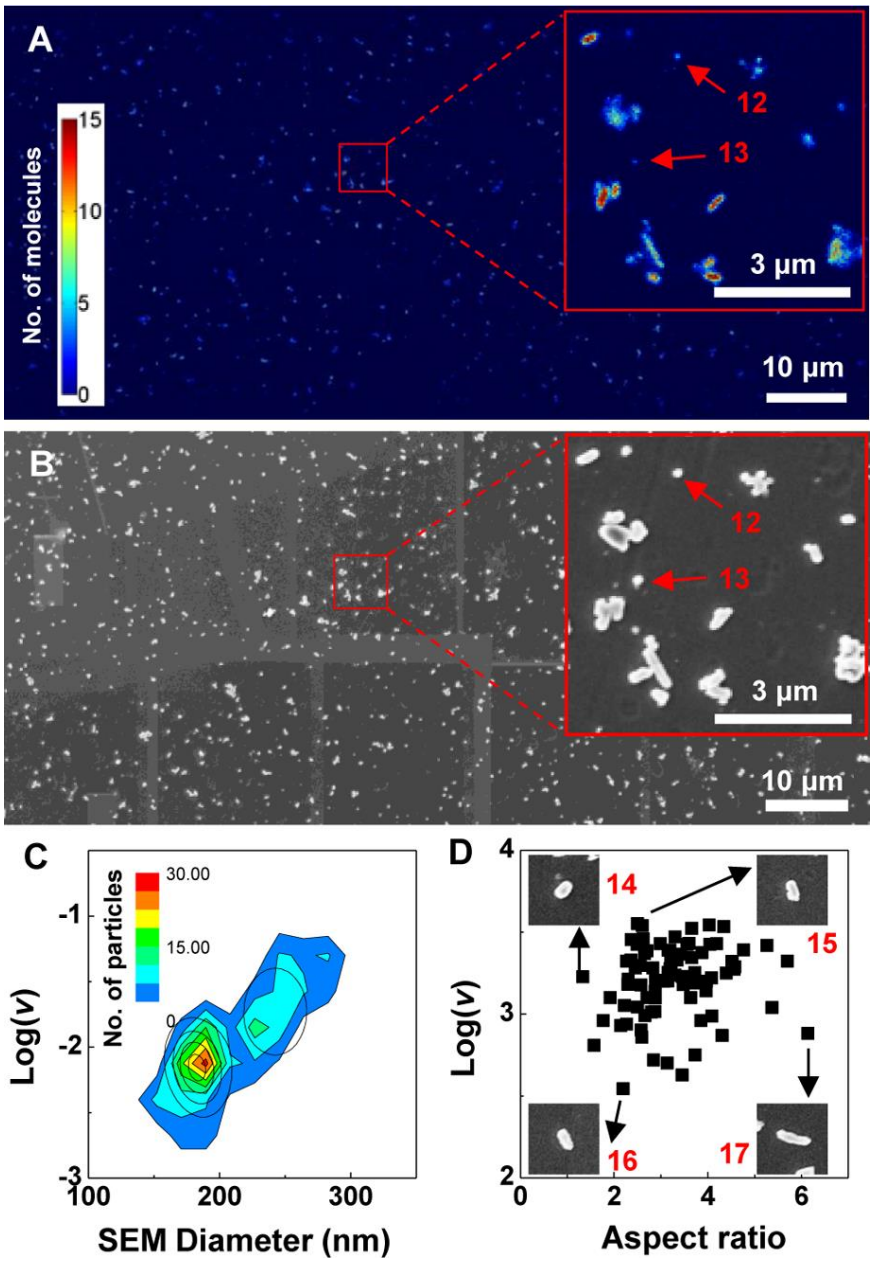

Figure 1.4 Parallel activity screening of a mixture of pseudospherical and rod-shaped Au@mSiO_2 particles in catalyzing the oxidative Ndeacetylation of amplex red to resorufin. Reaction conditions are in the SI, section 1.8.7. (A) Subdiffraction catalysis image of ~900 particles with a zoom-in inset. Image generated with 20 × 20 nm^2 bins. (B) SEM image of the same set of particles as in A with a zoom-in inset. (C) Contour plot of the 2-D histogram of ~220 pseudospherical particles against their respective SEM diameters and rates of turnovers (v, in s^{-1} $particle^{-1}$ in log scale) from A and B. Bin size: 20 nm ×0.25. The solid black lines are fits with two 2-D Gaussian functions (also Figure 1.31 and section 1.8.7). (D) Scatter plot of ~80 rods from A and B against their respective aspect ratios (from SEM image) and log(v). Insets: SEM images of selected rods.

1.4.4 Activity Correlation between Fluorogenic Probe Reactions and Common Model Redox Reactions

For our imaging approach, one of the catalytic products needs to be fluorescent. Therefore, catalytic reactions that do not generate fluorescent molecules cannot be studied directly. However, the types of chemical transformations to be studied are not limited because one can design reactant molecules that undergo the desired chemical transformation to generate a fluorescent molecule. For example, the two fluorogenic probe reactions we use here represent distinct chemical transformations: one an N-deacetylation reaction and the other an N-deoxygenation reaction (Figure 1.1B).

On the other hand, one may not even need to design new fluorogenic reactions for screening catalysts for a particular chemical transformation. Our hypothesis is the following: If a catalyst's activity in a reaction of interest is well correlated with its activity in either of the two fluorogenic probe reactions we study here, then our fluorescence microscopy-based screening results can be used to predict the (relative) activity of catalyst particles in the reaction of interest. Here, we demonstrate such activity correlations between the two fluorogenic probe reactions and two common model reactions for studying catalysts.

The two model reactions we chose are the reduction of 4-nitrophenol to 4-aminophenol and the oxidation of hydroquinone to quinone (Figure 1.34 and section 1.8.8). Both are commonly used to test the activity of catalysts.[65] We tested two series of catalysts: one bare pseudospherical Au particles and the other pseudospherical Au@mSiO_2 particles, both of varying sizes (Table 1.1). Figure 1.5A shows the

correlation between the activities of these catalysts in 4-nitrophenol reduction and in resazurin N-deoxygenation. Figure 1.5B shows the correlation between their activities in hydroquinone oxidation and in amplex red N-deacetylation. In both cases, linear positive correlation is observed: when a catalyst is high in activity in the reductive N-deoxygenation reaction of resazurin, it is also high in activity in the 4-nitrophenol reduction reaction, and when a catalyst is high in activity in the oxidative N-deacetylation reaction of amplex red, it is also high in activity in the hydroquinone oxidation reaction. The correlation coefficients are all ~1.0, even though the activities of the catalyst particles vary over many orders of magnitude. These correlations demonstrate that for the 4-nitrophenol reduction and hydroquinone oxidation reactions, even though we cannot directly screen the catalyst activities using our single-molecule imaging approach, we can still screen them at the single-particle level using our fluorogenic probe reactions to obtain equivalent information. This correlation approach can be broadly applied to many other catalytic reactions; one just needs to establish their correlations with a fluorogenic reaction using conventional ensemble measurements before applying the single-molecule fluorescence microscopy approach for activity screening at the single-particle level.

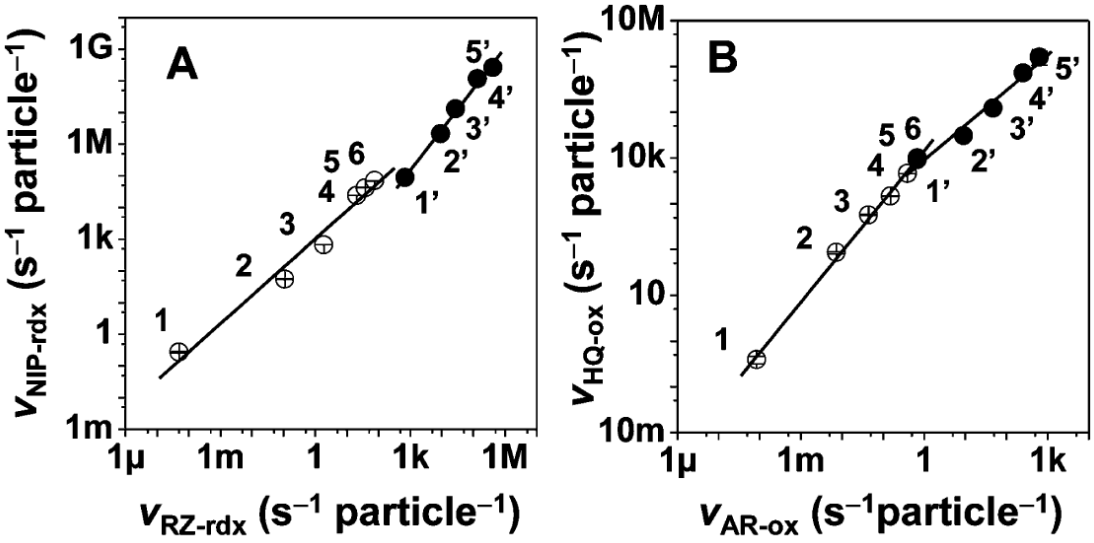

Figure 1.5 Activity correlation for the same sets of catalyst particles between different reactions. (A) Correlation between the reductive Ndeoxygenation reaction of resazurin (i.e., RZ-rdx) and the reduction of 4-nitrophenol (i.e., NIP-rdx). For bare Au particles, the correlation coefficient is $\rho \sim 1.00$; for Au@mSiO_2 particles, $\rho \sim 0.99$. (B) Correlation between the oxidative N-deacetylation reaction of amplex red (i.e., AR-ox) and the oxidation of hydroquinone (i.e., HQ-ox). For bare Au particles, $\rho \sim 0.98$; for Au@mSiO_2 particles, $\rho \sim$ 1.00. All error bars are standard deviations. Solid lines are linear fits. The activities were measured at the ensemble level and quantified by the rate of turnovers, v, in s−1 particle−1. Two series of catalyst particles were tested (SI, Table S1): one (●), bare pseudospherical Au particles 6, 9, 21, 102, and 226 nm in diameter, denoted as 1′, 2′, 3′, 4′, and 5′; the other (○), pseudospherical Au@mSiO_2 particles of 6@38, 21@81, 42@65, 42@70, 60@83, 102@59 nm in size, denoted as 1, 2, 3, 4, 5, and 6, in the plots.

1.5 Conclusion

We have shown here that the single-molecule fluorescence microscopy approach offers a quantitative way to screen the activity of a large number of catalyst particles in parallel at the single-particle level and subdiffraction resolution. This approach is applicable to many types of (nano)catalysts, and the results can be extrapolated using activity correlations to evaluate catalyst activity beyond fluorogenic reactions. With motorized fluorescence microscopes and larger camera formats, this

approach can be scaled up significantly to identify highly active ones among many thousands of catalyst particles, which can then be selected for subsequent high-resolution structural and compositional analysis, for example, using high-resolution electron microscopy.[66] Coupled with combinatorial or parallel synthesis of catalysts,[6–12,16,17] one can envision that this approach will be powerful for assessing catalyst synthesis protocols and the performance of resulting catalysts. The information can then be fed back quickly to the next round of catalyst synthesis and optimization, which would accelerate the discovery and development of new or better catalysts.

1.7 References

(1) Habas, S. E.; Lee, H.; Radmilovic, V.; Somorjai, G. A.; Yang, P.: Shaping binary metal nanocrystals through epitaxial seeded growth. *Nat Mater* **2007**, *6*, 692-7.

(2) Ahmadi, T. S.; Wang, Z. L.; Green, T. C.; Henglein, A.; El-Sayed, M. A.: Shape-Controlled Synthesis of Colloidal Platinum Nanoparticles. *Science* **1996**, *272*, 1924-1925.

(3) Sun, Y.; Xia, Y.: Shape-Controlled Synthesis of Gold and Silver Nanoparticles. *Science* **2002**, *298*, 2176-2179.

(4) Millstone, J. E.; Hurst, S. J.; Métraux, G. S.; Cutler, J. I.; Mirkin, C. A.: Colloidal Gold and Silver Triangular Nanoprisms. *Small* **2009**, *5*, 646-664.

(5) Murphy, C. J., Thompson, Lucas B., Chernak, Davin J., Yang, Jie An, Sivapalan, Sean T., Boulos, Stefano P., Huang, Jingyu, Alkilany, Alaaldin M., Sisco, Patrick N. : Gold nanorod crystal growth: From seed-mediated synthesis to nanoscale sculpting. *Current Opinion in Colloid & Interface Science* **2011**, *16*.

(6) Hanak, J. J.: The "multiple-sample concept" in materials research: Synthesis, compositional analysis and testing of entire multicomponent systems. *J Mater Sci* **1970**, *5*, 964-971.

(7) Salaita, K.; Wang, Y.; Fragala, J.; Vega, R. A.; Liu, C.; Mirkin, C. A.: Massively Parallel Dip–Pen Nanolithography with 55 000-Pen Two-Dimensional Arrays. *Angewandte Chemie International Edition* **2006**, *45*, 7220-7223.

(8) Moates, F. C.; Somani, M.; Annamalai, J.; Richardson, J. T.; Luss, D.; Willson, R. C.: Infrared Thermographic Screening of Combinatorial Libraries of Heterogeneous Catalysts. *Industrial & Engineering Chemistry Research* **1996**, *35*, 4801-4803.

(9) Gall, R. D.; Hill, C. L.; Walker, J. E.: Selective Oxidation of Thioether Mustard (HD) Analogs bytert-Butylhydroperoxide Catalyzed by $H_5PV_2Mo_{10}O_{40}$ Supported on Porous Carbon Materials. *Journal of Catalysis* **1996**, *159*, 473-478.

(10) Reddington, E.; Sapienza, A.; Gurau, B.; Viswanathan, R.; Sarangapani, S.; Smotkin, E. S.; Mallouk, T. E.: Combinatorial Electrochemistry: A Highly Parallel, Optical Screening Method for Discovery of Better Electrocatalysts. *Science* **1998**, *280*, 1735-1737.

(11) Fernández, J. L.; Walsh, D. A.; Bard, A. J.: Thermodynamic Guidelines for the Design of Bimetallic Catalysts for Oxygen Electroreduction and Rapid Screening by Scanning Electrochemical Microscopy. M−Co (M: Pd, Ag, Au). *J Am Chem Soc* **2004**, *127*, 357-365.

(12) Prochaska, M.; Jin, J.; Rochefort, D.; Zhuang, L.; DiSalvo, F. J.; Abruña, H. D.; van Dover, R. B.: High throughput screening of electrocatalysts for fuel cell applications. *Review of Scientific Instruments* **2006**, *77*, 054104.

(13) Jin, J.; Prochaska, M.; Rochefort, D.; Kim, D. K.; Zhuang, L.; DiSalvo, F. J.; van

Dover, R. B.; Abruña, H. D.: A high-throughput search for direct methanol fuel cell anode electrocatalysts of type PtxBiyPbz. *Applied Surface Science* **2007**, *254*, 653-661.

(14) Abruna, H., D.; Matsumoto, F.; Cohen, J. L.; Jin, J.; Roychowdhury, C.; Prochaska, M.; van Dover, R. B.; DiSalvo, F. J.; Kiya, Y.; Henderson, J. C.; Hutchison, G. R.: Electrochemical Energy Generation and Storage. Fuel Cells and Lithium-Ion Batteries. *Bulletin of the Chemical Society of Japan* **2007**, *80*, 1843-1855.

(15) Gregoire, J. M.; Kostylev, M.; Tague, M. E.; Mutolo, P. F.; van Dover, R. B.; DiSalvo, F. J.; Abruña, H. D.: High-Throughput Evaluation of Dealloyed Pt–Zn Composition-Spread Thin Film for Methanol-Oxidation Catalysis. *Journal of The Electrochemical Society* **2009**, *156*, B160-B166.

(16) Turner, H. W.; Volpe Jr, A. F.; Weinberg, W. H.: High-throughput heterogeneous catalyst research. *Surface Science* **2009**, *603*, 1763-1769.

(17) Jang, J. S.; Lee, J.; Ye, H.; Fan, F.-R. F.; Bard, A. J.: Rapid Screening of Effective Dopants for Fe_2O_3 Photocatalysts with Scanning Electrochemical Microscopy and Investigation of Their Photoelectrochemical Properties. *The Journal of Physical Chemistry C* **2009**, *113*, 6719-6724.

(18) Weinberg, W. H.; Jandeleit, B.; Self, K.; Turner, H.: Combinatorial methods in homogeneous and heterogeneous catalysis. *Current Opinion in Solid State and Materials Science* **1998**, *3*, 104-110.

(19) McFarland, E. W.; Weinberg, W. H.: Combinatorial approaches to materials discovery. *Trends in Biotechnology* **1999**, *17*, 107-115.

(20) Senkan, S. M.: High-throughput screening of solid-state catalyst libraries. *Nature* **1998**, *394*, 350.

(21) Guerrette, J. P.; Percival, S. J.; Zhang, B.: Fluorescence Coupling for Direct Imaging of Electrocatalytic Heterogeneity. *J Am Chem Soc* **2012**, *135*, 855-861.

(22) Leenheer, A. J.; Atwater, H. A.: Imaging Water-Splitting Electrocatalysts with pH-Sensing Confocal Fluorescence Microscopy. *Journal of The Electrochemical Society* **2012**, *159*, H752-H757.

(23) Weckhuysen, B. M.: Chemical Imaging of Spatial Heterogeneities in Catalytic Solids at Different Length and Time Scales. *Angewandte Chemie International Edition* **2009**, *48*, 4910-4943.

(24) Buurmans, I. L. C.; Weckhuysen, B. M.: Heterogeneities of individual catalyst particles in space and time as monitored by spectroscopy. *Nat Chem* **2012**, *4*, 873-886.

(25) Grunwaldt, J.-D.; Wagner, J. B.; Dunin-Borkowski, R. E.: Imaging Catalysts at Work: A Hierarchical Approach from the Macro- to the Meso- and Nano-scale. *ChemCatChem* **2013**, *5*, 62-80.

(26) Xu, W.; Kong, J. S.; Yeh, Y.-T. E.; Chen, P.: Single-molecule nanocatalysis reveals heterogeneous reaction pathways and catalytic dynamics. *Nat Mater* **2008**, *7*, 992-996.

(27) Meier, J.; Friedrich, K. A.; Stimming, U.: Novel method for the investigation of single nanoparticle reactivity. *Faraday Discussions* **2002**, *121*, 365-372.

(28) Tel-Vered, R.; Bard, A. J.: Generation and Detection of Single Metal Nanoparticles Using Scanning Electrochemical Microscopy Techniques†. *The Journal of Physical Chemistry B* **2006**, *110*, 25279-25287.

(29) Nakai, M.; Yamanoi, Y.; Nishimori, Y.; Yonezawa, T.; Nishihara, H.: Observation of Electrochemical Single-Electron-Transfer Events of Gold Nanoparticles in Aqueous Solution in the Presence of Both Ammonium and Sulfonate

Surface-Active Agents. *Angewandte Chemie International Edition* **2008**, *47*, 6699-6702.

(30) Sánchez-Sánchez, C. M.; Solla-Gullón, J.; Vidal-Iglesias, F. J.; Aldaz, A.; Montiel, V.; Herrero, E.: Imaging Structure Sensitive Catalysis on Different Shape-Controlled Platinum Nanoparticles. *J Am Chem Soc* **2010**, *132*, 5622-5624.

(31) Lai, S. C. S.; Dudin, P. V.; Macpherson, J. V.; Unwin, P. R.: Visualizing Zeptomole (Electro)Catalysis at Single Nanoparticles within an Ensemble. *J Am Chem Soc* **2011**, *133*, 10744-10747.

(32) Xiao, X.; Bard, A. J.: Observing Single Nanoparticle Collisions at an Ultramicroelectrode by Electrocatalytic Amplification. *J Am Chem Soc* **2007**, *129*, 9610-9612.

(33) Fan, F.-R. F.; Bard, A. J.: Observing Single Nanoparticle Collisions by Electrogenerated Chemiluminescence Amplification. *Nano Letters* **2008**, *8*, 1746-1749.

(34) Xiao, X.; Fan, F.-R. F.; Zhou, J.; Bard, A. J.: Current Transients in Single Nanoparticle Collision Events. *J Am Chem Soc* **2008**, *130*, 16669-16677.

(35) Xiao, X.; Pan, S.; Jang, J. S.; Fan, F.-R. F.; Bard, A. J.: Single Nanoparticle Electrocatalysis: Effect of Monolayers on Particle and Electrode on Electron Transfer. *The Journal of Physical Chemistry C* **2009**, *113*, 14978-14982.

(36) Kwon, S. J.; Fan, F.-R. F.; Bard, A. J.: Observing Iridium Oxide (IrO_x) Single Nanoparticle Collisions at Ultramicroelectrodes. *J Am Chem Soc* **2010**, *132*, 13165-13167.

(37) Chen, S.; Kucernak, A.: Electrocatalysis under Conditions of High Mass Transport: Investigation of Hydrogen Oxidation on Single Submicron Pt Particles

Supported on Carbon. *The Journal of Physical Chemistry B* **2004**, *108*, 13984-13994.

(38) Murray, R. W.: Nanoelectrochemistry: Metal Nanoparticles, Nanoelectrodes, and Nanopores. *Chem Rev* **2008**, *108*, 2688-2720.

(39) Krapf, D.; Wu, M.-Y.; Smeets, R. M. M.; Zandbergen, H. W.; Dekker, C.; Lemay, S. G.: Fabrication and Characterization of Nanopore-Based Electrodes with Radii down to 2 nm. *Nano Letters* **2005**, *6*, 105-109.

(40) Li, Y.; Cox, J. T.; Zhang, B.: Electrochemical Responses and Electrocatalysis at Single Au Nanoparticles. *J Am Chem Soc* **2010**, *132*, 3047-3054.

(41) Novo, C., Funston, Alison M., Mulvaney, Paul.: Direct Observation of Chemical Reactions on Single Gold Nanocrystals Using Surface Plasmon Spectroscopy. *Nature Nanotechnology* **2008**, *3*, 598-602.

(42) Novo, C.; Funston, A. M.; Gooding, A. K.; Mulvaney, P.: Electrochemical Charging of Single Gold Nanorods. *J Am Chem Soc* **2009**, *131*, 14664-14666.

(43) Cheng, J.; Liu, Y.; Cheng, X.; He, Y.; Yeung, E. S.: Real Time Observation of Chemical Reactions of Individual Metal Nanoparticles with High-Throughput Single Molecule Spectral Microscopy. *Analytical Chemistry* **2010**, *82*, 8744-8749.

(44) Tang, M. L.; Liu, N.; Dionne, J. A.; Alivisatos, A. P.: Observations of Shape-Dependent Hydrogen Uptake Trajectories from Single Nanocrystals. *J Am Chem Soc* **2011**, *133*, 13220-13223.

(45) Liu, N.; Tang, M. L.; Hentschel, M.; Giessen, H.; Alivisatos, A. P.: Nanoantenna-enhanced gas sensing in a single tailored nanofocus. *Nat Mater* **2011**, *10*, 631-636.

(46) Shan, X.; Diez-Perez, I.; Wang, L.; Wiktor, P.; Gu, Y.; Zhang, L.; Wang, W.; Lu, J.; Wang, S.; Gong, Q.; Li, J.; Tao, N.: Imaging the electrocatalytic activity of single

nanoparticles. *Nat Nano* **2012**, *7*, 668-672.

(47) De Cremer, G.; Sels, B. F.; De Vos, D. E.; Hofkens, J.; Roeffaers, M. B. J.: Fluorescence micro(spectro)scopy as a tool to study catalytic materials in action. *Chemical Society Reviews* **2010**, *39*, 4703-4717.

(48) Chen, P.; Zhou, X.; Shen, H.; Andoy, N. M.; Choudhary, E.; Han, K.-S.; Liu, G.; Meng, W.: Single-molecule fluorescence imaging of nanocatalytic processes. *Chemical Society Reviews* **2010**, *39*, 4560-4570.

(49) Tachikawa, T.; Majima, T.: Single-molecule, single-particle fluorescence imaging of TiO2-based photocatalytic reactions. *Chemical Society Reviews* **2010**, *39*, 4802-4819.

(50) Roeffaers, M. B. J.; Sels, B. F.; Uji-i, H.; De Schryver, F. C.; Jacobs, P. A.; De Vos, D. E.; Hofkens, J.: Spatially resolved observation of crystal-face-dependent catalysis by single turnover counting. *Nature* **2006**, *439*, 572-575.

(51) Naito, K.; Tachikawa, T.; Fujitsuka, M.; Majima, T.: Single-Molecule Observation of Photocatalytic Reaction in TiO_2 Nanotube: Importance of Molecular Transport through Porous Structures. *J Am Chem Soc* **2008**, *131*, 934-936.

(52) Yildiz, A.; Forkey, J. N.; McKinney, S. A.; Ha, T.; Goldman, Y. E.; Selvin, P. R.: Myosin V Walks Hand-Over-Hand: Single Fluorophore Imaging with 1.5-nm Localization. *Science* **2003**, *300*, 2061-2065.

(53) Thompson, R. E.; Larson, D. R.; Webb, W. W.: Precise Nanometer Localization Analysis for Individual Fluorescent Probes. *Biophysical Journal* **2002**, *82*, 2775-2783.

(54) Roeffaers, M. B. J.; Hofkens, J.; De Cremer, G.; De Schryver, F. C.; Jacobs, P. A.; De Vos, D. E.; Sels, B. F.: Fluorescence microscopy: Bridging the phase gap in catalysis. *Catalysis Today* **2007**, *126*, 44-53.

(55) Roeffaers, M. B. J.; De Cremer, G.; Uji-i, H.; Muls, B.; Sels, B. F.; Jacobs, P. A.; De Schryver, F. C.; De Vos, D. E.; Hofkens, J.: Single-molecule fluorescence spectroscopy in (bio)catalysis. *Proceedings of the National Academy of Sciences* **2007**, *104*, 12603-12609.

(56) Xu, W.; Shen, H.; Kim, Y. J.; Zhou, X.; Liu, G.; Park, J.; Chen, P.: Single-Molecule Electrocatalysis by Single-Walled Carbon Nanotubes. *Nano Letters* **2009**, *9*, 3968-3973.

(57) Roeffaers, M. B. J.; De Cremer, G.; Libeert, J.; Ameloot, R.; Dedecker, P.; Bons, A.-J.; Bückins, M.; Martens, J. A.; Sels, B. F.; De Vos, D. E.; Hofkens, J.: Super-Resolution Reactivity Mapping of Nanostructured Catalyst Particles. *Angewandte Chemie International Edition* **2009**, *48*, 9285-9289.

(58) Tachikawa, T.; Majima, T.: Single-Molecule Fluorescence Imaging of TiO_2 Photocatalytic Reactions. *Langmuir* **2009**, *25*, 7791-7802.

(59) De Cremer, G.; Bartholomeeusen, E.; Pescarmona, P. P.; Lin, K.; De Vos, D. E.; Hofkens, J.; Roeffaers, M. B. J.; Sels, B. F.: The influence of diffusion phenomena on catalysis: A study at the single particle level using fluorescence microscopy. *Catalysis Today* **2010**, *157*, 236-242.

(60) De Cremer, G.; Roeffaers, M. B. J.; Bartholomeeusen, E.; Lin, K.; Dedecker, P.; Pescarmona, P. P.; Jacobs, P. A.; De Vos, D. E.; Hofkens, J.; Sels, B. F.: High-Resolution Single-Turnover Mapping Reveals Intraparticle Diffusion Limitation in Ti-MCM-41-Catalyzed Epoxidation. *Angewandte Chemie International Edition* **2010**, *49*, 908-911.

(61) Tachikawa, T.; Yamashita, S.; Majima, T.: Evidence for Crystal-Face-Dependent TiO_2 Photocatalysis from Single-Molecule Imaging and Kinetic Analysis. *J Am Chem*

Soc **2011**, *133*, 7197-7204.

(62) Zhou, X.; Andoy, N. M.; Liu, G.; Choudhary, E.; Han, K.-S.; Shen, H.; Chen, P.: Quantitative super-resolution imaging uncovers reactivity patterns on single nanocatalysts. *Nat Nano* **2012**, *7*, 237-241.

(63) Tachikawa, T.; Yonezawa, T.; Majima, T.: Super-Resolution Mapping of Reactive Sites on Titania-Based Nanoparticles with Water-Soluble Fluorogenic Probes. *ACS Nano* **2012**, *7*, 263-275.

(64) Andoy, N. M.; Zhou, X.; Choudhary, E.; Shen, H.; Liu, G.; Chen, P.: Single-Molecule Catalysis Mapping Quantifies Site-Specific Activity and Uncovers Radial Activity Gradient on Single 2D Nanocrystals. *J Am Chem Soc* **2013**, *135*, 1845-1852.

(65) Herves, P.; Perez-Lorenzo, M.; Liz-Marzan, L. M.; Dzubiella, J.; Lu, Y.; Ballauff, M.: Catalysis by metallic nanoparticles in aqueous solution: model reactions. *Chemical Society Reviews* **2012**, *41*, 5577-5587.

(66) Li, Z. Y.; Young, N. P.; Di Vece, M.; Palomba, S.; Palmer, R. E.; Bleloch, A. L.; Curley, B. C.; Johnston, R. L.; Jiang, J.; Yuan, J.: Three-dimensional atomic-scale structure of size-selected gold nanoclusters. *Nature* **2008**, *451*, 46-48.

1.8 Supporting Information

1.8.1 Materials and General Methods

1.8.1.1 General Materials

All commercial materials were used as received unless specified otherwise. All experiments were done at room temperature under ambient conditions, unless specified otherwise. TEM (FEI Tecnai 12) and SEM (LEO 1550) were performed at the Cornell Center for Materials Research (CCMR) or the Cornell NanoScale Facility

(CNF). Image analyses were done using home-written MATLAB codes. The SEM images of larger areas, for example in Figure 2B in the main text, were taken piece wise in small areas. These smaller SEM images were then merged together using overlapping regions.

1.8.l.2 Catalyst Particles: Bare Pseudo-spherical Au Particles

The unconjugated (i.e., "bare") pseudo-spherical gold colloidal particles with diameters of 6.0 ± 1.7, 9.1 ± 1.5, 13.7 ± 2.4, 21.0 ± 4.0, 42.0 ± 8.1, 60.4 ± 8.4, 101.7 ± 13.4, 225.7 ± 35.3 nm were purchased from British Biocell International/Ted Pella and characterized by TEM. TEM images. Size distributions of these Au particles are shown in Figure 1.6, except for the 6.0 ± 1.7, 9.1 ± 1.5, 13.7 ± 2.4 nm ones, which were published previously in ref[1].

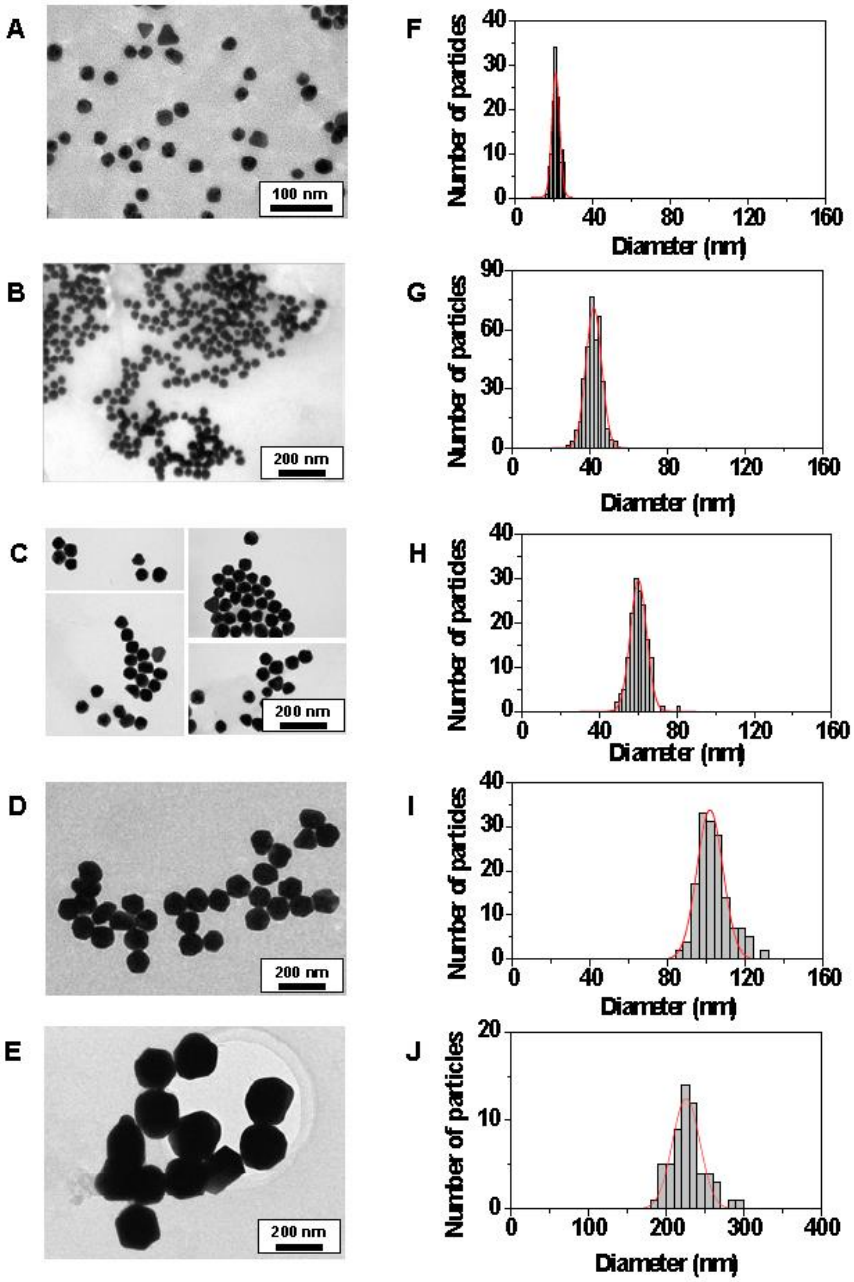

Figure 1.6 (A-E) TEM images of bare pseudo-spherical gold particles. (F-J) Corresponding diameter distributions from (A-E). The determined diameters are 21.0 ± 4.0 nm (from 145 particles), 42.0 ± 8.1 nm (from 362 particles), 60.4 ± 8.4 nm (from 156 particles), 101.7 ± 13.4 nm (from 150 particles), and 225.7 ± 35.3 nm (from 59 particles), respectively. The diameter is the center of the Gaussian fitting (red lines), and the error bar is the standard deviation.

1.8.1.3 Catalyst Particles: Mixture of Au@mSiO$_2$ Nanorods and Small Triangular, and Pseudo-spherical Particles

The mixture that contains gold nanorods, and triangular and pseudo-spherical particles were synthesized by three-step seeded growth protocol[2] and was described in detail in our previous publication[3]. Briefly, first, Au particle seeds were synthesized by reduction of $HAuCl_4$ (Aldrich) with $NaBH_4$. Then, the Au nanorods were grown stepwise from the Au seeds. The resulting sample was a mixture of particles: Au nanorods, triangular particles and pseudo-spherical particles (Figure 1.7A), which were collected from the bottom of the growth container, and dispersed in water for further use. The Au nanorods have ~100 nm to 700 nm lengths and 21.4 $\pm$ 3.2 nm diameters shown in Figure 1.7A, whose detailed size and shape analysis was reported in a previous study by us[3]. The sizes of triangular and pseudo-spherical particles are 113.5 $\pm$ 42.8 nm and 47.0 $\pm$ 15.4 nm shown in Figure 1.7B and C, respectively.

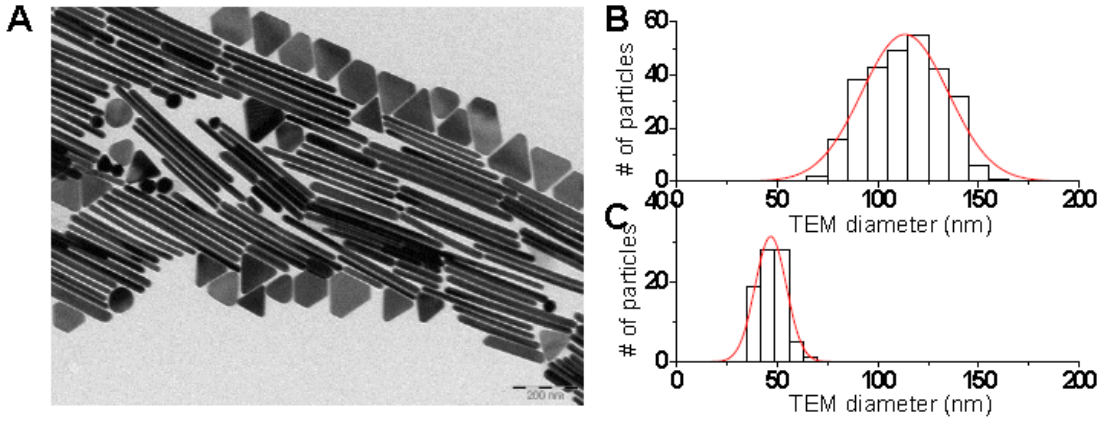

Figure 1.7 TEM characterization of the as-synthesized mixture of Au nanorods, and triangular and pseudo-spherical particles. (A) TEM image of the as-synthesized mixture. (B) Size distribution of triangular particles. The diameter of a particle was determined by boxing it in a rectangle in image analysis, and the average of the long and short edge lengths of the rectangular box was taken as approximation of its diameter. A Gaussian fit gives a diameter of 113.5 ± 42.8 nm. (C) Size distribution of pseudo-spherical Au nanoparticles. A Gaussian fit gives a diameter of 47.0 ± 15.4 nm.

The mesoporous silica coating was added onto the Au nanorods, triangular particles and pseudo-spherical particles (Au@mSiO_2) according to published procedures[4-6] and was described in detail in our previous publication3. Briefly, first, the as-synthesized Au particle mixtures were functionalized by 3-mercaptopropyltrimethoxysilane (MPTMS) (Aldrich) and sodium silicate solution. Second, a thick silica shell was grown by the hydrolysis of tetraethyl orthosilicate (TEOS) (Aldrich) in basic condition. Third, the silica shell was etched by NaOH with CTAB as a templating reagent to make mesoporous silica shell. The resulted mSiO_2 shell is ~80 nm thick (Figure 1.8)[3]. All mSiO_2-coated particles in this study were calcinated at 773 K for 1 hour, following literature procedures[6,7], before being used for catalysis. This calcination was to remove the organic surfactants and activate them for

catalysis, as we demonstrated previously[3]; and the morphology of the nanorods stay unchanged after calcination.

Due to the $mSiO_2$ coating, the small triangular particles are difficult to differentiate by shape from the pseudo-spherical particles using SEM, which only sees the outer structural contour, other than their differences in sizes. Therefore, when we used SEM to analyze the samples whose catalysis was imaged by single-molecule fluorescence microscopy, *we did not differentiate the triangular and pseudospherical ones and grouped them as "pseudo-spherical particles", apart from the nanorods*.

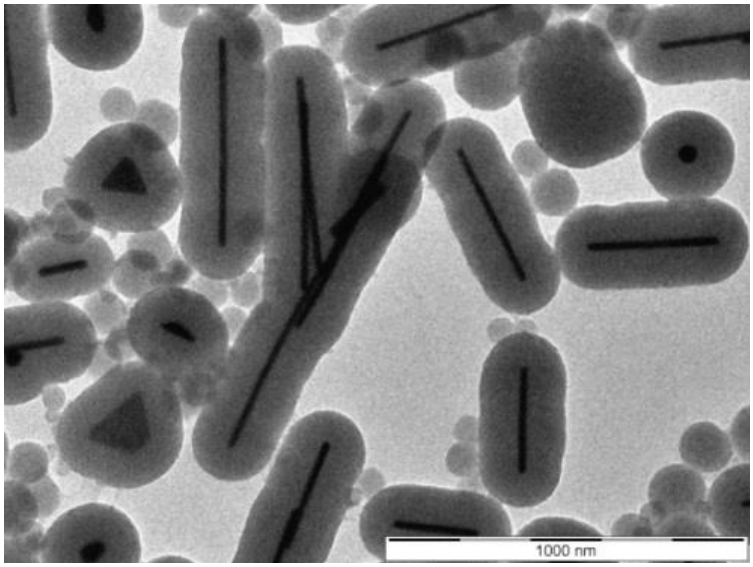

Figure 1.8 TEM of mesoporous-silica-coated Au nanorods, triangular and pseudo-spherical particles**.**

1.8.1.4 Catalyst Particles: Pseudo-spherical Au@$mSiO_2$ Particles of Different Core Diameters and $mSiO_2$ Shell Thicknesses.

Starting from the unconjugated pseudo-spherical Au colloidal particles described in Section 1.8.1.2, we also coated them with the $mSiO_2$ shell to make the pseudo-spherical Au@$mSiO_2$ particles of variable core diameters and shell thicknesses using the same protocol as in Section 1.8.1.3. Figure 1.9 shows the TEM images of

the pseudo-spherical Au@mSiO_2 particles that were used to demonstrate the sub-diffraction resolution of our single-molecule catalysis imaging approach, as presented in Figure 1.2E in the main text. Their corresponding core diameters and outer diameters are presented in Figure 1.6 and Figure 1.10, respectively.

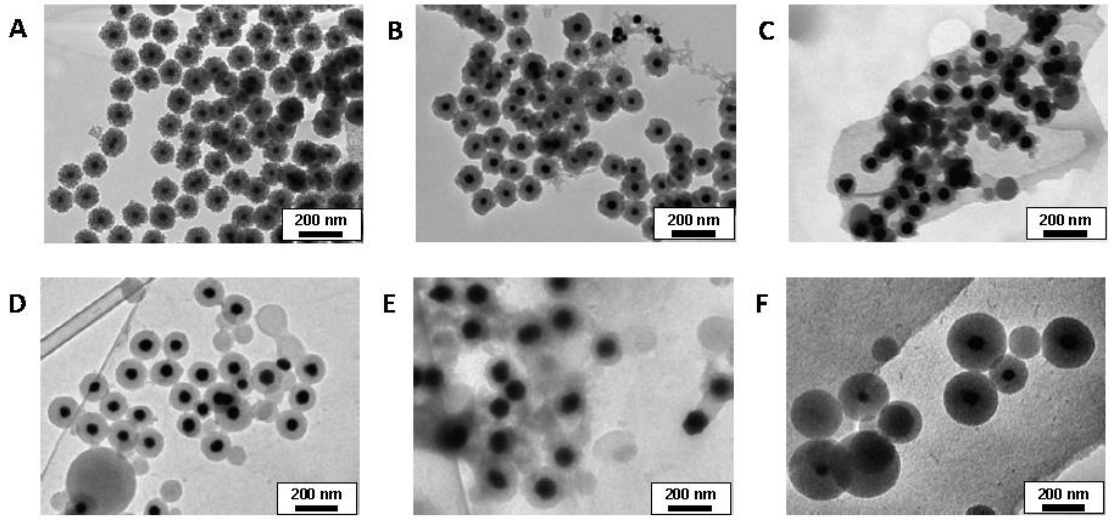

Figure 1.9 TEM images of pseudo-spherical Au@mSiO_2 particles that were used for acquiring the results presented in Figure 1.2E in the main text. Their measured size distributions are presented in Figure 1.10 below.
(A) 42.0@28.4 nm (core-diameter@shell-thickness) particles, with inner diameter of 42.0 ± 4.1 nm and outer diameter (OD) of 98.8 ± 7.3 nm.
(B) 42.0@38.6 nm particles, with inner diameter of 42.0 ± 4.1 nm and OD of 119.2 ± 8.5 nm.
(C) 60.4@24.5 nm particles, with inner diameter of 60.4 ± 4.2 nm and OD of 109.4 ± 7.0 nm.
(D) 60.4@42.8 nm particles, with inner diameter of 60.4 ± 4.2 nm and OD of 146.0 ± 12.7 nm.
(E) 101.7@33.4 nm particles, with inner diameter of 101.7 ± 6.7 nm and OD of 168.4± 12.5 nm.
(F) 60.4@96.8 nm particles, with inner diameter of 60.4 ± 4.2 nm and OD of 254.0± 21.9 nm.

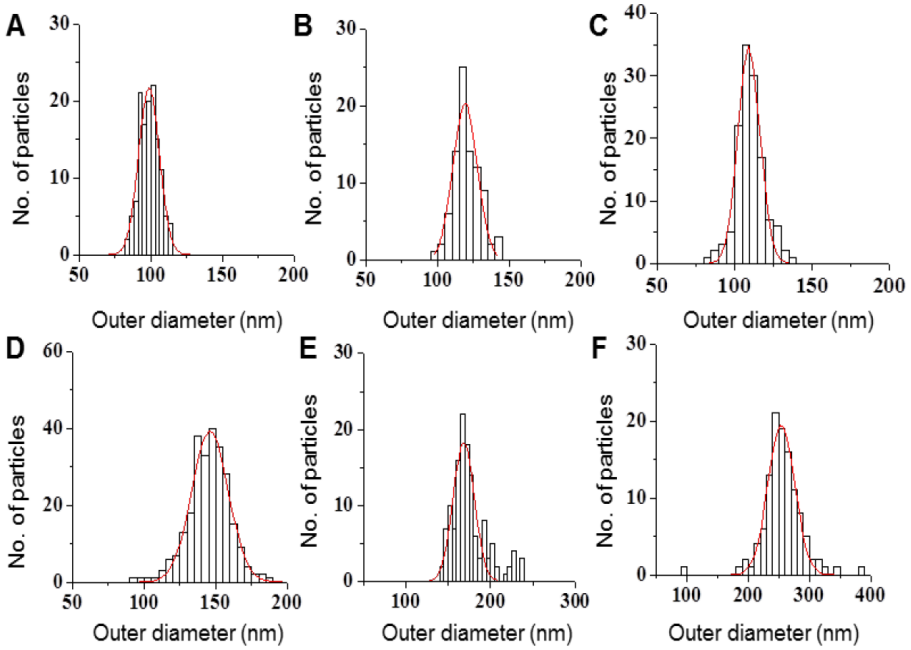

Figure 1.10 The outer diameter distributions of the pseudo-spherical Au@mSiO$_2$ particles from Figure 1.9A-F, respectively. The average outer diameters are (A) 98.7 ± 7.3 nm; (B) 119.2 ± 8.5 nm; (C) 109.4 ± 7.0 nm; (D) 146.0 ± 12.7 nm; (E) 168.4± 12.5 nm; and (F) 254.0± 21.9 nm.

1.8.1.5 Table 1.1. List of Catalyst Particle Sizes and Their Abbreviated Names

The following table lists the sizes of the catalyst particles for which we used abbreviated names for referring to them in the main text.

Catalyst particles (diameter or core-diameter@shell-thickness)	**Abbreviated denotations**	**references**
Bare pseudo-spherical Au particles used for Figure 1.2 in the main text as well as for making Au@mSiO$_2$ particles		
6.0 ± 1.7 nm	6 nm	reference[1]
9.1 ± 1.5 nm	9 nm	
13.7 ± 2.4 nm	14 nm	
Bare pseudo-spherical Au particles used for making Au@mSiO$_2$ particles		
21.0 ± 4.0 nm	21 nm	Figure 1.6
42.0 ± 8.1 nm	42 nm	
60.4 ± 8.4 nm	60 nm	
101.7 ± 13.4 nm	102 nm	
Pseudo-spherical Au@mSiO$_2$ particles used for Figure 1.2 in the main text		
42.0@28.4 nm	42@28 nm	Figure 1.9
42.0@38.6 nm	42@39 nm	
60.4@24.5 nm	60@25 nm	
60.4@42.8 nm	60@43 nm	
101.7@33.4 nm	102@33 nm	
60.4@96.8 nm	60@97 nm	
Pseudo-spherical Au@mSiO$_2$ particles used for Figure 1.3 in the main text		
21.0@41.5 nm	21@42 nm	Figure 1.22
101.7@32.4 nm	102@32 nm	
Pseudo-spherical bare Au and Au@mSiO$_2$ particles used for Figure 1.5 in the main text		
6.0 ± 1.7 nm	6 nm	reference[1]
9.1 ± 1.5 nm	9 nm	
21.0 ± 4.0 nm	21 nm	Figure 1.6
101.7 ± 13.4 nm	102 nm	
225.7 ± 35.3 nm	226 nm	
6.0@37.5 nm	6@38 nm	Figure 1.35
21.0@80.6 nm	21@81 nm	
42.0@65.4 nm	42@65 nm	
42.0@70.3 nm	42@70 nm	
60.4@82.8 nm	60@83 nm	
101.7@58.6 nm	102@59 nm	

1.8.1.6 Ensemble Catalytic Activity Measurements

All ensemble catalytic activity measurements were done at room temperature in 3.4 mM pH 7.3 phosphate buffer solution. The reactants were premixed before injecting an aliquot of 5 to 100 μL solution of catalyst particles to initiate the reactions. The catalysts include bare Au particles of 6, 9, 21, 102, and 226 nm in diameter (Table 1.1), and the other pseudo-spherical Au@mSiO_2 particles of 6@38, 21@81, 42@65, 42@70, 60@83, 102@59 nm in size (Table 1.1). The concentrations of core-shell Au particles were calibrated by their UV-Vis extinction band from their surface plasmon resonance.

The oxidative N-deacetylation reaction of amplex red (Invitrogen) to resorufin by H2O2 was monitored using the fluorescence signal of the product resorufin at 586 nm excited at 532 nm. Amplex red was at 0.69 μM and H_2O_2 was at 60 mM. The reductive N-deoxygenation reaction of resazurin (Invitrogen) by NH_2OH was monitored using the absorption of the reactant resazurin at 604 nm for bare Au particle catalyzed reactions or the fluorescence signal of the product resorufin at 586 nm excited at 532 nm for Au@mSiO_2 catalyzed reactions. Resazurin was at 2.2 μM and NH_2OH was at 1.0 mM. The hydroquinone (Allied Chemical) oxidation by H_2O_2 was monitored using the absorption of hydroquinone at 280 nm for bare Au particles catalyzed reactions or the fluorescence signal of hydroquinone at 330 nm excited at 250 nm for Au@mSiO_2 particles catalyzed reactions. Hydroquinone was at 69 μM and H_2O_2 was at 0.6 mM. The 4-nitrophenol (Sigma-Aldrich) reduction by $NaBH_4$ was monitored using the absorption of 4-nitrophenol at 400 nm. 4-nitrophenol and $NaBH_4$ were at 51.7 μM and 1.0 mM, respectively, for bare Au particle catalyzed reactions, or at 34.5 μM and 3.4 mM, respectively, for Au@mSiO_2 particles catalyzed reactions.

1.8.2 Single-molecule Fluorescence Microscopy of Catalysis

The single-molecule fluorescence experiments were done on a home-made prism-type total internal reflection fluorescence (TIRF) microscopy based on an Olympus IX71 microscope[1,8]. A continuous circularly-polarized 532 nm laser beam (CrystaLaser) of 2-20 mW was directed onto the sample to directly excite the fluorescence of the catalytic product resorufin via a TIRF geometry. The fluorescence was collected by a 60× NA1.2 water-immersion objective (UPLSAPO60XW, Olympus), filtered (HQ580m60, Chroma), and detected by a back-illuminated ANDOR iXon EMCCD camera (DU897D-CS0-#BV) operated at 25 ms frame rate. The reactants were continuously fed into a flow cell (about 100 μm (height) × 5 cm (length) × 5 mm (width)) shown in Figure 1.11A with a syringe pump at 10 μL/min, and were catalytically converted to fluorescent products, which were detected by the EMCCD camera.

We used two fluorogenic probe reactions to test the catalyst activities using our fluorescence microscopy approach. One was the oxidative N-deacetylation reaction of amplex red to resorufin by H_2O_2, and the other was the reductive N-deoxygenation of resazurin to resorufin by NH_2OH, both in aqueous solutions (Figure 1.11B).

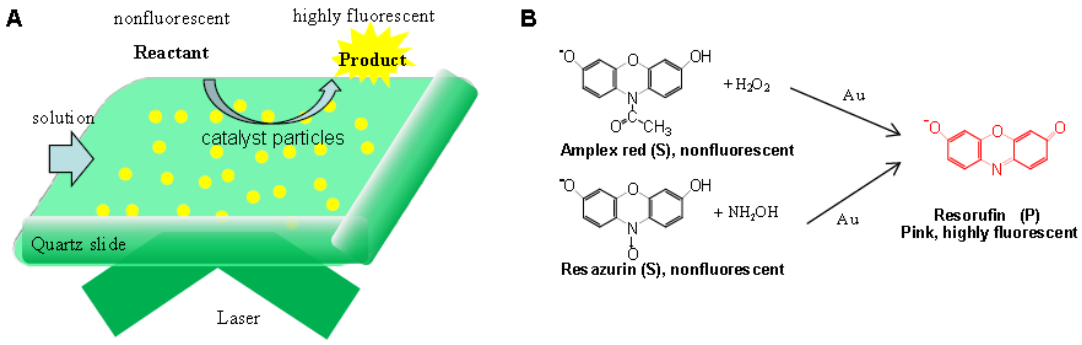

Figure 1.11 Wide-field, single-molecule fluorescence imaging of catalysis on a large number of catalyst particles. (A) Schematic of the flow cell showing many catalyst particles immobilized on the quartz slide, the fluorogenic catalytic reaction, the continuous flow supplying the reactant solution, and the total internal reflection laser excitation that illuminates an area of ≥100 × 50 μm^2. (B) Reaction schemes: the fluorogenic oxidative N-deacetylation of the nonfluorescent amplex red molecule (denoted as S) to the fluorescent resorufin (denoted as P) by H_2O_2, catalyzed by Au particles; and the fluorogenic reductive N-deoxygenation of the nonfluorescent resazurin molecule (denoted as S) to the fluorescent resorufin (denoted as P) by NH_2OH, catalyzed by Au particles.

1.8.3 Nanometer Localization of Individual Catalytic Products in Fluorescence Images

The images in the movies recorded from the single-molecule fluorescence microscopy experiments were usually 400 × 200 pixels, covering about 100 × 50 μm^2 area on the quartz slide where a large number of catalyst particles were immobilized.

To decrease the computational demand, we first separated the entire image into grids of 7 × 7 pixels except for the 3-pixel wide area along the four edges of the image (Figure 1.12A). Excluding this 3 pixel-width around the edge was to avoid analyzing fractions of fluorescence signals of single catalytic product molecules that reside in this area - the fluorescence signal of a single molecule in the image appears as a point spread function (PSF), whose FWHM is about ~470 nm (i.e., ~2 pixels) for our microscope.

For each 7 × 7 pixel area, the EMCCD counts were integrated to get the fluorescence intensity and extracted versus time (i.e., frame index) from the entire movie (Figure 1.12B). If a catalytic product molecule was detected within the 7 × 7 pixel at any time, a fluorescence intensity burst would be observed in the extracted fluorescence intensity trajectory and would be selected by an automated intensity thresholding algorithm (Figure 1.12B), which was detailed in our previous publication[3]. For each detected catalytic product, a 13 × 13 pixel (~3.5 × 3.5 μm^2) area around it was redefined (Figure1.12A) and the frames during which the product stayed visible were added together to get a combined 13 × 13 pixel small image, from which the intrinsic emission signal of the catalyst particle, if present, was subtracted out (Figure 1.12C), as we detailed previously[3]. Then the combined frame was fitted by a modified two-dimensional Gaussian function that contained a sloping plane to account for the background (Figure 1.12D)[3]:

$$I(x, y) = A + Bx + Cy + \int_{x-\delta}^{x-\delta} \mathrm{d}X \int_{y-\delta}^{y-\delta} \mathrm{d}Y I_0 \exp\left[-\frac{1}{2}\left(\frac{X - x_0}{\sigma_x} \right)^2 - \frac{1}{2}\left(\frac{Y - y_0}{\sigma_y} \right)^2 \right]$$

The center (x_0, y_0) of the fitted Gaussian function was the location of the product molecule. And $A + Bx + Cy$ was a sloping plane for accounting for the background in the image. The position error E_i from the fitting was calculated according to Thompson et al[9]:

$$Er_i = \sqrt{\frac{\sigma_i^2}{N} + \frac{a^2}{12N} + \frac{8\pi\sigma_i^4 b^2}{a^2 N^2}}$$

where $i = x$ or y, σ_i is the standard deviation from the fitted Gaussian function above, a is the pixel size (266.67 nm) in the fluorescence image, and b is the standard deviation

of the background. *N* is the total number of detected photons that could be determined from the EMCCD counts[3]. All determined positions were further corrected for sample drifting using position marks (Au particles themselves) on the sample, as we detailed previously, to generate the final positions of all detected product molecules (Figure 1.12E)[3]. If the fitted locations fell outside of the center 7 × 7 pixel area of the 13 × 13 pixel area; they were discarded because they would be more reliably obtained in analyzing the neighboring 7 × 7 pixels.

The entire grids of 7 × 7 pixel areas were analyzed one at a time and the results from them eventually patched together (Figure 1.12F), from which a 2-D histogram could be taken to generate the sub-diffraction catalysis image (Figure 1.12G). From the large, sub-diffraction-resolution catalysis image, we could identify every catalytically active particle in correlation with the corresponding SEM image of the same sample area (Figure 1.12H). Because the analysis of the entire image was done piece-wise and involves the final merging, the particles that happened to reside at the edges of the 7 × 7 pixel areas were problematic. In order to solve this problem, the isolated particles were selected again individually based on the SEM image, and their catalytic events were re-analyzed in the corresponding locations in the fluorescence image.

Our current home-made software in automating the above analysis of the fluorescence movies is not ideal; it underestimates events at the 7 × 7 grid dividing lines. But this does not change our results in histogramming the well-isolated particles, which were re-analyzed selectively as described above. We are working on a new computer code to analyze the large fluorescence image in parallel without dissecting it into small grids.

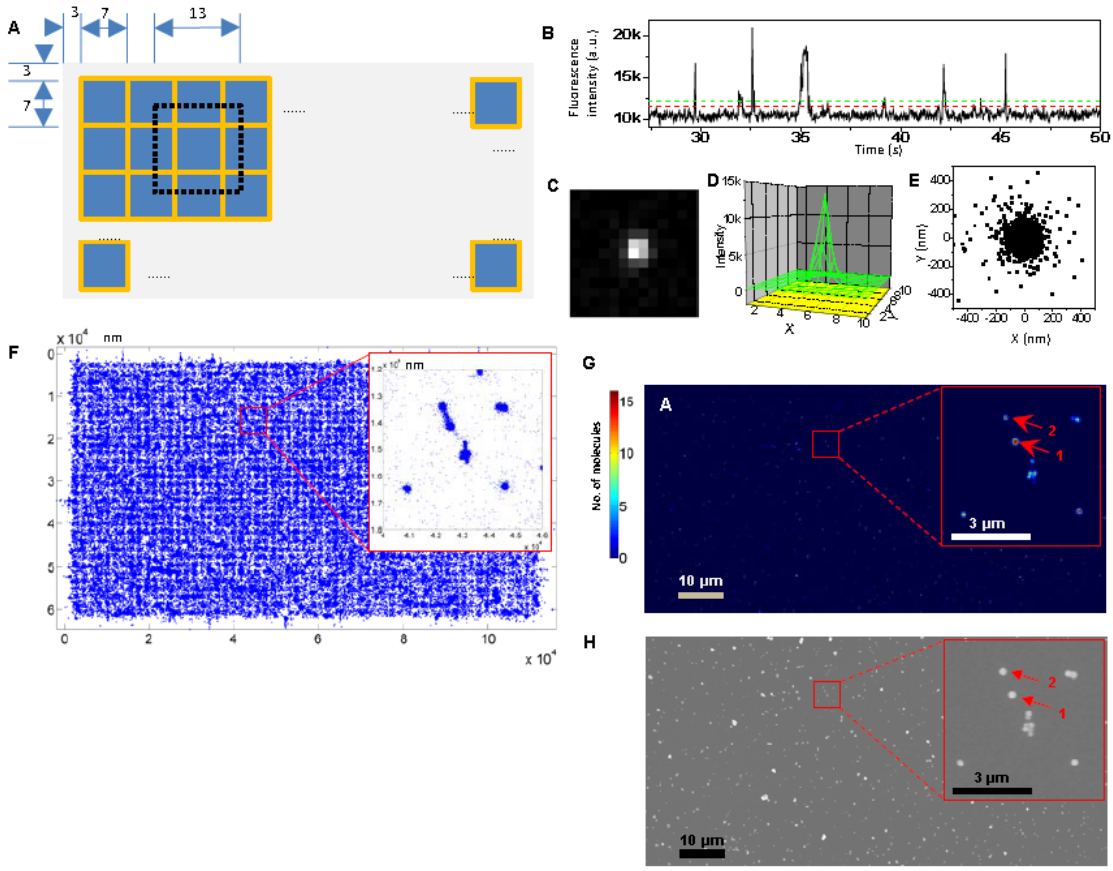

Figure 1.12 (A) Image dissection scheme for analyzing the single-molecule fluorescence images for sub-diffraction resolution imaging analysis of the catalytic reactions of many catalyst particles. (B) An exemplary fluorescence intensity trajectory here, showing the fluorescence intensity bursts due to catalytic product formation and thresholding to select the bursts. (C) An exemplary 13 × 13 pixel image of a reaction product. (D) The fitted PSF of a single catalytic product molecule plotted in 3-D. (E) An exemplary scatter plot of all product positions from a catalyst particle. (F) A global scatter plot of all product molecule positions with a zoom in. The crowded looking is due more to visual effects of plotting too many dots on the figure; the zoom in is a better representation. (G) Sub-diffraction catalysis image, which is a 2-D histogram of the product positions in F. The figure is the same as Figure 1.3A in the main text. (H) SEM image corresponding to the same area in F. This figure is the same as Figure 1.3B in the main text.

1.8.4 Extracting the Size Information from the Locations of Individual Catalytic Product Molecules on Single Catalyst Particles

The single-molecule imaging and nanometer localization of individual catalytic products produces a large number of locations from many catalyst particles, with these product locations clustered around individual particles (e.g., Figure 1.2A and 1.2C in the main text and Figure 1.12E and F). To extract the size information about a catalyst particle from its product locations, we used three different analysis methods for both the bare and the $mSiO_2$ coated catalyst particles: the model-fitting method for both types of the catalyst particles is most reliable in extracting the size information, but also computationally most costly; the other two methods, which are empirical in nature, are less reliable but fast computationally. The results from all three analysis methods are included in Figure 1.2E in the main text across a series of bare Au and Au@$mSiO_2$ catalyst particles.

1.8.4.1 For Bare Pseudo-spherical Catalyst Particles

(1) One-dimensional (1-D) model fitting. The catalyst particles are 3-D objects, but our imaging is in 2-D, onto which the locations of the fluorescent catalytic reaction product resorufin are projected. To extract the size information about the catalyst particle, here we use a model to fit the distributions of the product locations that are further projected onto 1-D (i.e., along *x* or *y* direction; e.g., Figure 1.13C-E). This model assumes that the pseudo-spherical catalyst particles are perfect spheres and the catalytic reactions occur evenly on the surface so that over a period of time, the detected product molecules sample all surface sites on the sphere evenly. Then the distribution of the product locations follow the spherical surface, which are projected

onto 2-D and further to 1-D (Figure 1.13A). The projected 1-D distribution of a sphere is a constant value within the dimension of the sphere:

$$N(x) = \begin{cases} \rho \dfrac{(2\pi R(h+\mathrm{d}x) - 2\pi Rh)}{\mathrm{d}x} = 2\pi\rho R; & \textbf{when } -R \le x \le R \\ 0; & \textbf{when } x < -R \textbf{ or } x > R \end{cases}$$

where R is the radius of the sphere, h is the height of a spherical cap, and ρ is the density of catalytic events on the spherical surface.

Because our nanometer localization of molecular positions has a finite spatial resolution, $N(x)$ needs to be convoluted with a broadening function, $g(x')$, which we approximate as a Gaussian function with a FWHM = 2.355σ, where σ is the standard deviation of the Gaussian function:

$$N'(x) = \int_{-\infty}^{+\infty} N(x - x')g(x')\mathrm{d}x'$$

$N'(x)$ is plotted in Figure 1.13B and was used to fit the 1-D histogram of product molecule locations of bare Au NPs of 6, 9, and 14 nm in diameter in both x and y directions shown in Figure 1.13C-E. In these fittings, the radius R was fixed to the values determined from TEM (i.e., half of the diameter of 6.0, 9.1, and 13.7 nm, respectively) and the FWHM (and thus σ) of the Gaussian convolution function $g(x')$ was floated. The resulting FWHMs of the fitted $N'(x)$ were 15.3 ± 0.6, 24.5 ± 0.9 and 15.5 ± 1.1 nm, respectively, for the 6, 9, 14 nm Au particles. These FWHMs are all larger than the actual size of the respective catalyst particles; therefore, the size of any catalyst particles that are smaller than these FWHMs cannot be measured reliably using the single-molecule catalysis imaging approach, and these values represent the *effective spatial resolution of our approach*. We have used these three values as the

"apparent size" for the 6, 9, 14 nm particles, and plotted them in Figure 1.2E in the main text.

Using this model, we also simulated $N'(x)$ as a function of R, using σ = 10, 15, 20, or 25 nm for the Gaussian broadening function $g(x')$. We then determined the FWHMs of the simulated $N'(x)$ and plotted against $2R$ (i.e., the diameter of the particle) in Figure 1.2E (the four dashed lines).

Figure 1.14 shows the measurement of a single 6 nm particle using this 1-D model fitting method and the other two analyses methods; the latter two are described below.

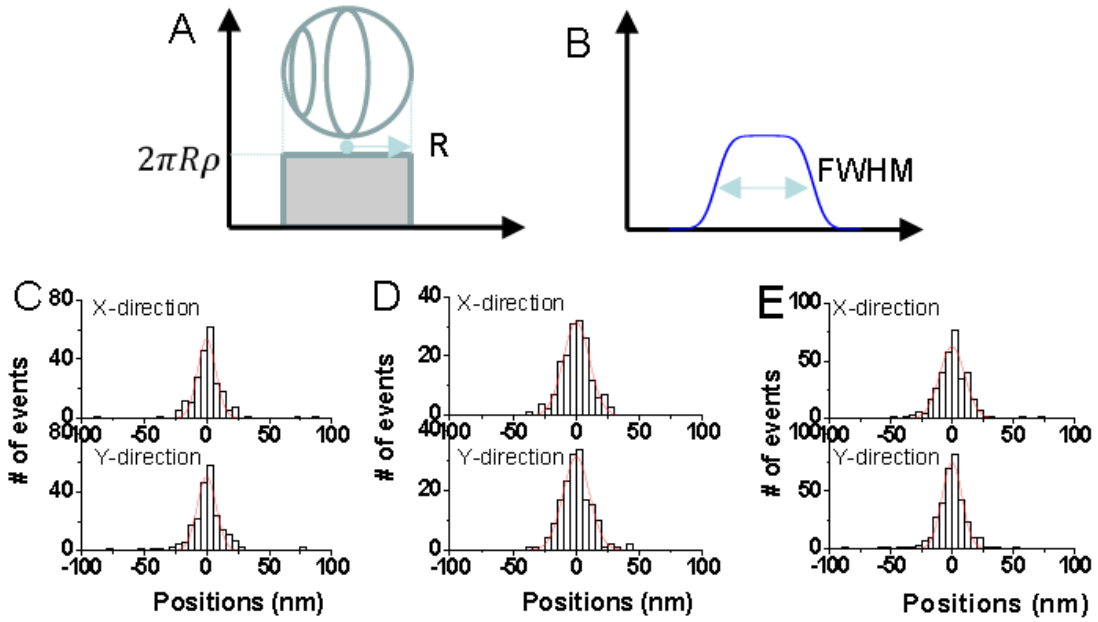

Figure 1.13 1-D model fitting of the product location histograms from bare pseudo-spherical Au particles. (A) Schematic of projecting the spherical surface of radius R onto one dimension and the resulted distribution function $N(x)$. (B) Schematic of the 1-D distribution function $N'(x)$ after convolution with a Gaussian broadening function. (C, D, E) Fitting of the 1-D histograms in x and y directions of the product locations by $N'(x)$ for 6, 9, and 14 nm bare Au particles. The fitted $N'(x)$'s have FWHMs of (C) in x, 14.9 ± 0.9 nm; in y, 15.7 ± 0.2 nm; average is 15.3 ± 0.6 nm; (D) in x, 24.4 ± 0.8 nm; in y, 24.6 ± 1.0 nm; average is 24.5 ± 0.9 nm; (E) in x, 17.8 ± 1.4 nm; in y, 13.2 ± 0.7 nm; average is 15.5 ± 1.1 nm.

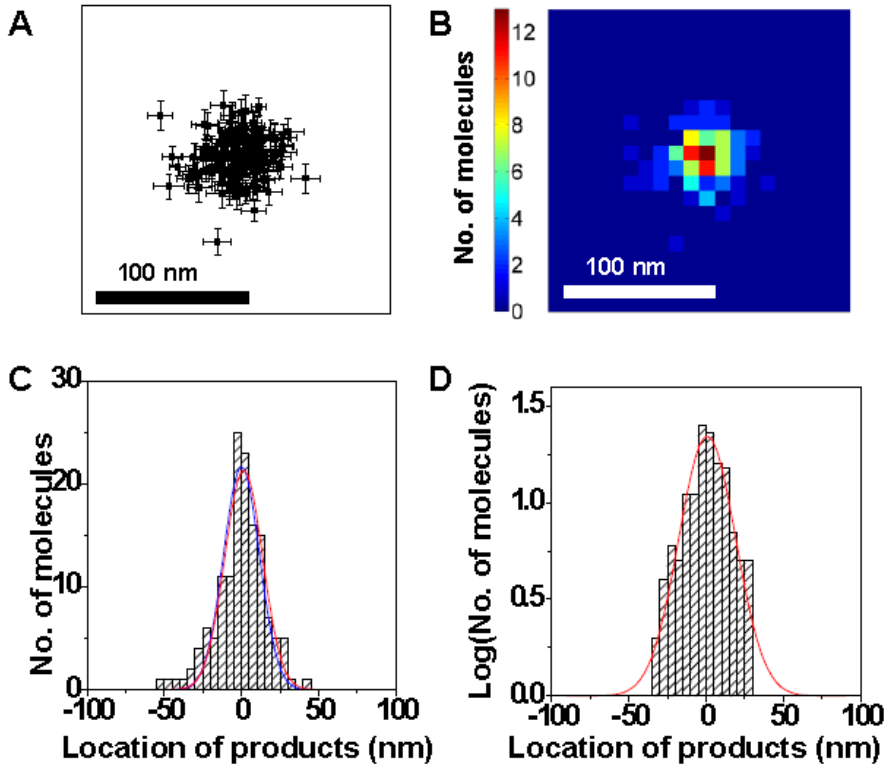

Figure 1.14 (A) Scatter plot of the catalytic product locations from a single 6 nm bare Au nanoparticle in catalyzing the reductive N-deoxygenation reaction of resazurin. (B) 2-D histogram of A with 10 × 10 nm^2 bins. A and B are the same as Figure 1.2A and B in the main text. (C) 1-D histogram of A along *x* direction. The red line is 1-D model fitting with the fitted FWHM of 27.4 ± 2.3 nm; the blue line is Gaussian fitting with the fitted FWHM of 28.7 ± 1.7 nm. (D) 1-D histogram of A along *x* direction; the y-axis is converted to log scale. The red line is Gaussian fitting with FWHM = 43.4 ± 2.7 nm.

(2) Empirical 1-D Gaussian fitting of the location histograms. This is a simple empirical method. First, the 1-D histograms of product molecule locations in *x* and *y* directions were obtained. Second, the histograms were fitted with a 1-D Gaussian function (Figure 1.14C). The average FWHM of the two fitted 1-D Gaussian functions were used as a measure of the apparent size of the particle. Figure 1.15 shows the histograms and corresponding fitting curves of 6, 9, and 14 nm bare Au particles, whose average FWHM of *x* and *y* directions are 17.1 ± 1.0, 24.4 ± 0.9 and

21.4 ± 1.2 nm, respectively, which are plotted in Figure 1.2E in the main text.

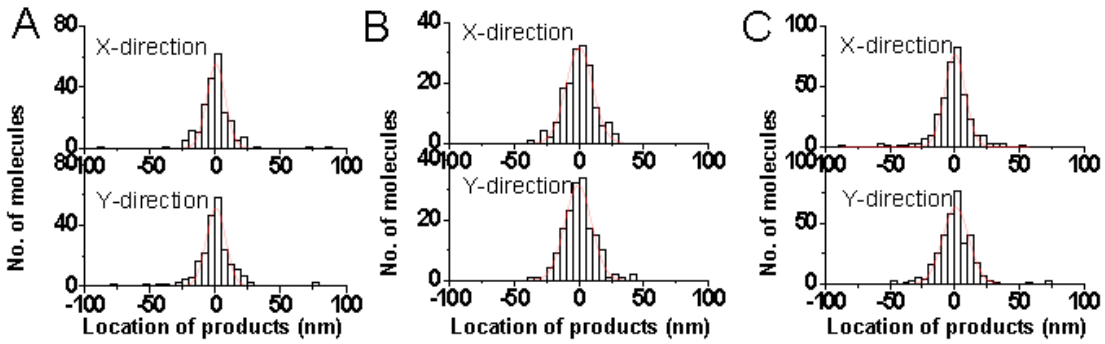

Figure 1.15 Empirical 1-D Gaussian fitting to determine the apparent size of the catalyst particle from its histograms of product locations. (A) 1-D histograms of product locations in x and y direction for 6 nm bare Au catalyst particles and the corresponding Gaussian fits (red lines). Data from 5 particles are overlaid using the mass center of locations to increase statistics. The fitted Gaussian FWHM in x is 16.7 ± 0.9 nm, in y is 17.5 ± 1.1 nm, and the average FWHM is 17.1 ± 1.0 nm. (B) Same as A, but for 9 nm bare Au particles. Data from 7 particles are overlaid. FWHM in x is 24.3 ± 0.8 nm, in y is 24.4 ± 0.9 nm, and the average is 24.4 ± 0.9 nm. (C) Same as A, but for 14 nm Au particles. Data from 32 particles are overlaid. FWHM in x is 18.8 ± 0.8 nm, in y is 23.9 ± 1.5 nm, and the average is 21.4 ± 1.2 nm.

(3) Empirical 1-D Gaussian fitting of the location histograms in log-scale.

This method is similar to (2) above. The difference is that the 1-D histograms of the product locations were first converted to log scale in the y-axis before the Gaussian fitting (Figure 1.14D). We decided to use this empirical fitting as well, because we noticed that the linear 1-D histograms often have long tails on both sides that could not be fitted well by Gaussian functions. These side tails become less problematic in the log-scale. Figure 1.16 shows the log-scale histograms and corresponding fitting curves of 6, 9, 14 nm bare Au particles, whose average FWHM of *x* and *y* directions are 37.6 ± 2.2, 40.1 ± 1.7 and 44.9 ± 2.4 nm, respectively. These average FWHMs are used as a measure of apparent sizes of the catalyst particles from the catalysis imaging and plotted in Figure 1.2E in the main text.

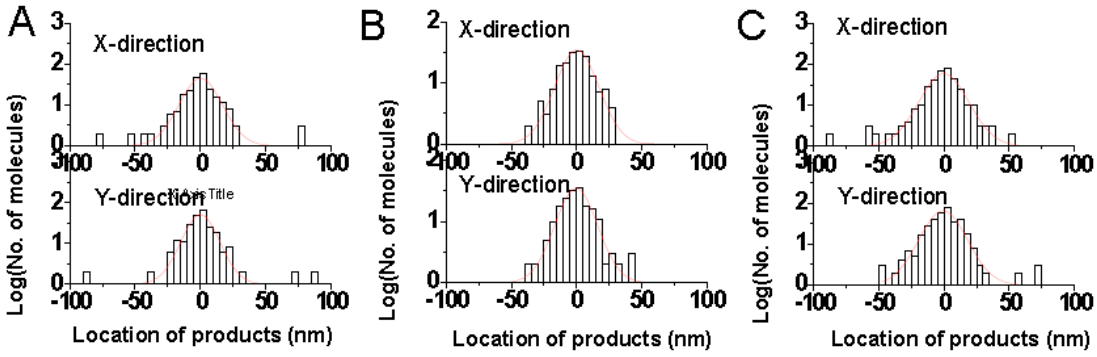

Figure 1.16 Empirical 1-D Gaussian fitting to determine the apparent size of the catalyst particle from its *log-scale* histograms of product locations. (A) 1-D histogram in log scale of the product locations in x and y directions for 6 nm bare Au particles and the corresponding Gaussian fits (red lines). The fitted Gaussian FWHM in x is 39.6 ± 2.3 nm, in y is 35.6 ± 2.1 nm, and the average FWHM is 37.6 ± 2.2 nm. (B) Same as A, but for 9 nm bare Au particles. FWHM in *x* is 40.2 ± 1.6 nm, in *y* is 39.0 ± 1.8 nm, and the average is 40.1 ± 1.7 nm. (C) Same as A, but for 14 nm Au particles. FWHM in x is 45.5 ± 2.2 nm, in y is 44.3 ± 2.5 nm, and the average is 44.9 ± 2.4 nm.

1.8.4.2 For Pseudo-spherical Au@mSiO_2 Catalyst Particles

(1) Two-dimensional (2-D) core-shell model fitting. For the pseudo-spherical Au@mSiO_2 particles, the catalytic product molecules are generated on the Au particle surface and detected while they are temporarily trapped in the mSiO_2 shell. Assuming that the product molecules will sample the entire mSiO_2 shell evenly over a large number of catalytic reactions on the same particle, the distribution of the product locations will follow the distribution of the shell volume. Mathematically, the volume of this shell (N) is equivalent to the difference between the spherical volume ($N1$) of the outer shell (radius, R) and the spherical volume ($N2$) of the core (radius r). Using this model, we project the distribution of this shell volume into 2-D ($N(x,y)$), in which our imaging was done (Figure 1.17A). This 2-D projection of shell volume $N(x,y)$ is (Figure 1.17B):

$$N(x,y) = N_1(x,y) - N_2(x,y)$$

Where

$$N_1(x,y) = 2\rho\sqrt{R^2 - x^2 - y^2};\ x,y \in [-R, R] \text{ and } x^2 + y^2 \le R^2$$
$$N_2(x,y) = 2\rho\sqrt{r^2 - x^2 - y^2};\ x,y \in [-r, r] \text{ and } x^2 + y^2 \le r^2$$

And ρ is the density of product molecules in the shell.

Again, because our nanometer localization of product positions has a finite spatial resolution, $N(x,y)$ needs to be convoluted with a broadening function, $g(x',y')$, which we approximate as a Gaussian function with a FWHM = 38.2 nm (i.e., its standard deviation being 16.2 nm) to give $N'(x,y)$ (Figure 1.17C):

$$N'(x,y) = \int_{-\infty}^{+\infty}\int_{-\infty}^{+\infty} N(x-x', y-y')g(x',y')dx'dy'$$

Note this FWHM value of 38.2 nm for $g(x',y')$ is larger than the FWHMs (~15 nm) of $g(x')$ determined from analyzing the 6, 9, 13 nm bare particles above; this is because the FWHM of the convolution function depends on the localization errors of the individual molecules and it broadens when the average location error is larger (i.e., less accurate) as we showed previously[3]. For these Au@mSiO$_2$ particles, their catalytic product molecules desorb faster than those 6, 9, 14 nm bare particles, leading to their less fluorescence photon counts overall and thus less localization accuracy. We found that with including more and more localizations of less accuracy, this FWHM, thus the *effective spatial resolution*, broadens but eventually saturates to ~38.2 nm,[3] which is used here.

$N'(x,y)$ was used to fit the 2-D histogram of the catalytic product positions (Figure 1.18B), where we fixed r, the core radius, to the value from TEM, and the

FWHM of the convolution function g(x',y'), and floated R, the outer radius of the shell (Figure 1.18C). Using this 2-D model fitting method, we analyzed individual particles of different sets of Au@mSiO$_2$ particles, and obtained their apparent size distribution (Figure 1.19). We then obtained the average apparent size for each set of particles and plotted the average values in Figure 1.2E in the main text.

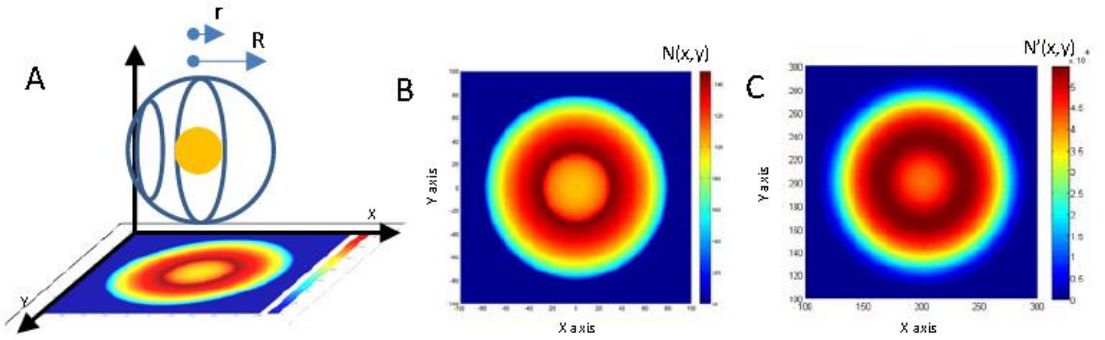

Figure 1.17 2-D model of the product location histograms from pseudo-spherical Au@mSiO$_2$ particles. (A) Schematic of projecting the spherical shell volume with outer radius R and inner radius r onto a 2-D plane and the resulted distribution function $N(x,y)$. (B) Replot of $N(x,y)$ from A; here r = 30 nm and R = 80 nm in the simulation. (C) Schematic of the 2-D distribution function $N'(x,y)$ after convolution with a Gaussian broadening function.

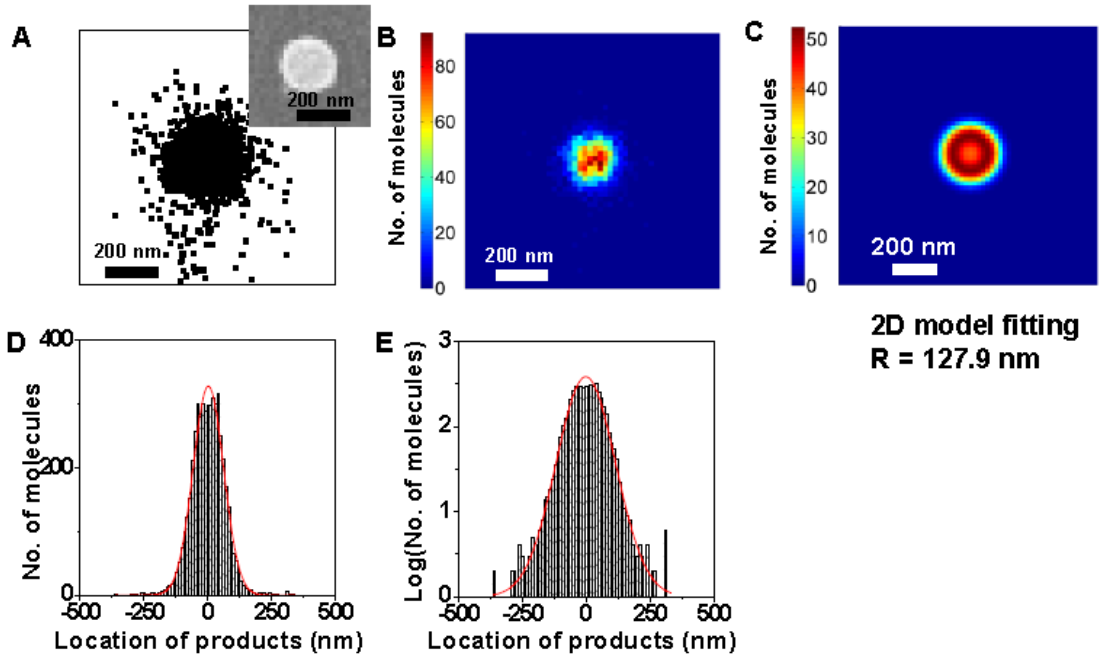

Figure 1.18 (A) Scatter plot of catalytic product positions from a single pseudo-spherical 101.7@33.4 nm Au@mSiO_2 particle (outer diameter = 168.5 nm; this value is the average of many particles of this batch of 101.7@33.4 sample; see Figure 1.9E). Inset: SEM image of the corresponding particle. The diameter of this individual particle is 236.4 nm; this particular particle is larger than the average value. (B) 2-D histogram of the positions in (A) in 20 × 20 nm^2 bins. (C) 2-D model fitting results of (B). Fitted *R* is = 127.9 nm, i.e., outer diameter = 255.8 nm. (D) 1-D histogram of the positions in (A) along the *x* direction, and its empirical 1-D Gaussian fitting with FWHM = 140.8 ± 2.4 nm (E) Log scale 1-D histogram of the positions in (A) along the *x* direction, and its empirical 1-D Gaussian fitting with FWHM = 293.7 ± 5.3 nm.

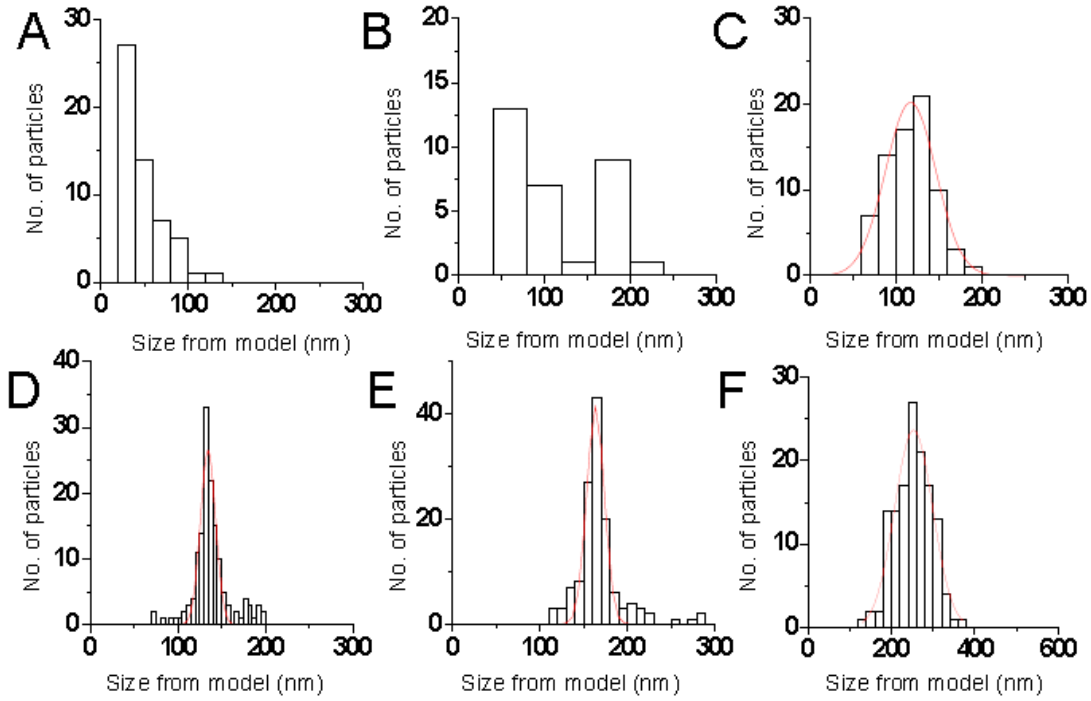

Figure 1.19 Distribution of sizes (=2*R*, where *R* is the fitted outer radius) from 2-D model fitting of the product location histograms for different sets of Au@mSiO_2 particles.
(A) 42.0@28.4 nm particles; average apparent size = 51.6 ± 23.1 nm
(B) 42.0@38.6 nm particles; average apparent size = 107. 9 ± 51.5 nm
(C) 60.4@24.5 nm particles; fitted average apparent size = 117.1 ± 58.7 nm
(D) 60.4@42.8 nm particles; fitted average apparent size = 134.4 ± 17.3 nm
(E) 101.7@33.4 nm particles; fitted average apparent size = 163.7±20.2 nm
(F) 60.4@96.8 nm particles; fitted average apparent size = 253.2 ± 91.5 nm.
The average apparent sizes and s.d. were either directly calculated from the individual values of the distributions, as for A and B, or obtained by fitting the distributions with a Gaussian distribution function when the statistics are large, as for C-F (red lines). Similar ways of obtaining the average apparent sizes were used below for Figure 1.20 and Figure 1.21.

(2) Empirical 1-D Gaussian fitting of the location histograms. This is the same as method (2) in Section 1.8.4.1. First, the 1-D histograms of catalytic events in *x* and *y* directions were obtained. Second, the histograms were fitted with a 1-D Gaussian function. The average of the two FWHMs of the fitted 1-D Gaussian functions was taken as the apparent size of the Au@mSiO_2 particle. Figure 1.18D shows the histogram and corresponding fitting curve of a pseudo-spherical 102@33

Au@mSiO$_2$ particle, whose average FWHM of *x* and *y* directions is 140.4 ± 1.9 nm. The distribution of the apparent size determined this way for all 102@33 nm Au@mSiO$_2$ particles is shown in Figure 1.20E; the average is 94.8 ± 22.5 nm. The distributions for other particle samples are shown in Figure 1.20 as well, and the average value for each set of particles is plotted in Figure 1.2E in the main text.

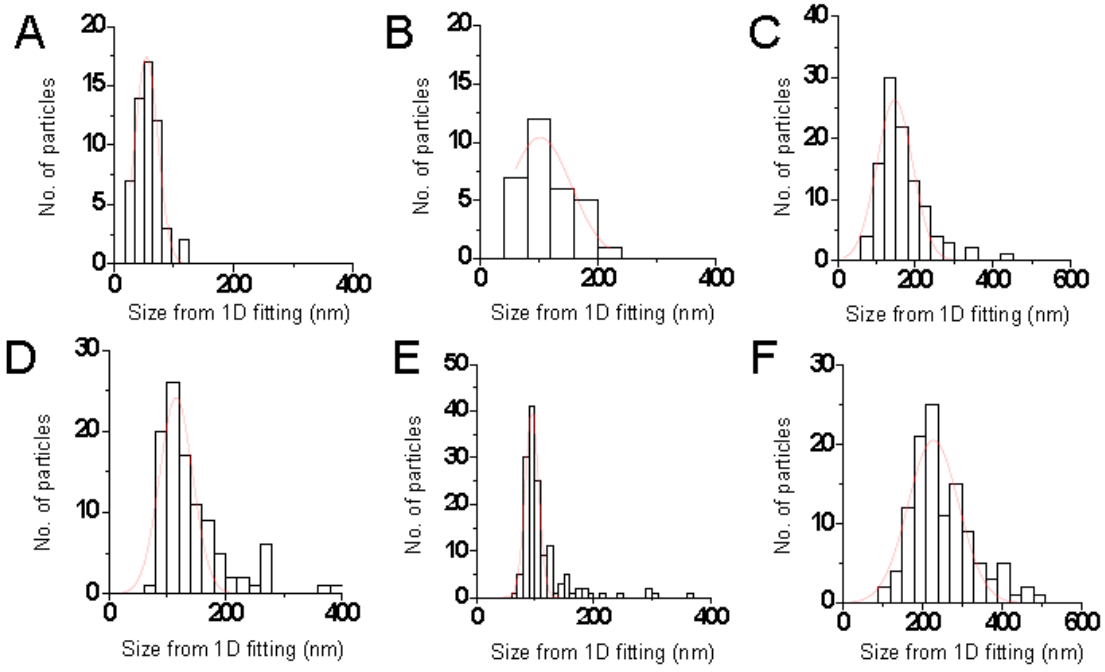

Figure 1.20 Distribution of apparent sizes from empirical 1-D Gaussian fitting of the product location histograms for different sets of Au@mSiO$_2$ particles.
(A) 42.0@28.4 nm particles; average apparent size = 54.4 ± 38.3 nm
(B) 42.0@38.6 nm particles; average apparent size = 101.4 ± 106.7 nm
(C) 60.4@24.5 nm particles; average apparent size = 146.7 ± 92.2 nm
(D) 60.4@42.8 nm particles; average apparent size = 115.3 ± 56.8 nm
(E) 101.7@33.4 nm particles; average apparent size = 94.8 ± 22.5 nm
(F) 60.4@96.8 nm particles; average apparent size = 227.4 ± 127.5 nm.

(3) Empirical 1-D Gaussian fitting of the location histograms in log-scale.

This is the same as method (3) in Section 1.8.4.1. First, the 1-D histograms of catalytic product locations in *x* and *y* directions were obtained. Second, the intensity of histograms was converted into log scale. Third, the log scale histograms were fitted

with a 1-D Gaussian function. The average of the FWHM of the 1-D Gaussian functions in *x* and *y* directions was taken as apparent size of the catalyst particle. Figure 1.18E shows the log-sale histogram and corresponding fitting curve of a 102@33nm Au@mSiO_2 particle, whose average FWHM of *x* and *y* directions is 302.4 ± 7.7 nm. The distribution of the apparent size determined this way for all 102@33 nm Au@mSiO_2 particles is shown in Figure 1.21E; the average apparent size is 225.3 ± 40.4 nm. The distributions for other Au@mSiO_2 particles are shown in Figure 1.21 as well, and the average value for each type of particles is plotted in Figure 1.2E in the main text.

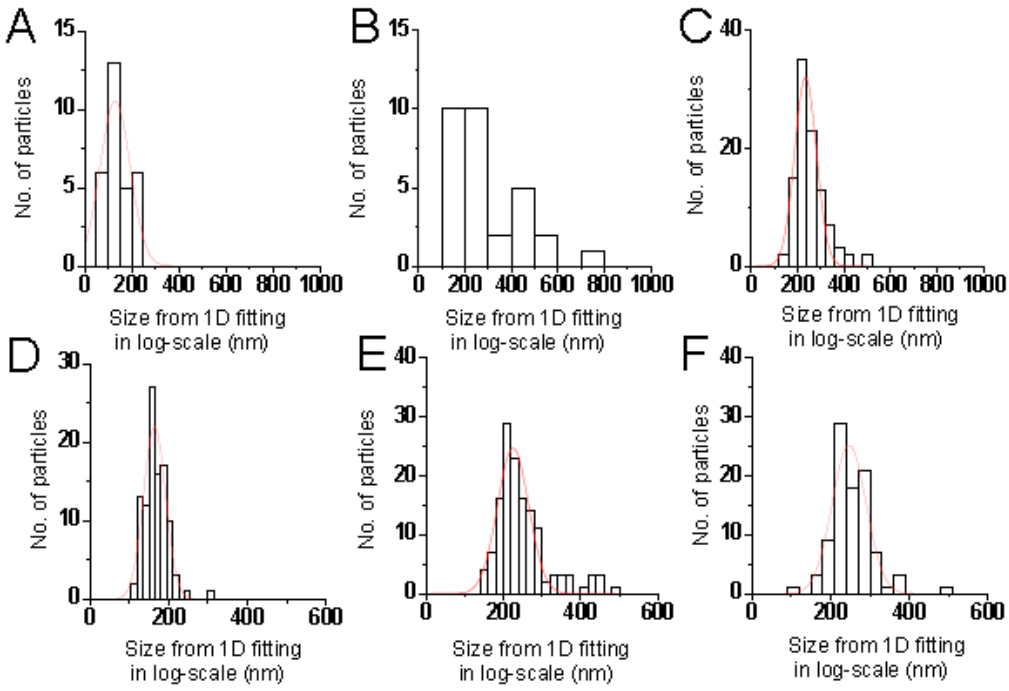

Figure 1.21 Distribution of apparent sizes from empirical 1-D Gaussian fitting of the location histograms in log-scale for different sets of Au@mSiO_2 particles.
(A) 42.0@28.4 nm particles; average apparent size = 130.2 ± 63.6 nm
(B) 42.0@38.6 nm particles; average apparent size = 286.7 ± 155.8 nm
(C) 60.4@24.5 nm particles; average apparent size = 233.2 ± 47.1 nm
(D) 60.4@42.8 nm particles; average apparent size = 164.1 ± 28.1 nm
(E) 101.7@33.4 nm particles; average apparent size = 225.3 ± 40.4 nm
(F) 60.4@96.8 nm particles; average apparent size = 247.2 ± 43.2 nm

1.8.4.3 For Au@mSiO$_2$ Nanorods

With the sub-diffraction catalysis image and the corresponding SEM image, we identified the individual Au@mSiO$_2$ nanorods and obtained their catalytic activities. We used the SEM images to obtain the size information for these nanorods, by fitting their SEM structural counters with a model that approximates the nanorod as a cylinder of length *l* capped with two hemispheres of radius *R*. This model, its validation, and the fitting procedure were detailed in our previous publication[3]. The overall length of a nanorod is then $L = l + 2R$. The aspect ratio of a Au@mSiO$_2$ nanorod was taken as $L/2R$, which was presented in Figure 1.4D in the main text.

1.8.5 Additional Results for the Activity Screening of a Mixture of Pseudo-spherical Au@mSiO$_2$ Catalyst Particles in Catalyzing the Reductive N-deoxygenation of Resazurin to Resorufin

The mixture of pseudo-spherical Au@mSiO$_2$ particles of 21@42 and 102@32 nm in size were made by synthesizing them separately and mixing them together afterwards. The TEM image of each sample is shown in Figure 1.22; their size measurements are shown in Figure 1.23. This section also presents more statistical analyses of the activity of individual particles in catalyzing the reductive N-deoxygenation reaction of resazurin presented in Figure 1.3A in the main text. These additional statistical analyses include analyzing the distributions of individual catalyst particles along the dimension of their apparent sizes from the sub-diffraction catalysis imaging, SEM diameter, and activity (Figure 1.24 - Figure 1.26). The catalytic activity screening in Figure 1.3A was done with the following reaction conditions: [Resazurin] = 50 nM, [NH_2OH] = 1 mM, and pH = 7.3.

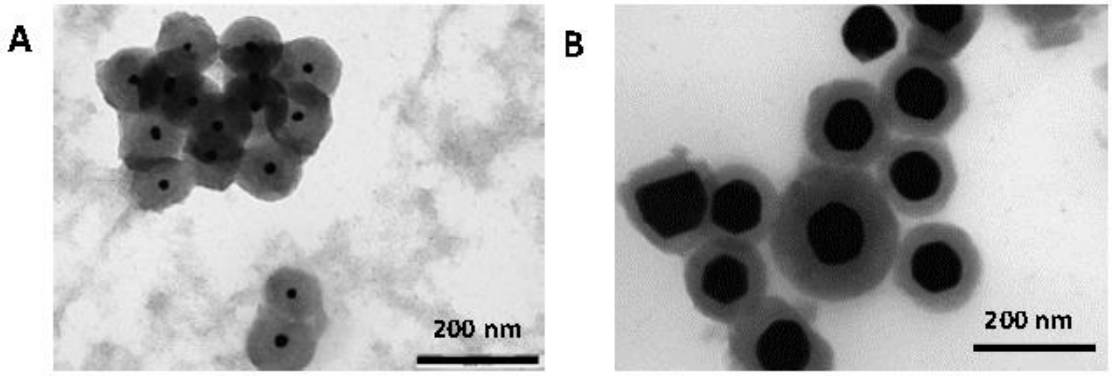

Figure 1.22 TEM images of 21@42 and 102@32 nm (core-diameter@shell-thickness) pseudo-spherical Au@mSiO_2 particles

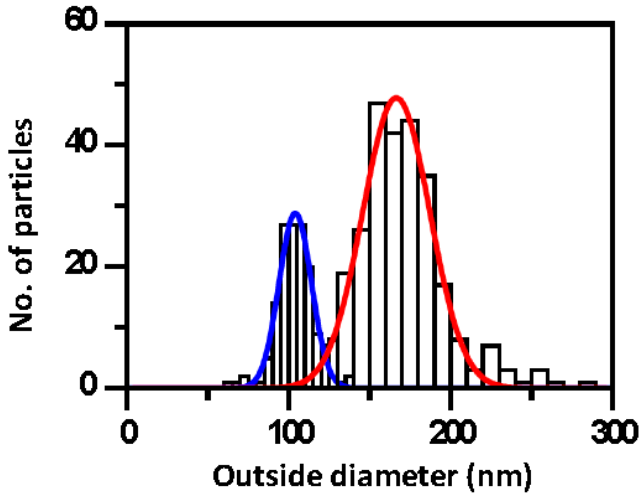

Figure 1.23 Outside diameter distribution from TEM (Figure 1.22) for the Au@mSiO_2 pseudo-spherical particles with core sizes of 21.0 ± 2.0 and 101.7 ± 6.7 nm. The outside diameter is 104.0 ± 19.9 and 166.5 ± 141.5 nm, respectively, determined from Gaussian fitting the distributions (red and blue lines). The error bar is s.d. of the fitted Gaussian distribution. There are 153 and 257 particles for the core sizes of 21.0 ± 2.0 and 101.7 ± 6.7 nm, respectively. These two types are denoted as 21@42 nm and 102@32 nm (Table 1.1), as in the text and in Figure 1.22.

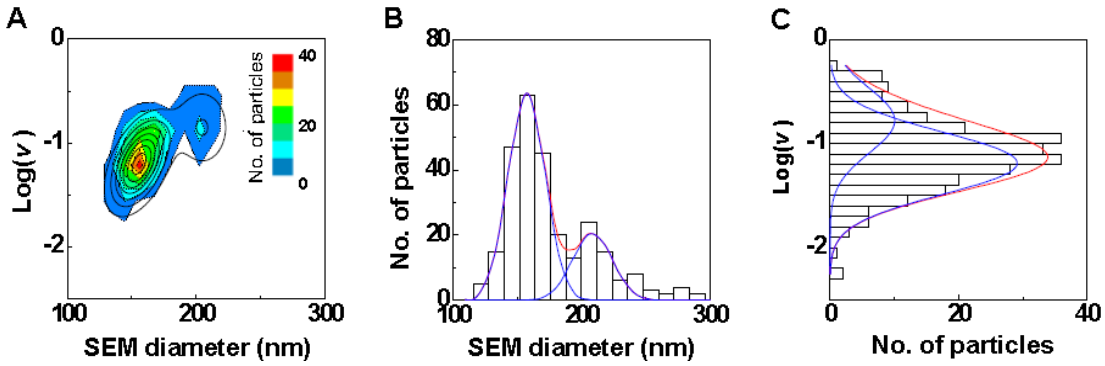

Figure 1.24 Correlation between the SEM diameter and log(*v*) from the parallel activity screening of a mixture of pseudo-spherical 21.0@41.5 nm, 101.7@32.4 nm Au@mSiO_2 particles in the reductive N-deoxygenation reaction of resazurin. *v* is the rate of turnover in s^{-1} $particle^{-1}$. Reaction condition: [Resazurin] = 50 nM. [NH_2OH] = 1 mM. pH = 7.30. (A) Contour plot of the 2-D histogram (bins size: 20 nm × 0.25) of the catalyst particles along the dimension of log(*v*) and the diameter determined from SEM. The color contour plot is the experiment data; the black lines are the fitting result using two 2-D Gaussian functions centered at (157.6 nm, -1.19) and (208.7 nm, -0.78). (B,C) Corresponding 1-D histograms for A along the dimension of SEM diameter (B) and log(*v*) (C), respectively. The blue solid lines are global fits with two Gaussian functions. The red lines are the sums of fitted Gaussian functions. The distributions reveal two subpopulations, corresponding to the mixture of two types of particles, with population ratio of about 2.89 : 1.

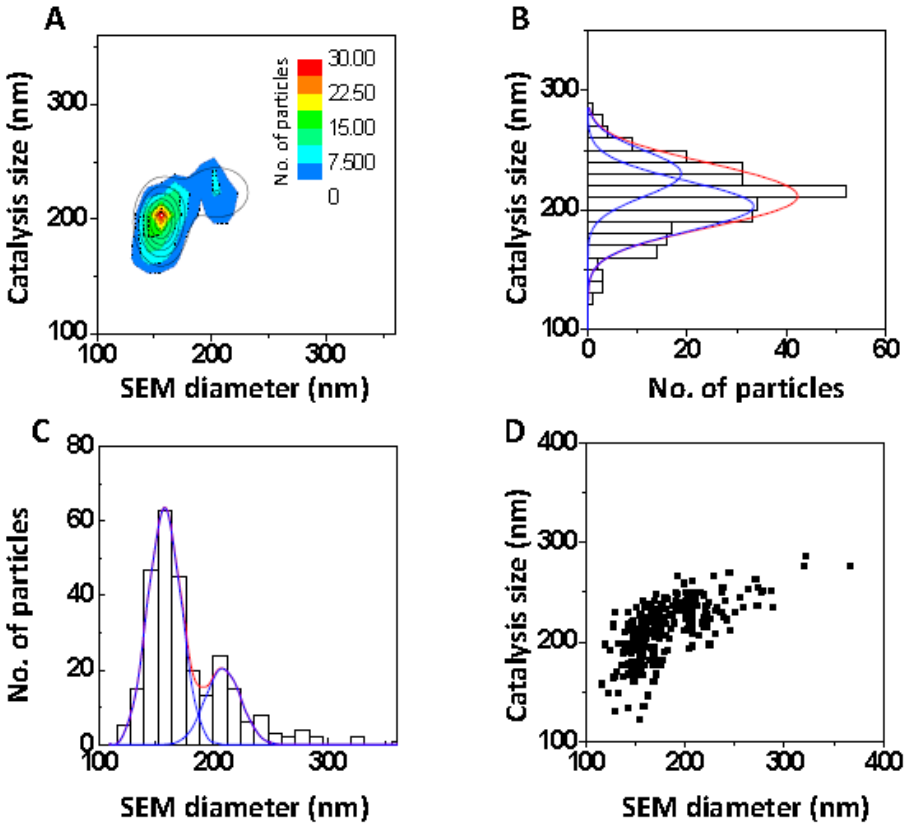

Figure 1.25 Correlation between the SEM diameter and the apparent size from the sub-diffraction catalysis imaging (via 1-D Gaussian fitting of log-scale location histogram) from the parallel activity screening of a mixture of pseudo-spherical 21.0@41.5 nm, 101.7@32.4 nm Au@mSiO_2 particles in the reductive N-deoxygenation reaction of resazurin.(A) Contour plot between catalysis size and SEM diameter. Bin size: 20 × 20 nm^2. The solid black lines are fits with two 2-D Gaussian functions centered at (157.6 nm, 202.9 nm) and (208.7 nm, 230.5 nm), respectively. (B) Histogram of apparent catalysis size and Gaussian resolutions. (C) Histogram of SEM diameter and Gaussian fittings. (D) Scatter plot of individual catalyst particles against their respective SEM diameter and apparent catalysis size. Each point represents one particle. Total number of particles = 275.

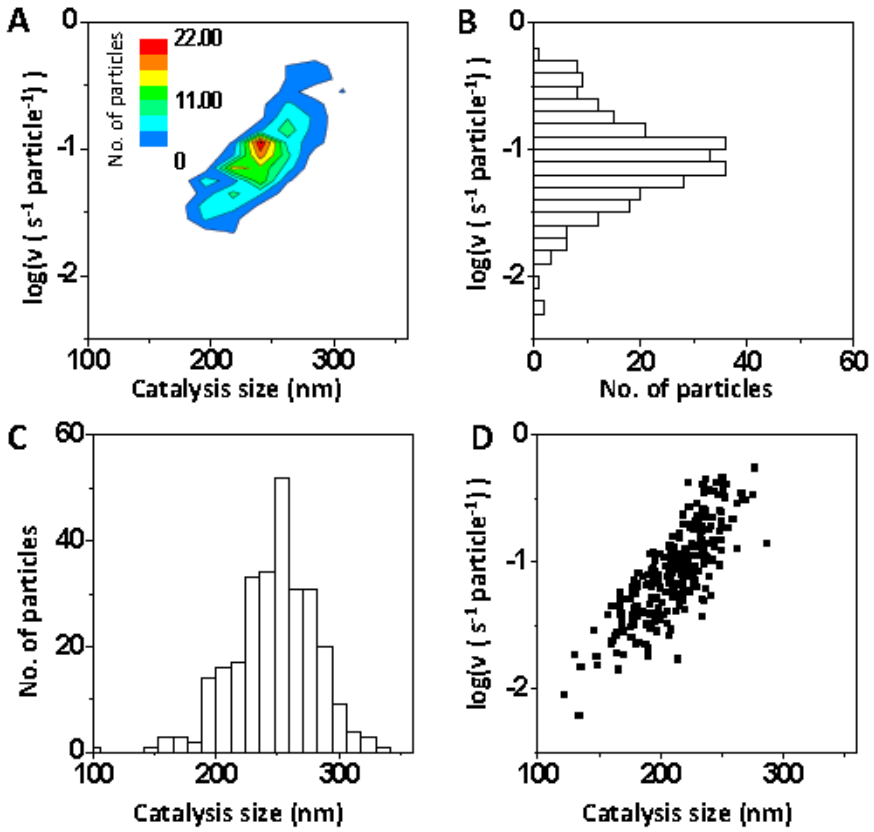

Figure 1.26 Correlation between the apparent size from the sub-diffraction catalysis imaging (via 1-D Gaussian fitting of log-scale location histogram) and log(*v*) from the parallel activity screening of a mixture of pseudo-spherical 21.0@41.5 nm, 101.7@32.4 nm Au@mSiO_2 particles in the reductive N-deoxygenation reaction of resazurin. (A) Contour plot of 2-D histograms of individual particles along catalysis size and rate of turnovers (i.e., *v*, in s^{-1} $particle^{-1}$ in log scale). Bin size: 20 nm × 0.25. (B) 1-D histogram of log(*v*) among individual particles. (C) 1-D histogram of catalysis size of individual particles. (D) Scatter plot of catalysis size and rate of turnovers (i.e., *v*, in s^{-1} $particle^{-1}$ in log scale) for individual catalyst particles. Each point represents one particle. Total number of particles = 275.

1.8.6 Additional Results on the Parallel Screening of a Mixture of Pseudo-spherical Au@mSiO_2 Particles in Catalyzing the Oxidative N-deacetylation Reaction of Amplex Red to Resorufin

This section presents more statistical analyses of the activity of individual particles in catalyzing the oxidative N-deacetylation reaction of amplex red, using a mixture of pseudo-spherical Au@mSiO_2 particles of 21@42 and 102@32 nm in size

(Figure 1.22). The global sub-diffraction catalysis image is shown in Figure 1.27A along with the corresponding SEM image of the same area of the sample (Figure 1.27B). The statistical analysis of individual particles regarding their activities and SEM diameters is presented in Figure 1.3E and F in the main text. Below are additional statistical analyses that include analyzing the distributions of individual catalyst particles along the dimensions of their apparent sizes from the sub-diffraction catalysis imaging, SEM diameter, and activity (Figure 1.27 - Figure 1.29). The reaction conditions for the activity screening are: [Amplex red] = 200 nM, [H_2O_2] = 60 mM, pH = 7.3.

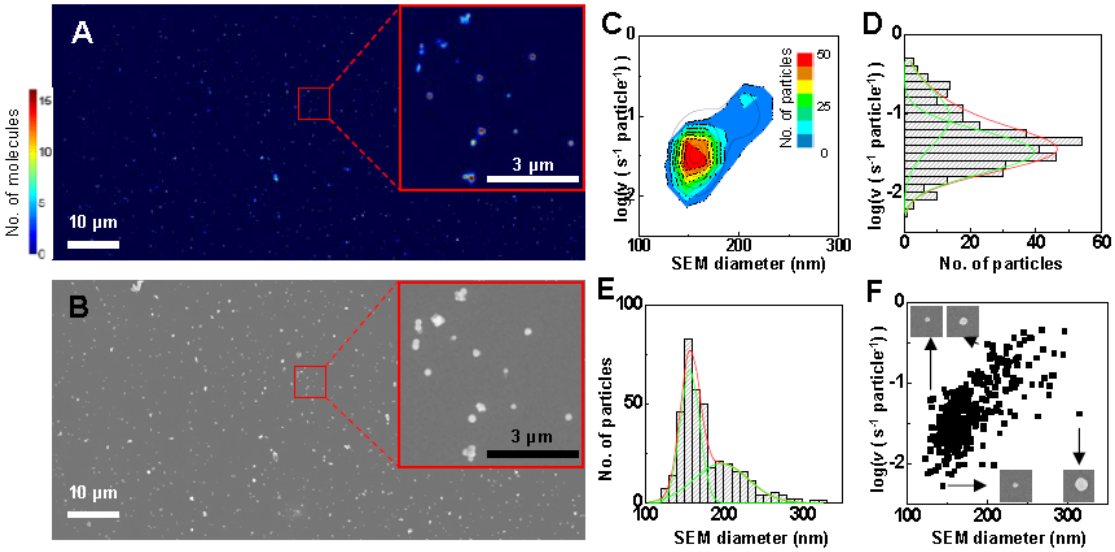

Figure 1.27 Parallel activity screening of a mixture of pseudo-spherical 21@42 nm and 102@32 nm Au@mSiO_2 particles in catalyzing the oxidative N-deacetylation of amplex red (AR) to resorufin. Reaction condition: [AR] = 200 nM, [H_2O_2] = 60 mM, pH = 7.3. (A) Sub-diffraction catalysis image of ~700 particles with 20 × 20 nm^2 bins in forming the histogram. Inset is a zoom in of a region. (B) SEM image of the same set particles as in A. (C) Contour plot of the 2-D histogram of individual particles along their SEM diameter and log(v) in F. (*v* is in s^{-1} $particle^{-1}$). Bin size: 20 nm × 0.25. The solid black lines are fits with two 2-D Gaussian functions centered at (157.0 nm, -1.48) and (203.3 nm, -0.99), respectively. (D) 1-D histogram of log(v) of individual particles and Gaussian resolutions. The blue lines are the 1-D Gaussian fitting for two species. The red line is the combination of these two blue lines. (E) 1-D histogram of SEM diameter of individual particles and Gaussian resolution. The blue lines are the 1-D Gaussian fitting for two species. The red line is the combination of these two blue lines. (F) Scatter plot of individual catalyst particles against their respective SEM diameter and rate of turnovers (i.e., *v*, in s^{-1} $particle^{-1}$ in log scale) from A. Each point represents one particle. Only isolated particles are included in the histogram, excluding those in aggregates. Total number of particles = 382.

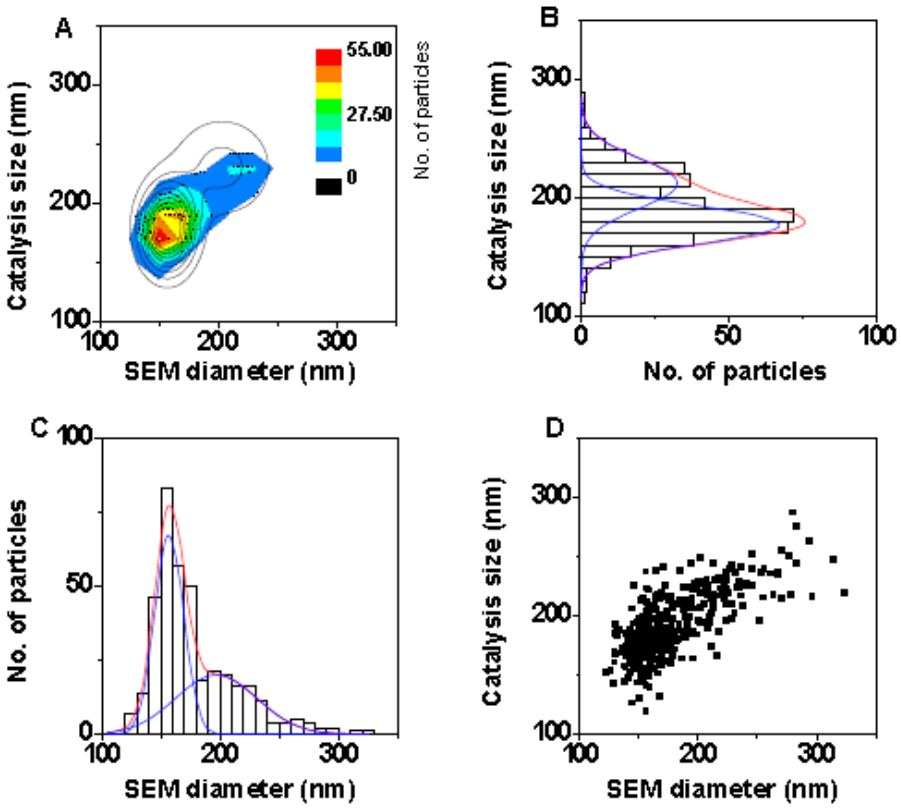

Figure 1.28 Correlation between SEM diameter and apparent catalysis size (via 1-D Gaussian fitting of log-scale location histogram) for the mixture of pseudo-spherical Au@mSiO_2 particles in Figure 1.27A and B. Again, only isolated particles were included. (A) Contour plot of the 2-D histogram of individual particles along their apparent catalysis size and SEM diameter. Bin size: 20 nm × 20 nm. The solid black lines are fits with two 2-D Gaussian functions centered at (157.0 nm, 177.7 nm) and (203.3 nm, 214.6 nm), respectively. (B) 1-D histogram of apparent catalysis size of individual particles and Gaussian resolutions. The blue lines are the 1-D Gaussian resolutions for two sub-populations. The red line is the combination of these two blue lines. (C) 1-D histogram of SEM diameter of individual particles and Gaussian resolutions. The blue lines are the 1-D Gaussian resolutions for two subpopulations. The red line is the combination of these two blue lines. (D) Scatter plot of individual catalyst particles against their respective SEM diameter and apparent catalysis size. Each point represents one particle. Total number of particles = 382.

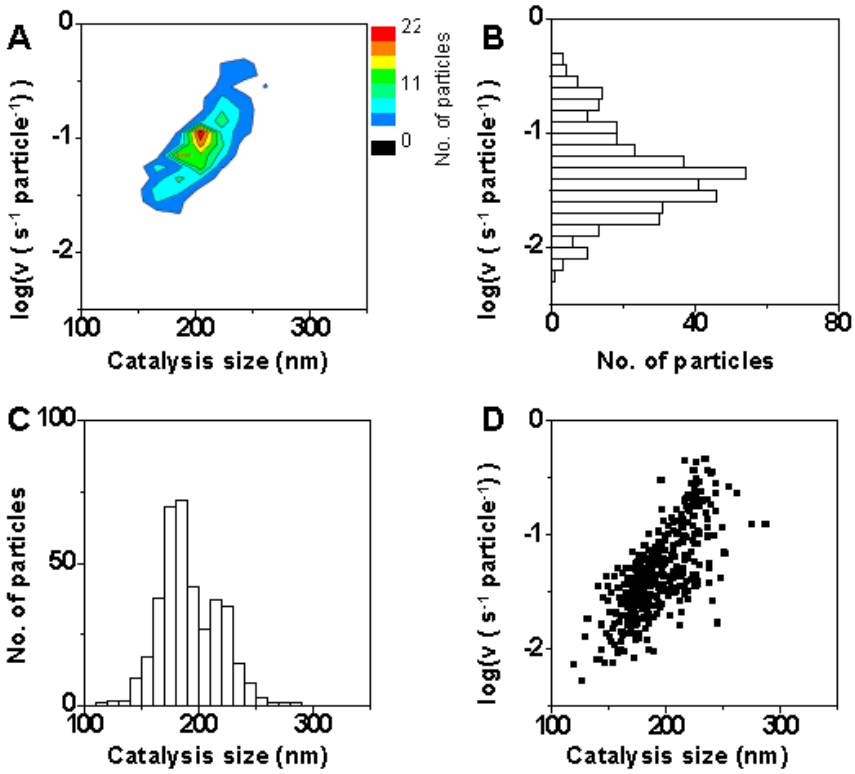

Figure 1.29 Correlation between apparent catalysis size (via 1-D Gaussian fitting of log-scale location histogram) and catalytic activity in log(*v*) for the mixture of pseudo-spherical Au@mSiO$_2$ particles in Figure 1.27A and B. (A) Contour plot of the 2-D histogram of individual particles along the apparent catalysis size and log(*v*). Bin size: 20 nm × 0.25. (B) 1-D histogram of log(*v*). (C) 1-D histogram of apparent catalysis size. (D) Scatter plot of individual catalyst particles against their respective apparent catalysis size and rate of turnovers (i.e., *v*, in s^{-1} $particle^{-1}$ in log scale). Each point represents one particle. Total number of particles = 382.

1.8.7 Additional Results on the Parallel Screening of a Mixture of Pseudo-spherical, Triangular, and Rod-shaped Au@mSiO$_2$ Particles in Catalyzing the Oxidative N-deacetylation Reaction of Amplex Red to Resorufin

Figure 1.30 presents the TEM images of the mixture containing pseudo-spherical, triangular, and rod-shaped Au@mSiO$_2$ particles and the structural measurements of the outer diameter of particles. The global sub-diffraction catalysis image is shown in Figure 1.31A along with the corresponding SEM image of the same area of the sample (Figure 1.31B) for catalyzing the oxidative N-deacetylation

reaction of amplex red to resorufin. This section also presents the additional statistical analyses of individual particles including the distributions of individual catalyst particles along the dimensions of their apparent sizes from the sub-diffraction catalysis imaging, SEM diameter, and activity (Figure 1.31 - Figure 1.33). The reaction conditions for the activity screening are: [Amplex red] = 200 nM, [H_2O_2] = 60 mM, and pH = 7.3.

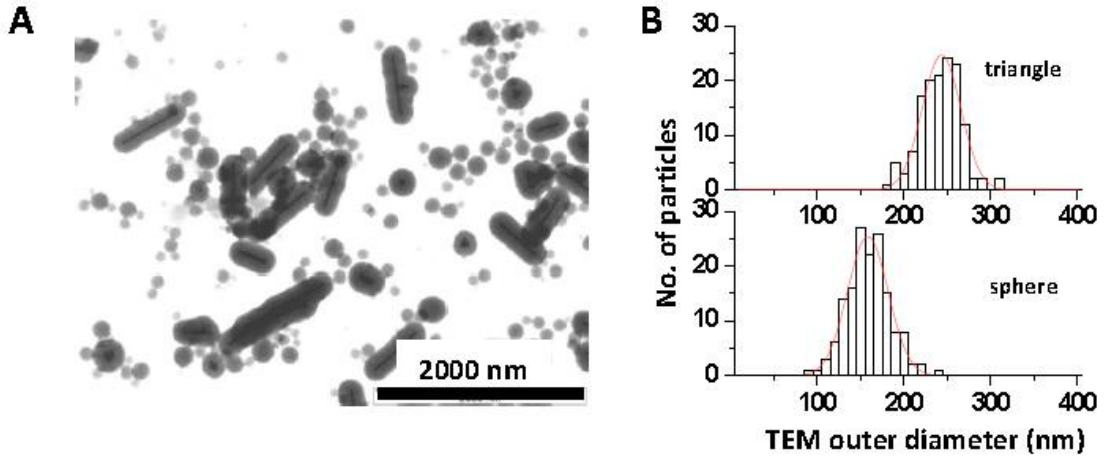

Figure 1.30 (A) TEM image of a mixture of pseudo-spherical, small triangular, and rod-shaped Au@mSiO_2 particles. (B) Size (diameter) distribution of pseudo-spherical and triangular particles. The Gaussian fitted centers of them are 158.3 ± 47.0 nm and 243.3 ± 44.5 nm, respectively, for the pseudo-spherical and triangular particles. The red lines are 1-D Gaussian fittings.

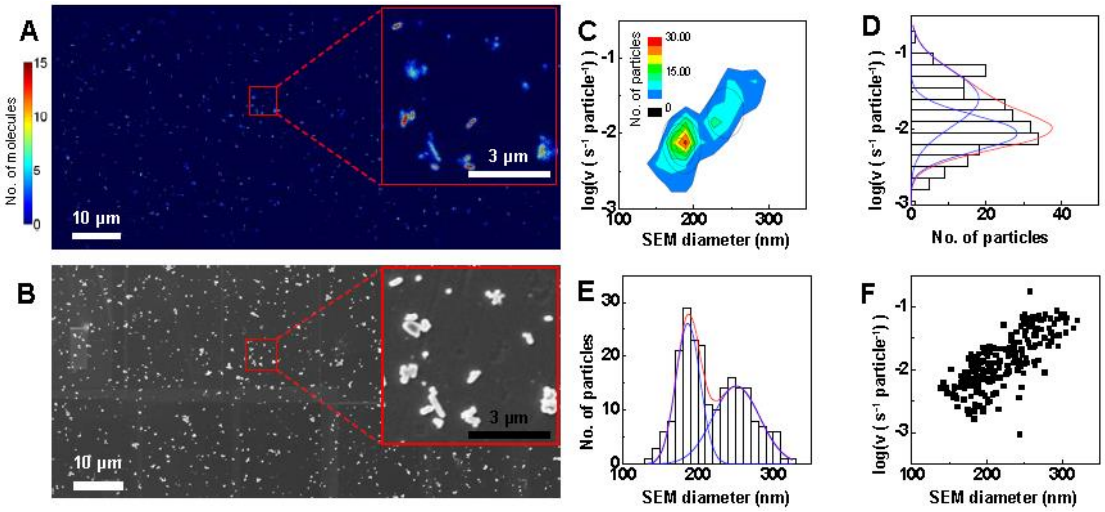

Figure 1.31 Parallel activity screening of a mixture of pseudo-spherical, small triangular, and rod-shaped Au@mSiO_2 particles in catalyzing the oxidative N-deacetylation of amplex red (AR) to resorufin. [AR] = 200 nM, [H_2O_2] = 60 mM, pH = 7.3. (A) Sub-diffraction catalysis image of ~900 particles, with 20 × 20 nm^2 bins in forming the histogram. Inset is a zoom in of a region. (B) SEM image of the same set particles as in A. The triangular and pseudo-spherical Au@mSiO_2 particles are largely differentiable. (C, D, E, F) Correlation between the SEM diameter and log(v) for the pseudo-spherical and triangular particles (the shapes of these two types cannot be differentiated well in the SEM image): (C) Contour plot of the 2-D histogram of 221 particles along the dimensions of the SEM diameter and log(v) in F. Bin size: 20 nm × 0.25. The solid black lines are fits with two 2-D Gaussian functions centered at (187.6 nm, -2.05) and (252.0 nm, -1.58), respectively. The two populations likely correspond to the triangular and pseudospherical particles, which are difficult to distinguish by shape but differ in size (see also Figure 1.30B). (D) Histogram of log(v) and Gaussian resolutions. The blue lines are the fittings of two Gaussians. The red line is the sum of these two blue lines. (E) Histogram of the diameter from SEM and Gaussian resolutions. (F) Scatter plot of individual catalyst particles against their respective SEM diameter and rate of turnovers (i.e., v, in s^{-1} $particle^{-1}$ in log scale). Each point represents one particle. Only isolated particles are included here. Total number of particles = 221.

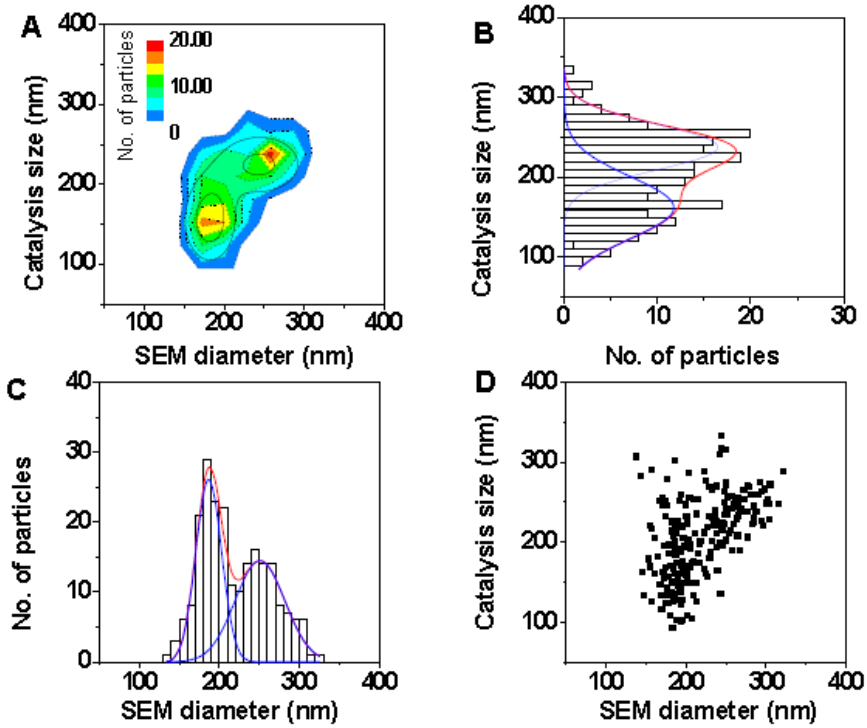

Figure 1.32 Correlation between SEM diameter and the apparent catalysis size from the sub-diffraction catalysis imaging (via 1-D Gaussian fitting of log-scale location histogram) for the mixture of pseudo-spherical and triangular Au@mSiO_2 particles from Figure 1.31A and B. (A) Contour plot between catalysis size and SEM diameter. Bin size: 20 × 20 nm^2. The solid black lines are fits with two 2-D Gaussian functions centered at (186.9 nm, 162.2 nm) and (250.8 nm, 237.8 nm), respectively. (B) 1-D histogram of apparent catalysis size (via 1-D Gaussian fitting of log-scale location histograms) of individual particles. (C) 1-D histogram of SEM diameter of individual particles; same as Figure 1.31E. The peak positions and widths of Gaussian resolution in A-C are consistently fitted with one another. (D) Scatter plot of individual catalyst particles against their respective SEM diameter and catalysis size. Each point represents one particle. Total number of particles = 221.

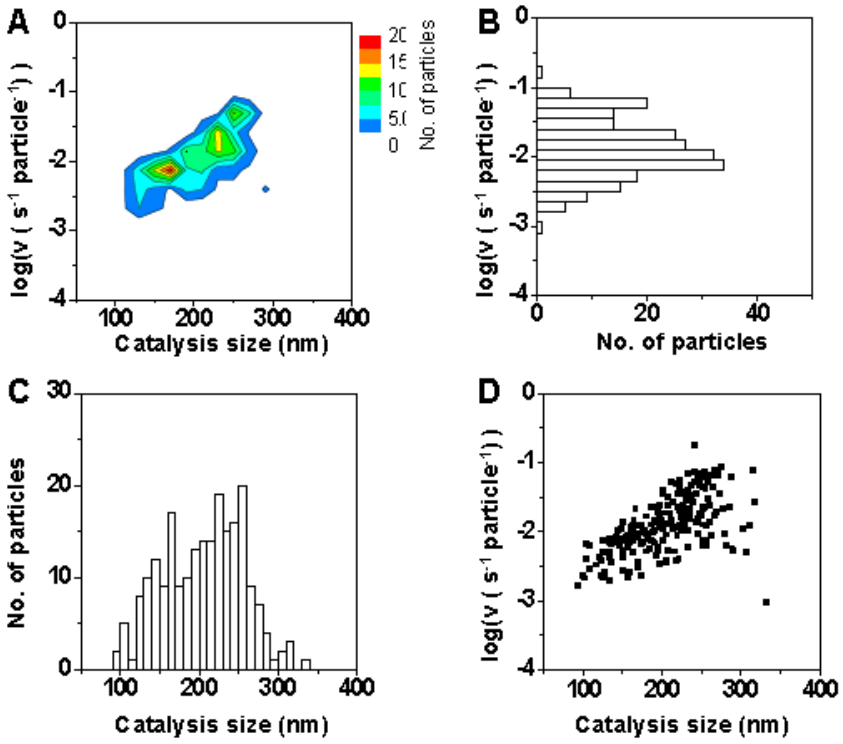

Figure 1.33 Correlation between the apparent catalysis size (via 1-D Gaussian fitting of log-scale location histogram) and reaction rate in log-scale for the mixture of pseudo-spherical and triangular particles from Figure 1.31A and B. (A) Contour plot of the 2-D histogram of D. Bin size: 20 nm × 0.25. (B) Same as Figure 1.31D. (C) Same as Figure 1.32B. (D) Scatter plot of individual catalyst particles against their respective apparent catalysis size and rate of turnovers (i.e., v, in s^{-1} $particle^{-1}$ in log scale). Each point represents one particle. Total number of particles = 221.

1.8.8 Additional Results on the Catalytic Activity Correlation Between Different Reactions at the Ensemble Level

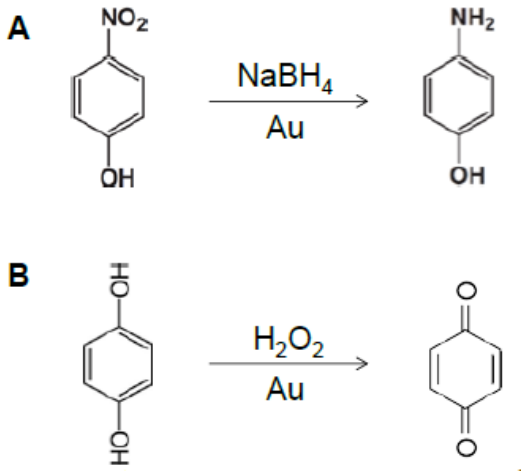

Figure 1.34 Schemes of the Au particle catalyzed: (A) reduction of 4-nitrophenol by $NaBH_4$ and (B) oxidation of hydroquinone by H_2O_2.

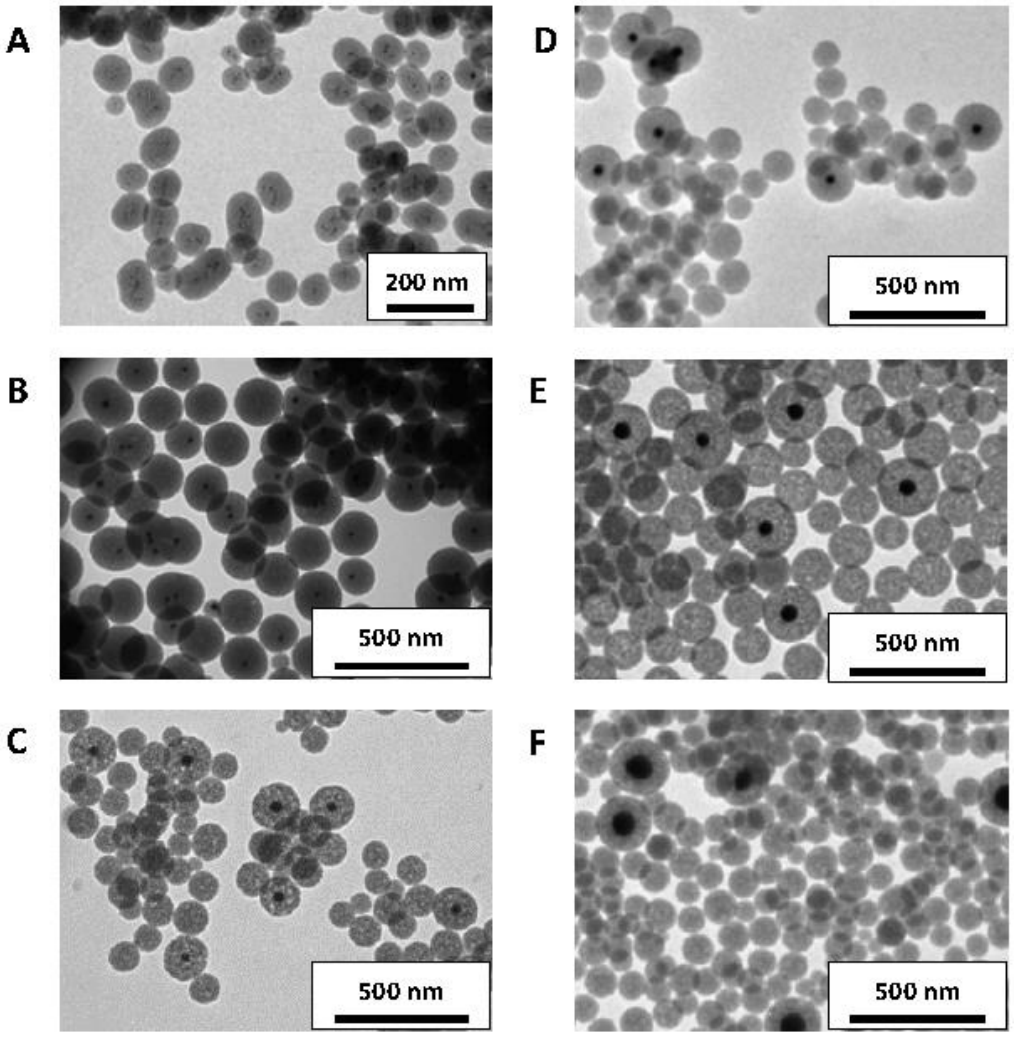

Figure 1.35 TEM images of pseudo-spherical Au@mSiO_2 particles for ensemble activity correlation experiments. See also Table 1.1 for their abbreviated names referred to in the text.
(A) 6.0@37.5 nm (core-diameter@shell-thickness)
(B) 21.0@80.6 nm
(C) 42.0@65.4 nm
(D) 42.0@70.3 nm
(E) 60.4@82.8 nm
(F) 101.7@58.6 nm
Note some silica particles do not contain a Au particle core. These do not affect our ensemble measurements, as the Au particle concentrations were calibrated experimentally by measuring the UV-Vis extinction spectra at the surface plasmon resonance peak of the Au particles.

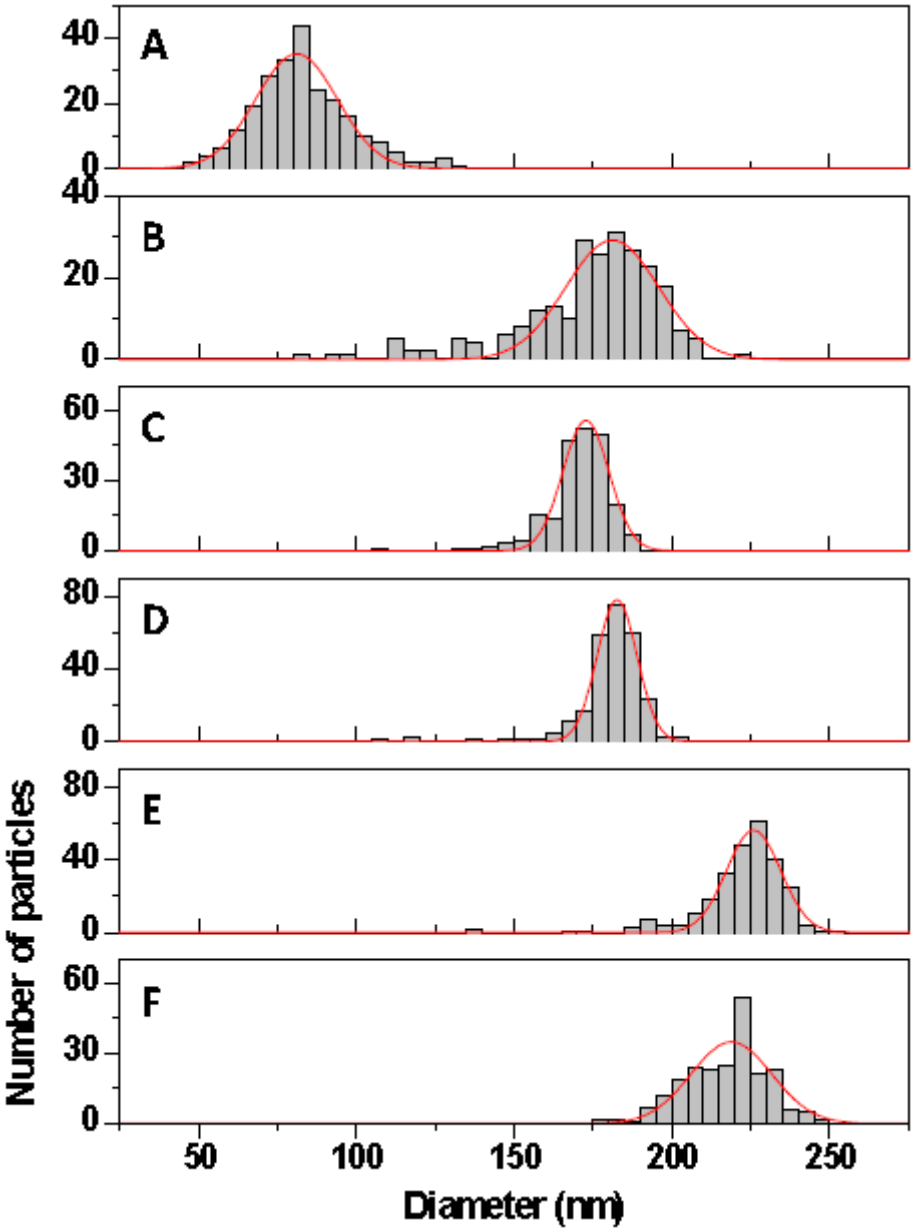

Figure 1.36 TEM outer diameter distributions for particles in Figure 1.35. See also Table 1.1 for their abbreviated names referred to in the text.
(A) 6.0@37.5 nm. Average outer diameter = 81.0 ± 25.9 nm out of 240 particles.
(B) 21.0@80.6 nm. Average outer diameter = 181.0 ± 29.5 nm out of 237 particles.
(C) 42.0@65.4 nm. Average outer diameter = 172.8 ± 14.7 nm out of 217 particles.
(D) 42.0@70.3 nm. Average outer diameter = 182.6 ± 12.7 nm out of 263 particles.
(E) 60.4@82.8 nm. Average outer diameter = 225.9 ± 17.2 nm out of 264 particles.
(F) 101.7@58.6 nm. Average outer diameter = 218.9 ± 25.6 nm out of 226 particles.

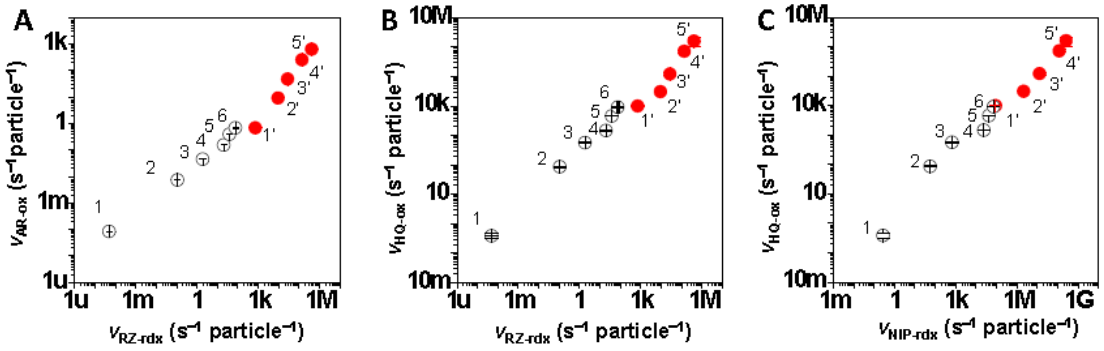

Figure 1.37 Activity correlation between different reactions for bare Au and Au@mSiO$_2$ catalyst particles. (A) Activity in the oxidative N-deacetylation reaction of amplex red (AR-ox) versus in the reductive N-oxygenation reaction of resazurin (RZ-rdx). (B) Activity in the hydroquinone oxidation reaction (HQ-ox) versus in the reductive N-oxygenation of resazurin (RZ-rdx). (C) Activity in the hydroquinone oxidation reaction (HQ-ox) versus in the nitrophenol reduction reaction (NIP-rdx). The black circles are Au@mSiO$_2$ catalyst particles, while the red dots are bare Au ones. The same series of catalyst particles are presented here as those in Figure 1.5 in the main text.

1.8.9 Supporting Information References

(1) X. Zhou, W. Xu, G. Liu, D. Panda & P. Chen. Size-dependent catalytic activity and dynamics of gold nanoparticles at the single-molecule level. *Journal of the American Chemical Society* **132**, 138-146 (2010).

(2) N. R. Jana, L. Gearheart & C. J. Murphy. Wet chemical synthesis of high aspect ratio cylindrical gold nanorods. *J. Phys. Chem. B* **105**, 4065-4067 (2001).

(3) X. Zhou, N. M. Andoy, G. Liu, E. Choudhary, K.-S. Han, H. Shen & P. Chen. Quantitative super-resolution imaging uncovers reactivity patterns on single nanocatalysts. *Nature Nanotech.* **7**, 237–241 (2012).

(4) W. Stöber, A. Fink & E. Bohn. Controlled growth of monodisperse silica spheres in the micron size range. *J. Coll. Interf. Sci.* **26**, 62-69 (1968).

(5) L. M. Liz-Marzán, M. Giersig & P. Mulvaney. Synthesis of nanosized gold−silica core−shell particles. *Langmuir* **12**, 4329–4335 (1996).

(6) P. Botella, A. Corma & M. T. Navarro. Single gold nanoparticles encapsulated in monodispersed regular spheres of mesostructured silica produced by pseudomorphic transformation. *Chem. Mater*. **19**, 1979–1983 (2007).

(7) B. Nikoobakht & M. A. El-Sayed. Evidence for bilayer assembly of cationic surfactants on the surface of gold nanorods. *Langmuir* **17**, 6368-6374 (2001).

(8) X. Zhou, N. M. Andoy, G. Liu, E. Choudhary, K.-S. Han, H. Shen & P. Chen. Quantitative super-resolution imaging uncovers reactivity patterns on single nanocatalysts. *Nature Nanotechnology* **7**, 237-241 (2012).

(9) R. E. Thompson, D. R. Larson & W. W. Webb. Precise nanometer localization analysis for individual fluorescent probes. *Biophys. J.* **82**, 2775-2783 (2002).

CHAPTER TWO

Synthesis and Characterization of Bimetallic Au/Pt and Au/Pd Nanocatalysts for Measuring Interfacial Catalytic Activity

2.1 Abstract

Bimetallic nanocatalysts can show increased catalytic activity over their monometallic counterparts. However, the introduction of a second metal into the nanoparticle introduces another degree of heterogeneity into an already diverse system, thus making their study desirable at the single particle level. Furthermore, it is natural to assume that the bimetallic enhancement will be greatest at the interface between the two metals. In an effort to understand the origin of this enhanced performance, bimetallic catalyst systems were synthesized with various interface structures between the two metals. Templated electrodeposition was used to synthesize AuPt segmented nanorods. Photolithography and thin film deposition were used to make intersecting arrays of Au and Pt stripes, and colloidal synthesis was used to create AuPd core-shell nanorods. The progress of the synthesis and characterization of these model bimetallic nanostructures is detailed in this chapter. The goal of the study was to use single-molecule fluorescence microscopy to spatially resolve the catalytic activity within the bimetallic nanostructures, enabling a comparison of the interface versus the non-interface regions. This work could eventually lead to a better understanding of microscopic bimetallic structure/activity correlations and enable the design of next generation catalysts.

2.2 Introduction

Nanoparticles are important catalysts. In an effort to achieve better resource economy, longer stability, resistance to poisons, higher selectivity, and tunable and increased performance, bimetallic particles offer advantages over their single component counterparts. By mixing two components together new properties are accessible because the introduction of a new metal will affect the electronic properties of neighboring atoms, which can affect the properties of adsorbates. Furthermore, the degree to which these properties are changed is tunable based on the composition of the two metals.[1-5] Additionally, bimetallic particles can have improved performance from synergistic effects as part of a bifunctional mechanism, in which each metal preferentially adsorbs different reactants and brings them in to close proximity or one metal is responsible for adsorption and catalytic transformation and the other allows for desorption.[6-9]

Alloys are commonly used bimetallic structures since they are simple to make with a variety of compositions. However, they are difficult to study at the reactive site level since there are a tremendous number of different microscopic arrangements of the two metal atoms and varying degrees of segregation are possible depending on the conditions, which could yield core-shell type structures.[5,10] In order to study the effect the two metals have on each other in terms of catalytic activity, it is important to study the interface region as this is where the synergistic and electronic effects have their influence. Studying the interface directly in a mixed alloy would require atomic characterization of the particle surface combined with subnanometer catalytic activity resolution. To get around this challenge, my research uses two approaches to make model metal-metal interfaces to be studied. In one approach, by making a segmented

nanorod with one half made entirely of one metal and the second half made entirely of another metal, a well-defined interface between the two is established. Alternatively, photolithography combined with metal evaporation can be used to make intersecting stripes of the two metals. The single molecule fluorescence imaging technique can be used to measure catalytic activity at tens of nanometers spatial resolution. This means that the non-interface region in the entire particle needs to be many times larger than the spatial resolution to be differentiated from the interface region. By using templated electrodeposition to synthesize the segmented nanorods, the lengths of the two segments can easily be tuned by controlling the charge passed and thus the amount of metal deposited. For lithographically produced stripes, sizes down to a few hundred nanometers can easily be made.

Although the bimetallic effect is greatest at the metal-metal interface region, it can also be measured indirectly by measuring core-shell nanoparticle behavior as a function of shell thickness for a fixed core sample. In this case, since only one metal is exposed to the surface, a bifunctional mechanism is not possible, but the electronic effects from the core metal on the shell still can affect its catalytic behavior. At monolayer coverage this effect is most pronounced and with thick shell coverage, the effect of the core is lost. By studying the catalytic activity as a function of shell thickness, the length scale of the effect of the interface, although buried, can be probed which can still lead to new insight for future catalyst design. This is another aspect of my research which will be described below.

2.3 Electrodeposition to Generate Segmented Au/Pt Nanorods

The first system I use to study catalysis at bimetallic interfaces is segmented nanorods produced by templated electrodeposition. This templated electrodeposition method is widely reported in the literature using anodic aluminum oxide (AAO) as the template structure. AAO is well suited for this use due to its parallel cylindrical nanopore structure and since it can be easily removed by dissolving in basic solution.[8,11,12] In order to measure the catalytic activity using the single molecule fluorescence microscopy technique, it is necessary to have catalytic reactions yielding fluorescent product molecules. Previous work in the Chen lab has shown that resorufin, a fluorescent molecule, can be catalytically generated on Au and Pt with the appropriate reactants.[13,14] For these reasons, segmented Au/Pt rods are the target system of my research. These rods have previously been synthesized and reported in the literature for use as bifunctional nanoscale building blocks and for catalytic self-propelled nanomotors in hydrogen peroxide solution.[15-17]

2.3.1 Overview of Templated Electrodeposition in AAO Templates for Making Segmented Nanorods

The first step in making the nanorods is to add a conducting electrode onto one side of the template. This is achieved by evaporating silver onto the AAOs. This conducting layer is blocked from the back so that only the solution in the nanopores can interact with the electrode. Then the template is placed in a bath with silver nitrate and silver is electrodeposited into the pores by applying an appropriate potential. This step is to partially fill the pores and provide a smooth electrode for the subsequent steps. Then the template is thoroughly rinsed and placed into a bath with the desired

metal salt present and more metal is deposited. This step can be repeated with different metals as desired. After the deposition of the rods is complete, the silver electrode and template are removed. The silver is removed by dissolution in nitric acid, and the AAO template is removed by dissolution in a basic aqueous solution. The rods can then be collected by centrifugation and further purified. This process is shown in Figure 2.1.

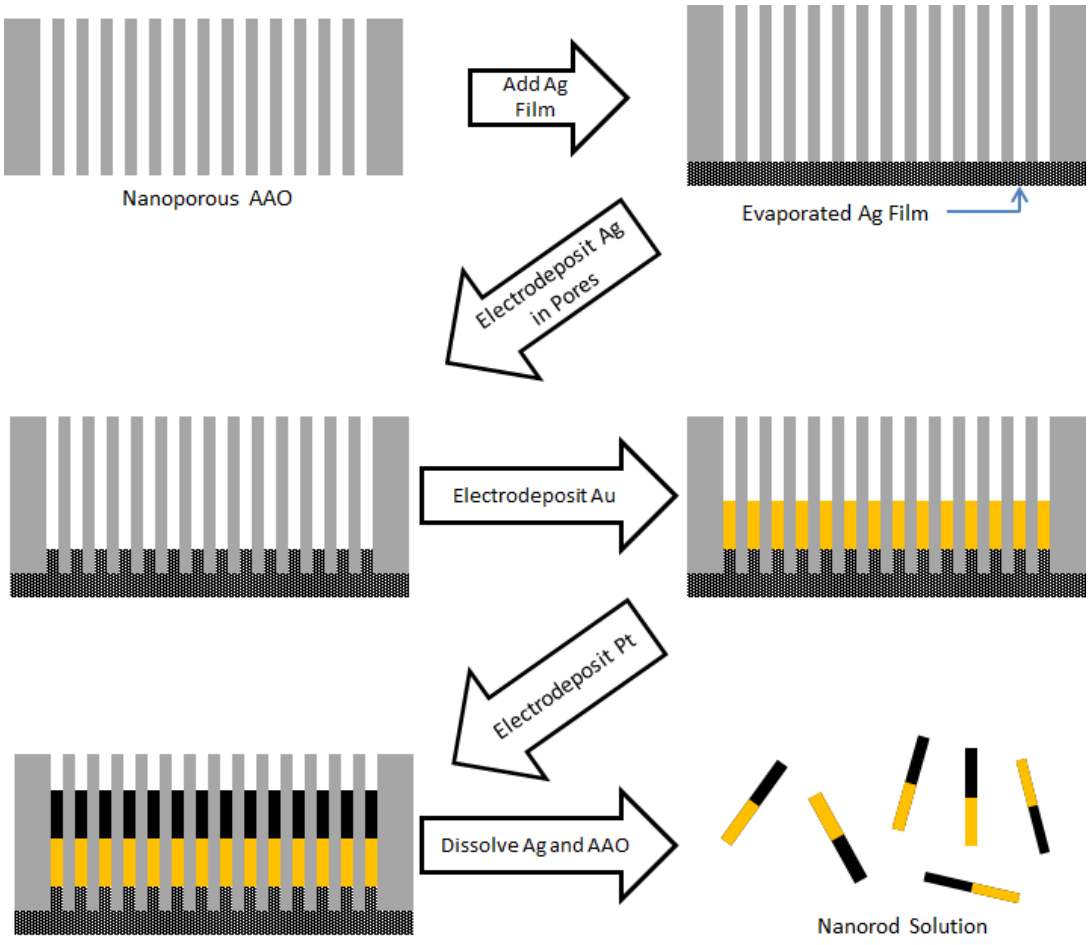

Figure 2.1 Process of making segmented nanorods using templated electrodeposition in anodic aluminum oxide templates

Another benefit of using templated electrodeposition is that the width of the nanorods can be chosen by using a template with the appropriate pore diameter, and the length of the nanorods can easily be tuned by controlling the amount of charge passed and thus metal deposited. Additionally, the interface is easy to make by changing the template to a different metal precursor bath, and any number of interfaces can be introduced by repeating this process. A simple metal-metal interface can be made by completely changing from one metal precursor bath to another, and more complicated interfaces such as a metal-alloy interface can also be synthesized by switching to a new bath with a mixture of metal precursors. The rods need to be made such that they are significantly longer than the spatial resolution of the sub-diffraction fluorescence microscopy method and so that they are narrow enough to fit within the penetration depth of the total internal reflectance excitation beam. With these constraints, I aimed to synthesize Au/Pt rods with segment lengths of several hundred nanometers and with a diameter of less than 100 nanometers.

2.3.2 Anodic Aluminum Oxide Template

One of the advantages in using AAO templates is that they are already commercially available as their nanoporous structure is used in filtering applications. These AAOs nominally come in various sizes which allows for the nanorod diameter selection as the deposited metal is confined to the space within the pores. However, in reality the nominal pore sizes and the actual pore sizes do not agree. This stems from their application in filtration in which the pore diameter at the narrowest point is cited compared to the diameter for the majority of the length of the pore. As the AAO is grown, a barrier layer of alumina remains present at the bottom of the pores as shown

in Figure 2.2.

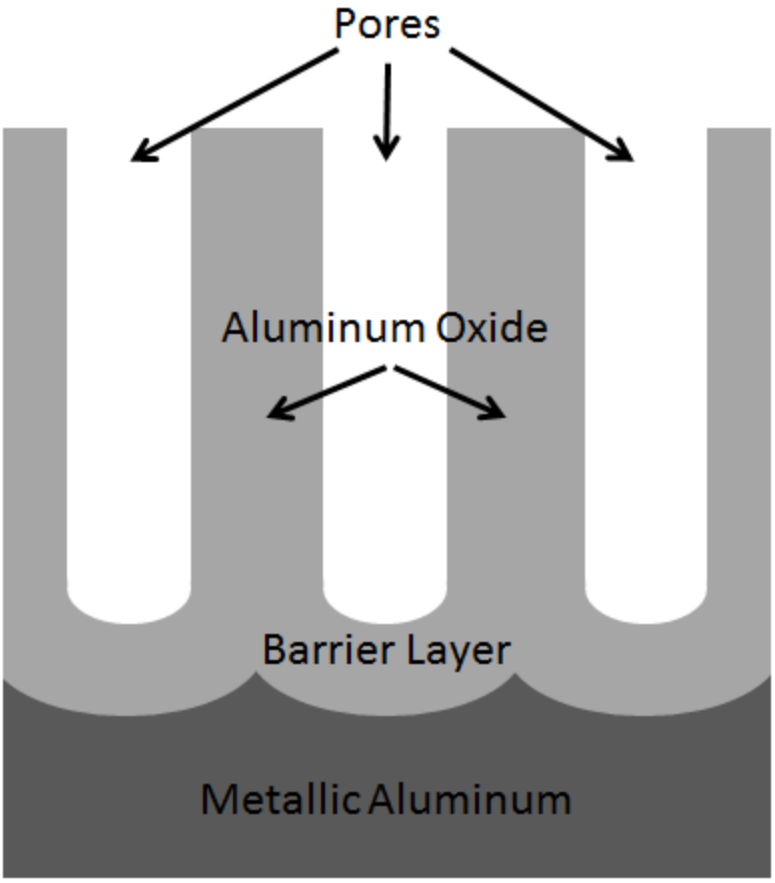

Figure 2.2 Schematic of cross sectional pore structure during AAO growth

After the template is grown to its desired thickness the barrier layer can be modified by further electrochemical treatment or chemical etching to penetrate the barrier layer and allow the pores to be continuous from one face to the other. These barrier layer modifications can yield smaller openings through the barrier layer than the size of the major pores. The pathway from the major pore through the barrier layer is highly branched. Figure 2.3A-C shows the top down SEM images of 200, 100, and 20 nm commercial AAO templates from Wattman respectively. As can be seen, the

major pore sizes do not all match with their nominal values. For the sample with nominal pore size of 20 nm, the top down image (C) shows the pores are much larger with a mean diameter of 165 nm. However the bottom up image (D) shows the side with the etched barrier layer, which has smaller openings averaging on 28 nm, which is much closer to the reported value.

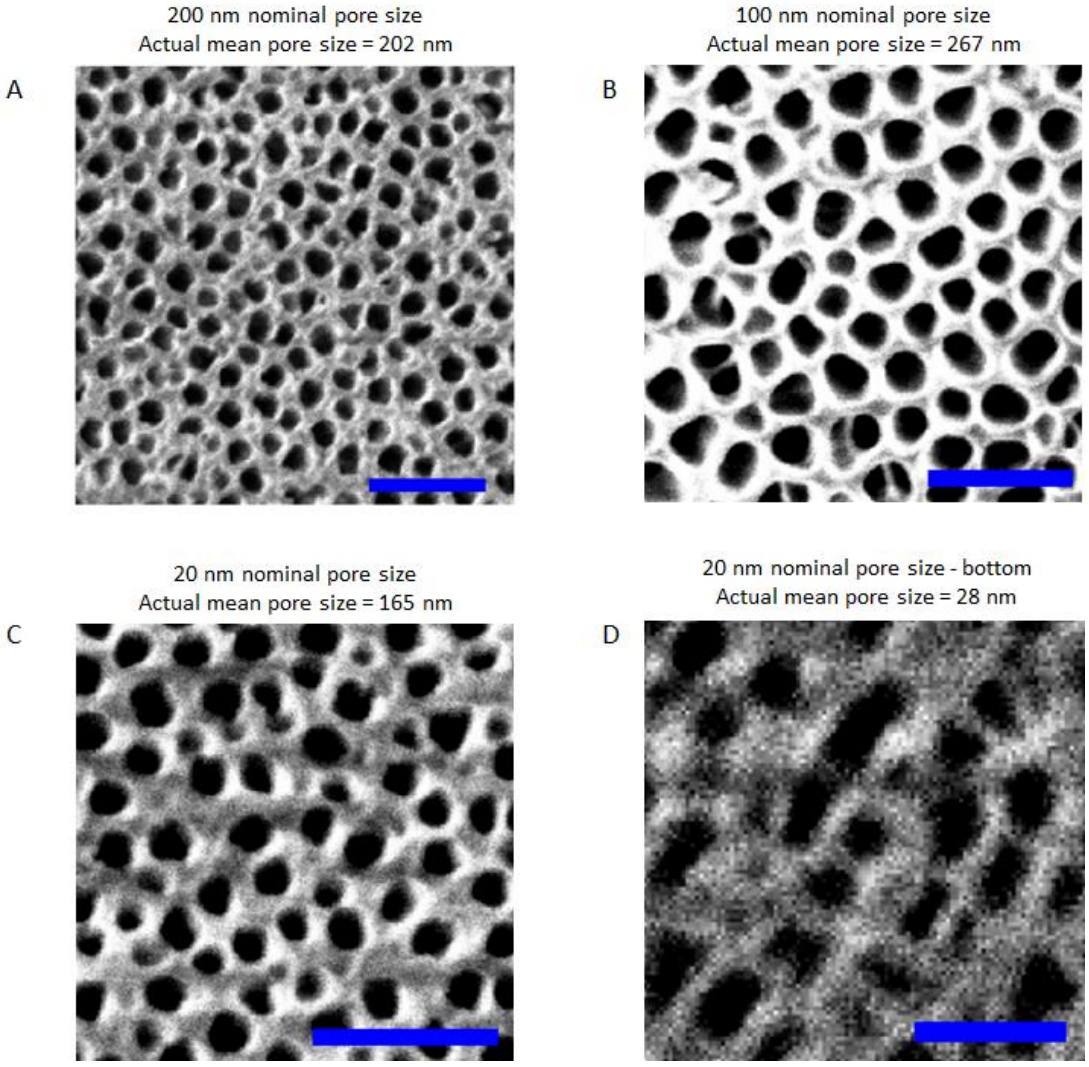

Figure 2.3 SEM images of commercial AAO templates with nominal pore sizes of 200 nm (A), 100 nm (B), 20 nm (C), and bottom face of 20 nm (D). Scale bars are 1 µm in A-C and 100 nm in D.

2.3.3 Electrodeposition of Au Rods into 20 nm Commercial AAO Templates

Following the synthetic scheme described in Figure 2.1, 20 nm Anodisc 25 membranes from Whatman were used as the template. Silver evaporation was performed on a CVC SC 4500 electron beam evaporator at the Cornell CNF facility. Silver was evaporated at a rate of 1.7 to 2.8 Angstroms/sec with a slower rate (~0.1 Angstrom/sec) for the first 30 nm to ensure good, uniform film quality at the interface that becomes the working electrode. Also the AAOs are mounted at a 45 degree angle to the direction of evaporation to ensure that only the back face and not the pore walls get covered with silver. Next, silver print was used to adhere the silver backing to copper tape. Then the template was laid flat against a glass slide and rubber cement was used to cover the copper tape and the edges of the template. This ensured that neither the copper tape nor the back of the silver film would come in contact with the solution, and that current could only be passed to the electrode at the bottom of the pores.

After the template/electrode assembly is prepared, silver is deposited into the bottom of the pores to fill in the barrier layer and part of the major pore so that the rods of the desired metal are deposited in the smooth portion of the pore. For this step 10 mM silver nitrate was used as the precursor solution. A two-electrode setup was used in which the silver film was the working electrode and a Pt wire was the counter electrode. A Ag/AgCl reference electrode was not used in this setup since the reference electrode frit allows chloride to escape into the bulk solution where it precipitates as AgCl and consumes the Ag^+ ions in solution. Ag was deposited by applying a -1.0 V bias on the working electrode using a CHI 1200 electrochemical

analyzer. One of the problems with using silver nitrate as the precursor solution is that the silver deposits resulting from it are known to cause dendritic tree-like deposits.[18] As can be seen in Figure 2.4, once the deposited silver structure reaches the surface of the template, it branches out and does not form a uniform film. Further, the silver structures are not coming out of all of the pores either, which means that once one silver branch reaches the surface, the Ag^+ ions in that vicinity will deposit on the surface structure and will not make it into the nearby pores. Silver cyanide is known to create smooth deposits of up to 50 micrometers when used as the precursor solution for electrodeposition but was not pursued for safety reasons.[18] Because of this challenge, the initial silver deposition step was skipped.

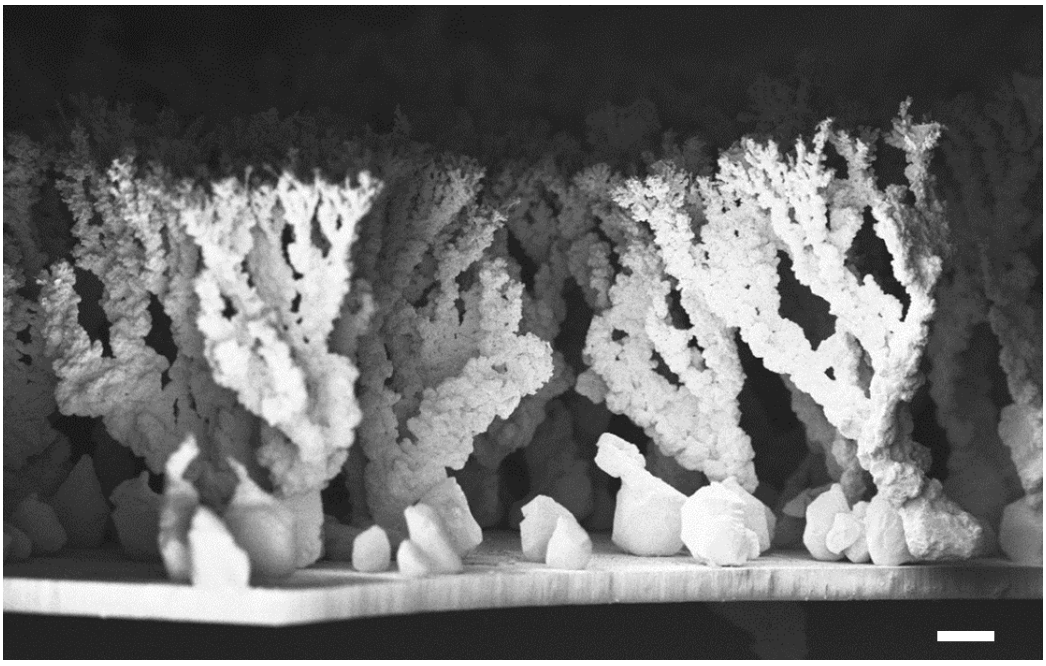

Figure 2.4 SEM image showing silver dendrites growing out of AAO pore structure. The scale bar is 100 μm.

As a trial before making Au/Pt nanorods, one-segment, Au only nanorods were formed in a variety of conditions in "20 nm" commercial templates. On my first several attempts, I performed a small, additional silver deposition for 5 minutes, by applying a -1.0 V bias on the working electrode in 10 mM $AgNO_3$ solution, which resulted in 1 C of charge being passed. From Wang et al, this amount should have deposited ~667 nm of silver into the pores.[16] Initially I was aiming to fill up the pores to 10 μm, which is still much less than the total height of the template, but often the silver deposits would reach the top surface in some locations as seen above. Next Au was deposited from a 10 mM $HAuCl_4$ and 0.5 M phosphoric acid solution, by passing 8 C of charge at -1.0 V bias in 50 minutes. Since the $HAuCl_4$ can be deposited by galvanic replacement with the silver, it is important that the voltage is already applied to the electrodes before the addition of the $HAuCl_4$ so that the Au grows on top of the silver and does not replace it. After completion of the deposition, the template and the silver film were dissolved. The resulting rods formed do not occupy the full diameter of the pore as can be seen in Figure 2.5. The supporting electrolyte plays a role in the deposition process and can control the morphology of the deposits, so other conditions were attempted.

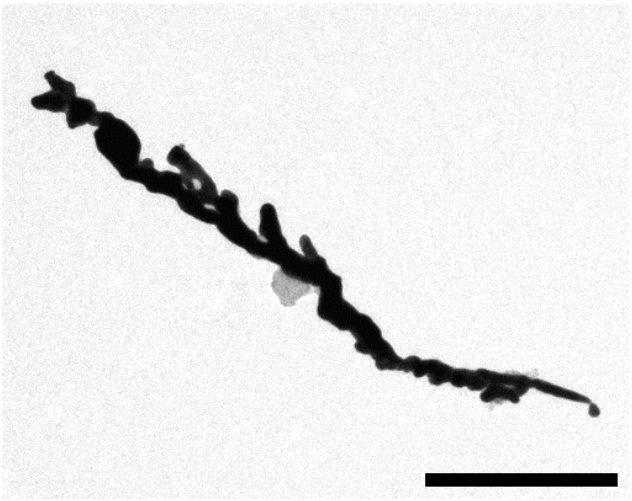

Figure 2.5 TEM image of a Au nanorod resulting from electrodeposition in the presence of phosphoric acid. The scale bar is 1 μm.

A new set of conditions were attempted in which the bath contained 0.5 M sodium thiosulfate, 0.5 M sodium sulfate, and 20 mM $HAuCl_4$. In this and subsequent attempts, the silver deposition step was skipped for the reasons explained above. A three electrode setup was used and the working electrode was held at -0.3 V vs Ag/AgCl which is 0.5 V more negative of where the gold reduction onset occurs. 1.12 C total charge was passed in 24 minutes. After the deposition, the template was removed by dissolution in base, but the Ag film was kept so that the rods on the film could be imaged as seen in Figure 2.6A. Since there was no sacrificial silver deposited into the bottom of the pores, the Au filled in the highly branched structure through the barrier layer resulting in a broom-like structure at the end to the silver electrode side. Even though in these conditions the gold deposited goes across the full width of the pore, the structure is still polycrystalline, consisting of many domains of about 15-20 nm each (Figure 2.6C). Another set of conditions was used, which yields

similar results; the bath consisted of only 10 mM $HAuCl_4$ without any supporting electrolyte. Instead of using a reference electrode a straight bias of -1.5 V was applied to the silver electrode. H^+ reduction did not onset until -1.6 V. 1.2 C was passed in 25 minutes. The resulting rods are shown in Figure 2.6.

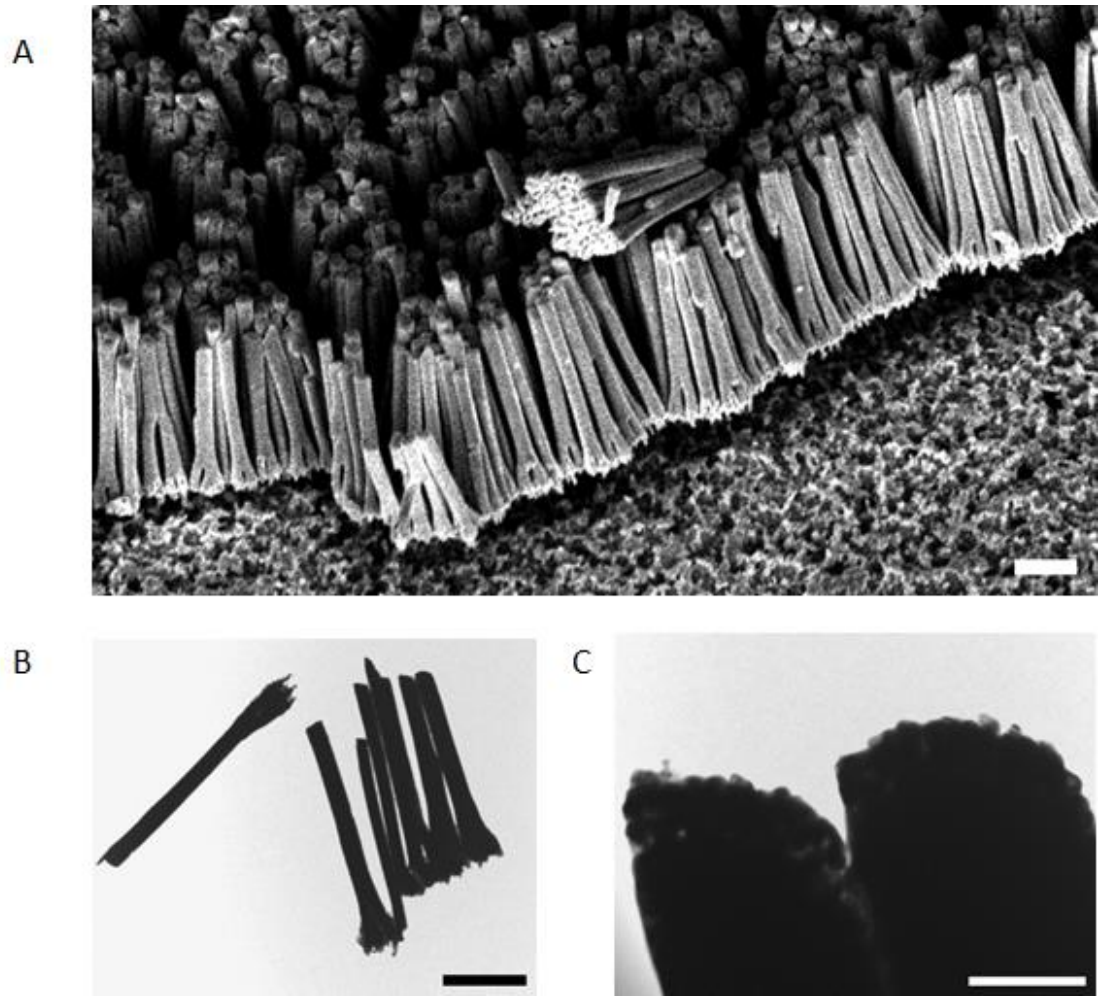

Figure 2.6 (A) SEM image of Au nanorods formed by electrodeposition after removal of the template only. (B) TEM image of the Au nanorods after removal of silver electrode. (C) Close-up of rod tips in B showing polycrystalline nature of the electrodeposits. Scale bars are 1 μm in A & B, and 100 nm in C.

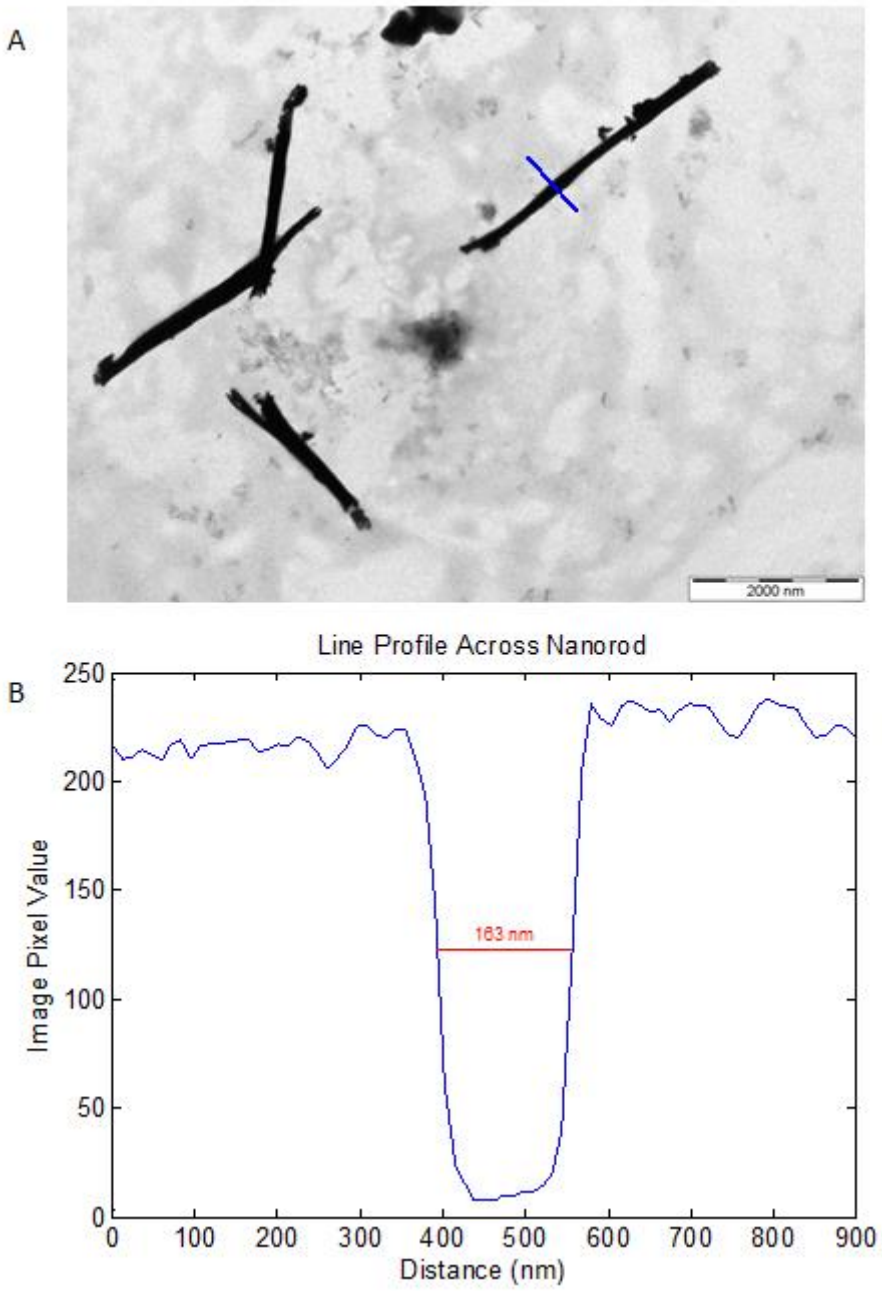

Figure 2.7 (A) TEM bright field micrograph of electrodeposited Au rods in 20 nm commercial AAO template without supporting electrolyte. (B) Line profile across blue line in (A).

By using different conditions to electrodeposit Au into 20 nm commercial templates, I find that using phosphate as a supporting electrolyte leads to incomplete

filling of the pores, producing seaweed-like structures, while using a mixture of sodium sulfate and sodium thiosulfate or no supporting electrolyte at all leads to complete filling of the pores with polycrystalline Au. Additionally there does not seem to be a difference in rod structure between using a two or three-electrode setup. Both are able to hold the silver film at a potential appropriate for reducing Au ions, and both lead to currents of a couple mA/cm^2. However, one problem remains in that the rods resulting from the "20 nm" commercial templates are ~165 nm in diameter which is in agreement with the size of the pores for the majority of the template (Figure 2.7 & Figure 2.3 (C) respectively). This diameter could be problematic when the rods are used as catalysts in the single-molecule fluorescence microscopy measurements because the fluorescence excitation comes from a TIR scheme where the light intensity exponentially decays from the interface with a length scale of a few hundred nanometers. This would lead to great inhomogeneity between the light intensity at the top and bottom of the rod as it lies flat across the slide. To avoid this, I would like to have rods with a diameter of less than 100 nm, which involves using a template with smaller major pores. Homemade AAO templates can be synthesized with pore sizes from 5 to 200 nm by using the appropriate conditions.[12]

2.4 Procedure and Theory for Homemade AAO Templates

AAO templates can be made by electrochemically oxidizing a high purity aluminum sheet in an appropriate electrolyte solution. By using a sheet of Al as the anode in an electrochemical cell, an oxide layer is grown by the following reaction while hydrogen is evolved at the cathode.[11,19]

$$2\ Al_{(S)} + 3\ H_2O_{(l)} \rightarrow Al_2O_{3(s)} + 3\ H_{2(g)}$$

This process is shown in Figure 2.8.

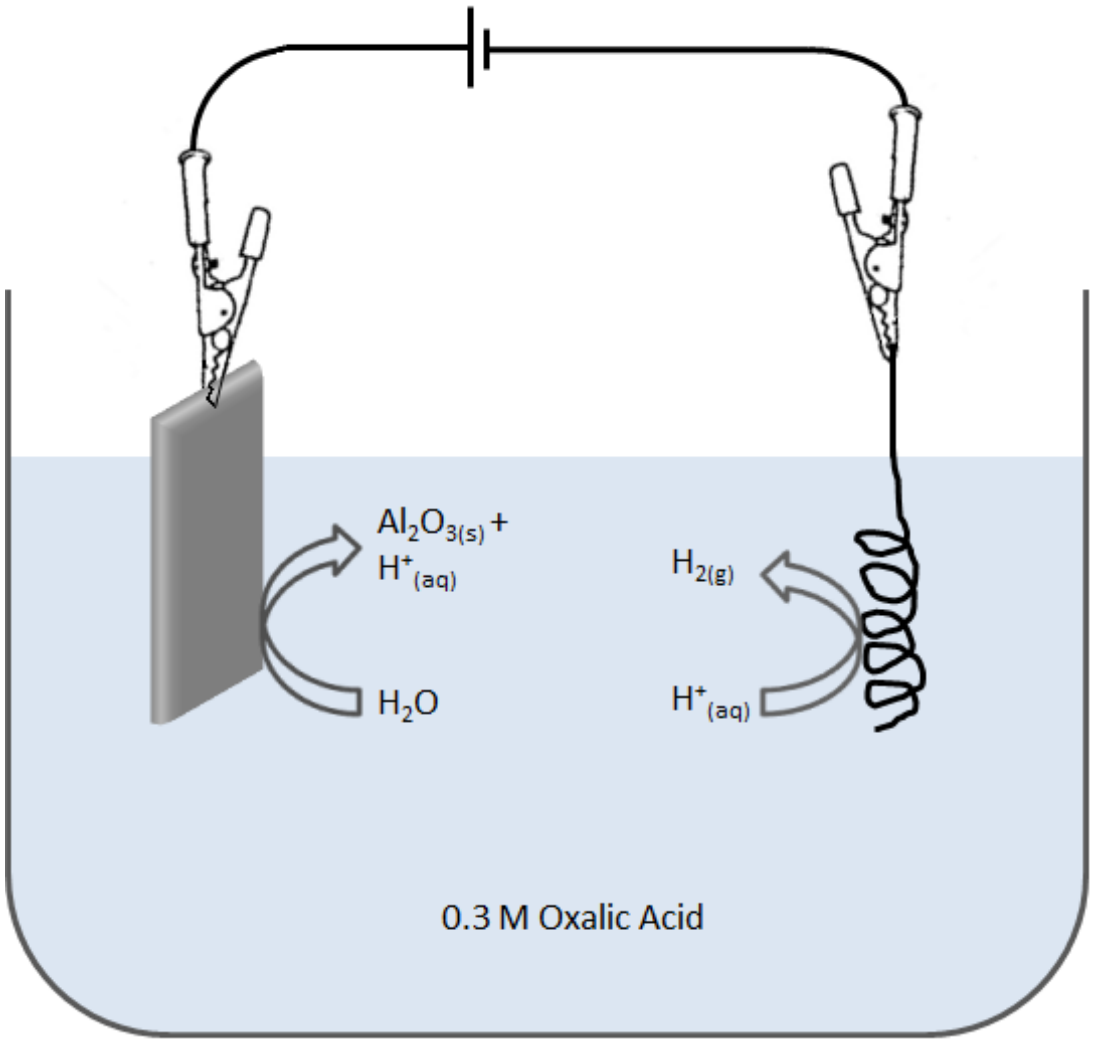

Figure 2.8 Diagram of chemical processes during AAO formation. The Al sheet is the anode on the left and the Pt coil is the cathode on the right.

The characteristics of the oxide structure are dependent upon the voltage applied, the temperature, the electrolyte solution used, and the time the process is run. In an electrolyte where the alumina is inert, an oxide layer starts to grow on the aluminum surface as a voltage is applied. As it grows it provides a barrier to further growth, thus decreasing the amount of current being passed until no further oxide can

be produced. This final oxide barrier layer thickness is dependent on the voltage applied. By changing the electrolyte solution, a competing process of oxide layer dissolution can be introduced. In the extreme case where the oxide layer is dissolved quickly compared to the rate at which it is electrochemically formed, no oxide layer build-up is maintained. These conditions are also used for electropolishing to produce a clean metal surface. By using an appropriate electrolyte solution, voltage, and temperature combination, the rate of oxide layer dissolution can be slow and comparable to the rate of electrochemical oxide layer formation. These are the conditions that lead to the formation of the porous oxide structure. There are many theories as to how the pore formation process actually occurs. However the reason for the hexagonal pattern is known to be due to the volume expansion of the oxide film relative to the underlying substrate. Experimental results show that after the barrier layer oxide is grown and the pore process has been initiated, the barrier layer thickness remains constant for the remainder of the process. This means that steady-state kinetics are achieved in which the rate of oxide formation and dissolution in the pore are equal. It is known that an electric field can play a role in the oxide dissolution process, and the enhanced electric field at the bottom of the pore could be responsible for the oxide layer's selective dissolution there. Regardless of the theory used to describe pore formation, the voltage applied affects the barrier layer thickness, the cell size, and the pore diameter. The temperature controls the current density (rate of oxide formation) and dissolution rate, and the electrolyte ions affect the oxide morphology and also the dissolution rate. Finally, the anodization time affects the oxide structure thickness. [11,19-21]

2.5 Experimental Conditions and Results for Homemade AAO Templates

Aluminum and Electrolyte Preparation

1 mm x 15 cm x 30 cm, 99.999% high-purity aluminum sheet was purchased from Laurand Associates. It was cut into strips approximately 30 mm wide by 75 mm long using aviation shears, which distorted the edges. The strips were then pressed flat using a 2-ton hydraulic press. A fresh Al surface was prepared by electopolishing the Al strips individually in a 4:1 ethanol to perchloric acid solution at 4 ^{o}C, using a Pt wire coil as the counter electrode and applying a +40 V bias while stirring the solution for several seconds. During this process bubbles are evolved at the Pt electrode and the surface oxide layer on the aluminum can be seen peeling away and leaving behind a shiny, polished surface. This process passes two amps of current and will cause the solution to warm up quickly if left going for too long. The Al was mounted in the solution so that only the alligator clip contact was above the solution, ensuring that most of the surface was cleaned. Next, the Al strip was rinsed with 18.2 MΩ water.

For the electrolyte solution, 2 liters of 0.3 M oxalic acid was prepared using 99.9% pure oxalic acid dihydrate from J.T. Baker and 18.2 MΩ water. The reason such a large batch was produced is that during the aluminum anodization some of the Al is released to the solution as $Al^{+}_{(aq)}$, which causes the electrolyte solution to change. By working with a large, 2-liter solution, the $Al^{+}_{(aq)}$ is diluted so that its concentration stays low for the whole anodization process.

Anodization Setup and Experimental Conditions

The anodization was performed in an apparatus set up similar to that in Figure 2.8. A 4 liter beaker was filled with the 2 liters of the oxalic acid electrolyte solution and placed in a tub that was connected to a circulating water bath. This tub and the

beaker were placed on top of a stir plate and a magnetic stir bar was used to gently stir the electrolyte. The water bath was set to 10 ^{o}C and left to equilibrate. 4 alligator clips were held together in a plane by connecting them with copper wire. 4 Al sheets were connected to this device and then held hanging in the electrolyte solution by a ring stand and clamp. The positive lead on an HP 6255A DC power supply was connected to the wire holding together all 4 alligator clips, so that all of the Al strips could be anodized simultaneously. A Pt wire coil was also held in place with a clamp and connected to the negative lead on the power supply. The power supply was set to 40 V and turned on to start the anodization. At first a large current of over an amp was present as the barrier layer formed on the fresh Al surface. Within 10 – 20 seconds the current quickly decays to its stead-state value around 4 mA/cm^2. The first anodization was run for about an hour. After that the Al pieces were removed and placed in a bath containing a few weight percent chromium oxide in 85% phosphoric acid at 70 ^{o}C for an hour to selectively dissolve the oxide layer. The first oxide film is grown off of a flat Al surface, but as the pore structure develops, the metal/oxide interface takes on a repeating cellular structure with a honeycomb pattern. This first oxide growth and removal serves to prepatterns the metal surface which allows the next oxide layer to have better defined pore. This is shown in the top down SEM images of the oxides resulting from the first and fourth anodizations in Figure 2.9B and C respectively. After removal of the first oxide film, the remaining anodizations were run overnight so that the resulting oxide layer would be over 100 μm thick. This made them easier to handle as they would not break easily like the samples that were only anodized for a few hours.

Anodic Aluminum Oxide Removal

After the second anodization had run overnight, the oxide film needs to be separated from the underlying metal. The Al strips with the oxide still attached were removed from the oxalic acid bath and rinsed with 18.2 MΩ water. One Al strip was then suspended to the same level in a 50 mM hydrochloric acid solution and connected to the negative lead of the power supply. A stir plate and magnetic bar were used to stir the solution. A Pt wire coil was also suspended in the solution and connected to the positive lead of the power supply. The power supply was set to 10 V and turned on. A current of around 4-20 mA/cm2 results, and oxygen and chlorine bubbles are formed at the Pt anode. The oxide is permeable to ions, and H^+ is reduced to $H_{2(g)}$ at the metal-oxide interface. This creates a bubble of hydrogen that propagates along the interface until the oxide layer delaminates from the metallic substrate. Sometimes, the voltage needed to be increased to get this to happen. Usually the entire face will come off in once piece, with the breaks occurring at the corners. Once this happens, the solution can now reach the aluminum metal unencumbered and the current saturates the power supply at which point it is turned off. The Al strip with the oxide loosely hanging on was removed from the solution and rinsed with 18.2 MΩ water again. It is then dried in an oven at 120 ^{o}C. The oxide then easily popped off the metal either by hand or with gentle leverage applied by razor blade. Since the Al strip has two large faces, sometimes one face would pop off before the bubble fully formed under the oxide on the other side. This is the case that would require a little help from a razor blade to remove. At this point the oxide was fully independent and was marked to indicate which side is up. A brief chemical etching step was employed to slightly widen the pores and make them more uniform. The AAOs were placed in a 5% phosphoric acid solution at 45 ^{o}C, briefly sonicated to help wet the pores, and left to

sit for 10 minutes. Then they were removed, rinsed with 18.2 MΩ water, and dried. SEM imaging was performed on the oxide at this point and the side-on, top-down, and bottom up images are depicted in Figure 2.10A, B, and C respectively. The Al strips were then placed in the same chromium oxide and phosphoric acid bath mentioned above to remove any last fragments of oxide still bound to the metal. Once the metal is free of oxide, it was removed, rinsed with with 18.2 MΩ water, and reanodized in the oxalic acid bath. This process can be repeated until the Al strip becomes too thin and weak for further use. The 1 mm thick Al sheet used as the starting material can produce 4-6 good oxide layers.

I invented the process of removing the oxide layer from the metal using cathodic hydrogen evolution so that the metal can be reused; usually the Al layer is either amalgamated or selectively dissolved leaving behind only the oxide layer.[19,22,23] Using the cathodic hydrogen evolution reaction to remove the oxide layer is beneficial because many oxide films can be grown and recovered from a single sheet of aluminum. Additionally, by successively anodizing the same sheet, the initial anodization that gets discarded only needs to be performed once to provide a few useful oxide films. Figure 2.9A shows how the pore diameters from resulting oxide films change with successive anodizations. The initial oxide has smaller, ill-defined pores, but after this layer is discarded, the remaining oxides have well defined pores and near-constant pore diameters.

For some of the samples produced, the pore-widening step was omitted. The pore diameter distribution in Figure 2.9A for the second anodization is 40 +/- 5 nm. For a different oxide film produced in the same conditions but that was subjected to the pore-widening process described above, the pore diameter distribution becomes 53

+/- 4 nm, which is shown in Figure 2.10B.

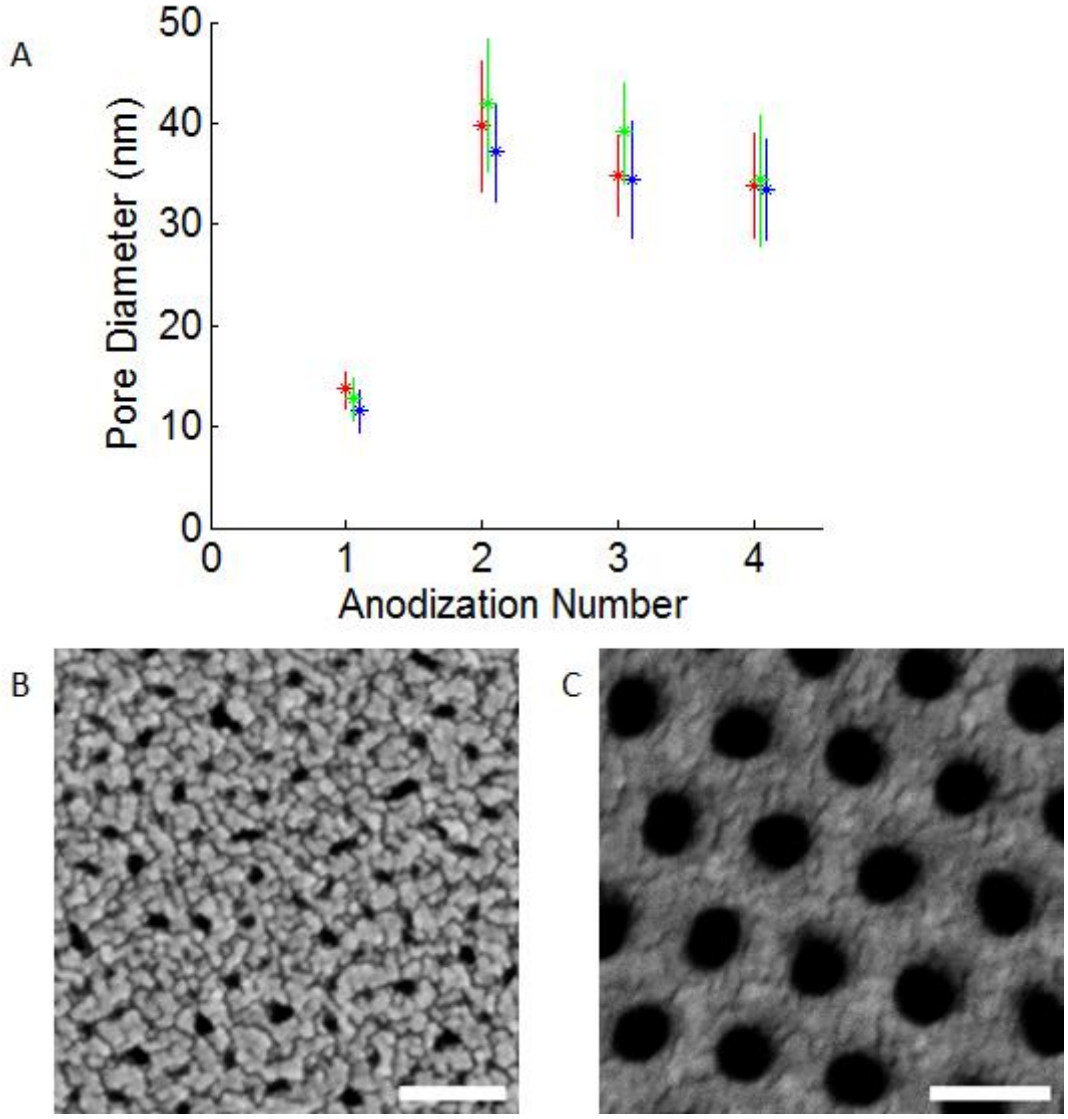

Figure 2.9 Pore diameter versus anodization iteration (A). The red, green, and blue markers represent three independent trials of different sheets of aluminum. Anodizations were performed at 4 ^{o}C in 0.3 M oxalic acid. SEM top down image of pores after first anodization (B), and fourth anodization (C). Scale bars are both 100 nm.

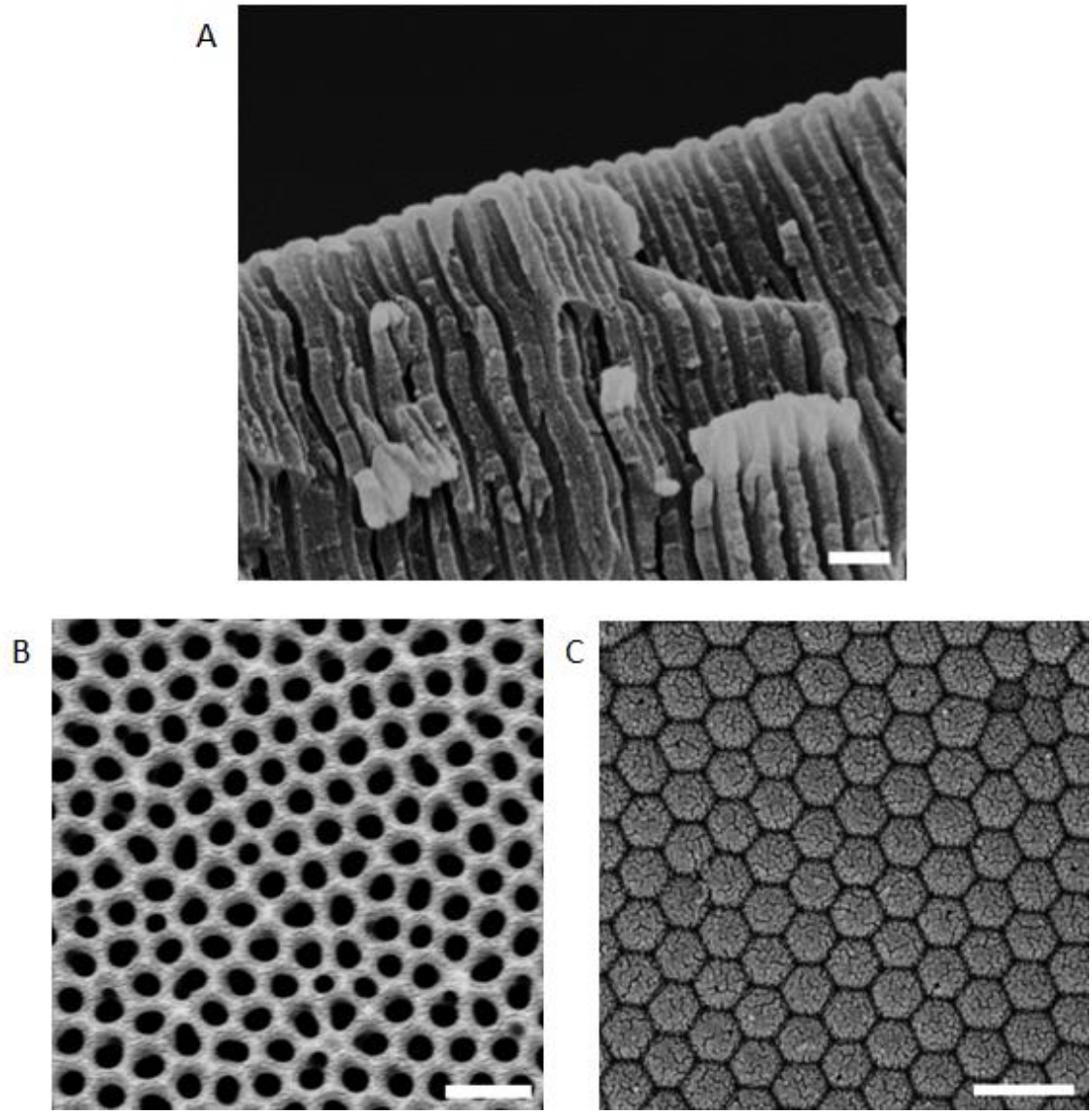

Figure 2.10 SEM images of pore structure of AAO film from the side on (A), top down (B), and bottom up (C) views. All scale bars are 200 nm.

Barrier-layer Thinning and Through-barrier Electrodeposition Theory

After the homemade templates have been synthesized, removed from the metallic substrate, and possibly pore-widened, they still have the barrier layer present at the bottom. This is a challenge because the pores are only open on one side making

it impossible for the silver electrode and solution to come into contact. It is possible to reduce the thickness of the barrier layer at the end of the anodization by tapering the voltage down. Since the barrier layer thickness is dependent on voltage, this has the effect of reducing the barrier layer thickness. Since the voltage also controls the pore spacing, pore branching also accompanies this process. Choi has shown that by tapering the voltage down to 0.01 V, the barrier layer becomes thin enough that silver ions can be deposited through the barrier with a 2.5 V applied potential since this is significantly larger than the breakdown potential of the barrier layer.[24] Similarly, Gerein showed that AC deposition could successfully be used on AAO templates still containing a barrier layer to electrodeposit copper in the pores through the barrier layer after thinning to only 10 V. The reason as to why the AC deposition works whereas the DC fails is that the barrier layer has a large resistance to DC current but for AC current it conducts preferentially in the cathodic direction. However, the AC deposition method only yielded rods in a relatively small fraction of the total pores.[21] These studies show that the barrier layer challenge is still surmountable.

Barrier-layer Thinning and Through-barrier Au Electrodeposition

A piece of Al that had already been anodized twice at 40 V was used to make another oxide film. After 19 hours of oxide growth the voltage was tapered from 40 to 0, linearly in small increments over 6 minutes to decrease the thickness of the barrier layer. Then the pore widening procedure was performed for 20 minutes to help further reduce the barrier layer thickness. At this point the Al piece with the oxide layer still attached was placed in the $HAuCl_4$ solution for gold deposition. The Al was the

cathode and the Pt coil was the anode. The bias was slowly ramped up to 10 V at which point some current (around 1 mA/cm^2) started to pass, and within 15 minutes the purple color of the gold could be seen in the oxide film. An SEM image of the bottom up view of a removed piece of oxide template after voltage taper is shown in Figure 2.11A, and a close up TEM image of the resulting Au rod is shown in Figure 2.11B. The effects of the voltage tapering on the barrier layer can be seen by comparing Figure 2.10C, which shows what the barrier layer looks like in the absence of a voltage taper, with Figure 2.11A. Although the bottom up view of the voltage tapered barrier layer looks porous, these pores are not continuous with the major pore grown before the voltage taper. The presence of a barrier layer between the top and bottom pore is demonstrated since a relatively large bias needed to be applied before any current could pass which would not be the case for continuous pores. This through barrier layer deposition method was also tried on another sample from the same batch that only had 10 minutes of pore widening. For this sample, the AAO popped off of the metal, which is I how I discovered the oxide removal technique mentioned earlier. This method works but is very sensitive to the applied voltage; if the voltage is too low, no deposition occurs, but as a higher voltage is applied, the risk of forming a bubble between the metal and oxide layer increases which will separate the porous structure from the circuit. This method was not used further because of this challenge.

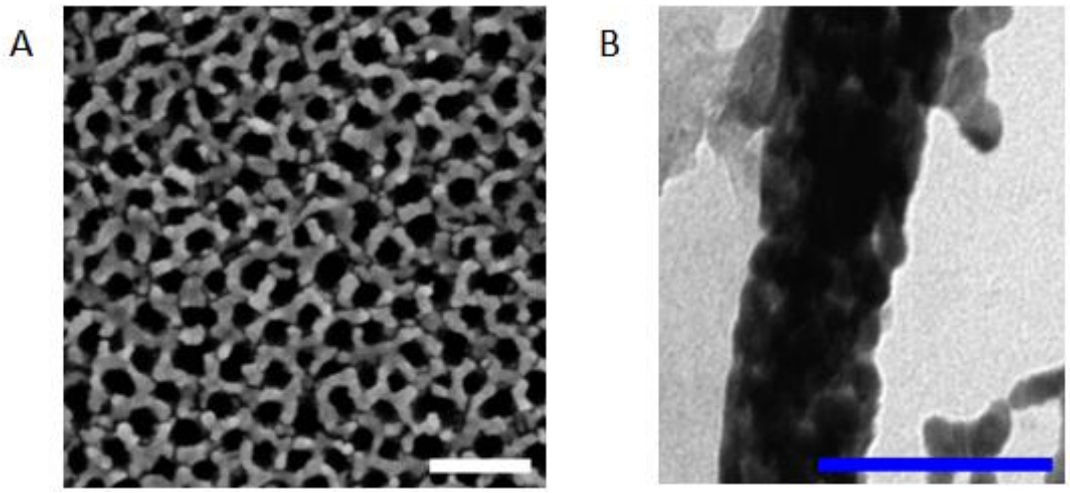

Figure 2.11 Bottom up SEM image of voltage-tapered AAO (A). TEM image of a Au rod deposited in a 40 V anodized homemade AAO template, with 20 minutes of pore widening, without barrier layer removal (B). Both scale bars are 100 nm.

Barrier Layer Removal

In order to bypass the challenges of through-barrier deposition, the barrier layer needs to be removed. This is done by a chemical etching process in basic conditions. Since the etching process occurs quickly in aqueous solution, it is difficult to stop the process after only the barrier layer has been removed without also dissolving some of the template as well. Using potassium hydroxide in ethylene glycol as the solution slows down the etching process since the potassium hydroxide has a lower solubility in ethylene glycol than water. Additionally, the increased viscosity of the ethylene glycol prevents the pores from wetting after the barrier layer has been removed which helps prevent the etching of the whole template. A saturated potassium hydroxide in ethylene glycol solution was prepared. When it is first mixed the solution is clear, but will darken over time. However, the age and color of the solution does not affect the rate at which it etches the alumina. Some of the solution

was poured into a watch glass, and then the alumina templates were placed on top of the meniscus with the barrier layer side facing down, making sure that there were not any air bubbles between the alumina and the solution. The pieces were left to etch and were removed after a set time, upon which they were rinsed with 18.2 MΩ water. Several pieces were used to construct a time series of the etching process which is shown in Figure 2.12. As can be seen, the barrier layer removal process does not occur uniformly within each unit cell. The etching continues until it breaks through in one spot, which occurs around 4 hrs and then the hole widens until the barrier layer is completely removed around 12 hrs 45 mins.

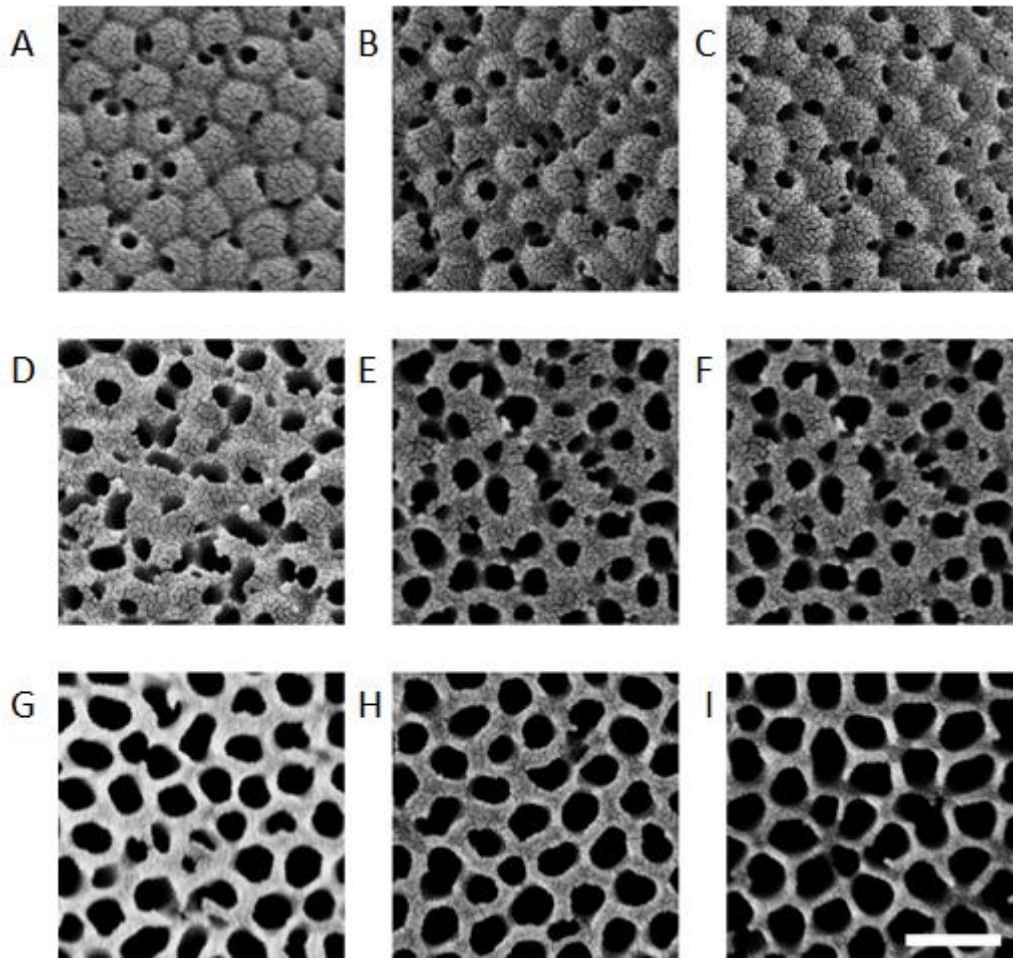

Figure 2.12 Bottom up SEM of barrier layer removal time series, after chemical etching in saturated KOH/ethylene glycol solution for 4 hrs 10 mins (A), 6 hrs (B), 7 hrs (C), 8 hrs (D), 9 hrs (E), 10 hrs (F), 12 hrs 45 mins (G), 15 hrs 35 mins (I). All images are shown in the same magnification. The scale bar is 200 nm.

After some time, the first saturated potassium hydroxide in ethylene glycol solution had been consumed, and a new batch was prepared using 17.5 g of KOH and 50 mL of ethylene glycol. Even though both solutions were saturated in that there was still solid KOH at the bottom of the solution, the etching rate for the new solution was faster. Using this solution, the barrier layer was completely removed in 90 mins as shown in Figure 2.13. This solution could be remade using the same conditions and achieve similar etching results.

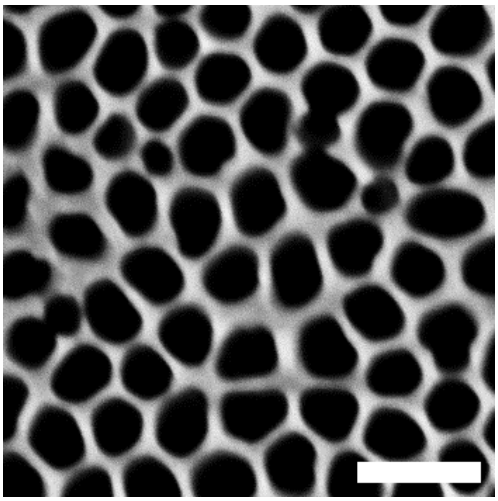

Figure 2.13 Bottom up SEM of barrier layer removal in solution containing 50 mL ethylene glycol and 17.5 g KOH after 90 mins. Scale bar is 100 nm.

Use of Homemade Nanoporous Alumina as a Template

Once the homemade nanoporous alumina films were made with sub 100 nm pores and had their barrier layer removed, they were ready to be used as templates. Silver was evaporated onto the top face as described before. Since the pore templates were around 100 μm long and the deposited rods were only a couple of μm long, the rods only formed near one end. The top face was chosen since the pores were more regularly aligned and more uniform in size at this face as compared to the bottom one. Also, sometimes the silver was evaporated onto the top face before barrier layer removal. This is not necessary but it helps to mark which side is the top. Another benefit of using the homemade templates is that the step in Figure 2.1 where Ag is electrodeposited into the template to fill up the bottom of the pore is not necessary since there is no branched portion present. This means Au and Pt can immediately be

deposited without forming the broom-like structures in Figure 2.6.

Electrodeposition of Pt

Pt was electrodeposited into the homemade templates with pore widths of around 80 nm using a three-electrode setup with Ag/AgCl as the reference electrode. The evaporated silver film was the working electrode and a Pt wire coil was the counter. The working electrode was held at -1 V and lowered into a solution of 50 mM HCl, 50 mM glycylglycine, and 5 mM H_2PtCl_6. This was done to prevent galvanic replacement of the Ag by the Pt ions. After 0.1 C had passed in 160 secs, some Pt had deposited into the pores, covering the underlying Ag, and the system was returned to open circuit. After waiting a minute for the system to equilibrate, the open circuit voltage was measured at 0.36 V vs Ag/AgCl. 1.9 C of additional Pt were deposited at 0 V in 42 mins; the resulting Pt rods are shown in Figure 2.14. This potential was chosen since it was far enough negative of the OCV that Pt deposition should be diffusion limited but not any further to avoid introducing other reduction processes. In some cases a pulsed deposition was used in which the working electrode was held at OCV for 10 secs and then held 300 mV negative of OCV for 10 secs. The reason behind the pulsed deposition is that during the negative pulses, the concentration of Pt ions near the working electrode decreases as they are reduced, and the time held at OCV allows for this concentration gradient to dissipate before the next reduction step. The structure of the rods looks similar either with or without pulsing.

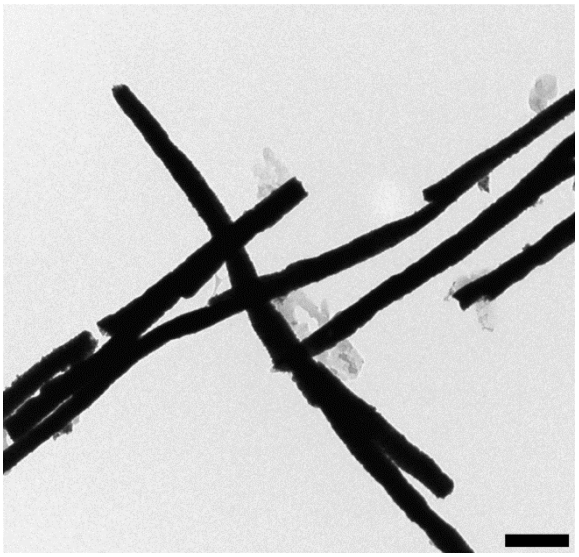

Figure 2.14 TEM image of Pt rods. Scale bar is 200 nm.

2.6 Challenges Remaining for Electrodeposited Nanorods

2.6.1 Making Bimetallic, Segmented Au/Pt Nanorods

With the experimental conditions for both Au and Pt deposition tested, the next step was to make bimetallic, segmented Au/Pt rods. A few of these samples have been produced by first depositing Au into the template and then rinsing the template thoroughly before placing in the bath for Pt deposition. Multiple rinses were performed between switching baths and sonication was used to aid in increasing diffusion into and out of the pores to ensure that all of the residual ions from the Au bath had been removed. Equal amounts of Au and Pt were deposited so the rods should be all Au on one half and all Pt on the other. A TEM image of these rods is shown in Figure 2.15. As can be seen in the image, the Z-contrast between the Au and Pt domains is not enough to differentiate the two segments from each other using

bright field TEM imaging, which is not surprising as their atomic numbers are merely one apart. STEM-EDX has also been used on this sample in an attempt to find the two domains within one rod, but the emission energies of Au and Pt are close, requiring long integration times in order to resolve the signal distributions from one another. Although the STEM-EDX was not able to measure 100% Au composition on one end and 100% Pt composition on the other, it was able to identify some of the fragments as either Au or Pt. This means it is possible that the rods can break at the interface yielding smaller particles that are dominantly one material. Additionally some rods were identified as having more Au than Pt on one end and more Pt than Au on the other. The preliminary results of this are promising, but more work is needed in order to identify each end segment and more importantly, the interface.

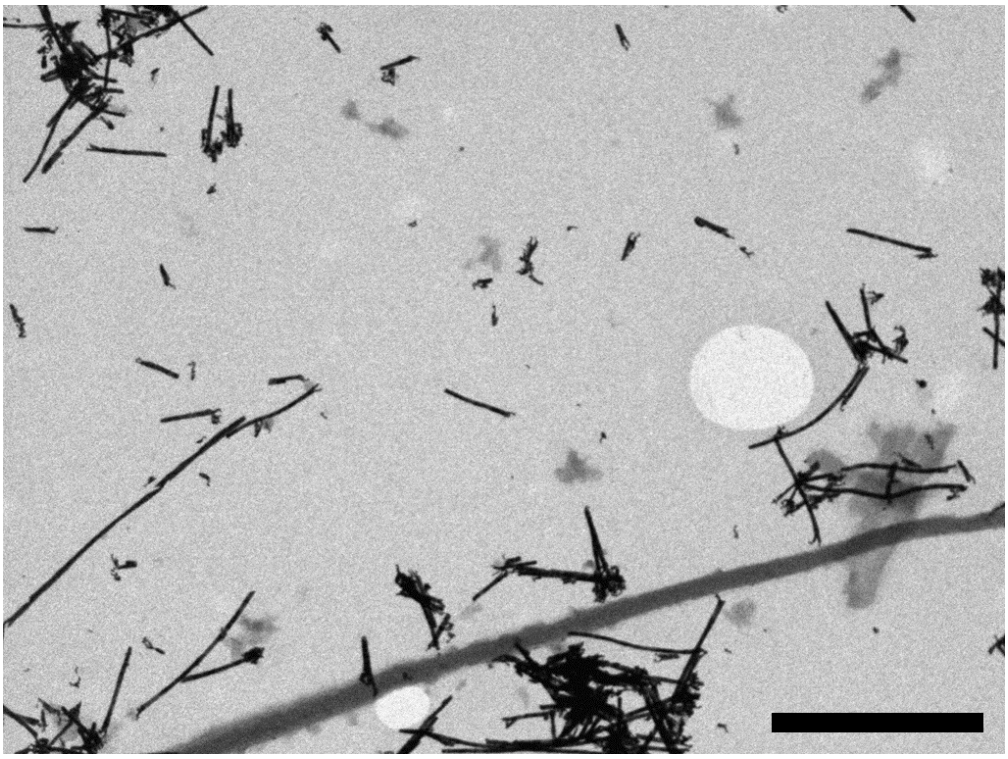

Figure 2.15 TEM image of electrodeposited nanorods using sequential electrodeposition of Au and Pt. The scale bar is 500 nm.

2.6.2 Single-molecule Catalysis Measurements of Au, Pt and AuPt Nanorods – Detection Issue

For the single domain Au or Pt rods, ensemble catalysis measurements confirmed their activity in catalyzing resazurin to resorufin. These samples were studied using single-particle, single-molecule catalysis measurements using fluorescence microscopy as described in the previous chapter. Despite being active at the ensemble level, no fluorescent signal resulting from catalysis was measured using the single-molecule technique on the microscope. This result is not completely unexpected. Plasmonic particles have the ability to quench the emission from excited

fluorophores close to their surface. This quenching behavior decays as the particle-fluorophore separation increases and depending on the system, the quenching behavior stops once the separation is increased to 20 to 40 nm.[25,26] This is one explanation as to why a fluorescence signal cannot be detected on the particle surface. Another possible reason is that the desorption time of resorufin from the particle surface is faster than the time resolution of the imaging system. Either way this is a challenge since a measurable fluorescence signal is required in order to spatially resolve the catalytic activity. The same problem occurred for the spherical gold nanoparticles 20 nm and larger. As was done before for those particles, a strategy to overcome this challenge is to add a mesoporous silica shell, which allows fluorescence detection of resorufin while adsorbed in the shell away from the particle surface.

2.6.3 Silica Shell Coating on Au and Pt Nanorods

The same procedure for adding a mesoporous silica shell onto the spherical Au particles was also used for the electrodeposited rods. The first step was surface functionalization of the particles' surface with dilute 3-mercaptopropyltrimethoxysilane (MPTMS). The sulfur group binds to the Au or Pt surface and the silane group on the other end serves as a nucleation point for further silica growth using first sodium silicate and then tetraethylorthosilane as precursors. At this stage a solid silica shell of ~100-150 nm thickness was present. The silica shell was etched in the presence of cetyltrimethylammonium bromide (CTAB), a surfactant, in order to direct the etching to form a porous structure. The growth of the solid silica shell is fairly robust and easy to reproduce. TEM images of electrodeposited Au rods with solid silica shells are shown in Figure 2.16A & B.

However, the etching step is highly sensitive to the starting shell thickness and the concentrations of particles, surfactant and hydroxide ion. Because of this sensitivity, it was necessary to synthesize several batches of particles with thick silica shell so that slightly different etching conditions could be performed on each batch. Another possibility was to take one batch of particles with a solid silica shell and divide it into many smaller aliquots, and perform variations of the etching on these. However, this was not possible since the amount of rods per batch was already fairly low. Dividing it into smaller aliquots would not yield a sufficient amount of material to work with in further steps. Since the amount of rods per batch is determined by the template size, a much larger template would be required in order to significantly increase rod yield. Use of a larger template could be pursued in the future, but ~6 cm^2 were the largest ones used thus far. After many trials a sample with a porous silica shell was obtained. A TEM image of AuPt rods with a porous silica shell is shown in Figure 2.16C. The lower transmission contrast in the image and the rough edges of the shell helps confirm the porous nature of the silica.

After the etching procedure is done, the sample is calcinated in a glazed ceramic dish in a two stage process. First the sample is left to dry in the dish under mild heating conditions. Then the sample is raised to 120 ^oC for 30 minutes, which enables the shell to cure and lock in its morphology. Then the temperature is raised to 500 ^oC for one hour to burn off any remaining organic ligands so that there is a continuous void path from the outside of the shell, through the pores, to the metal particle surface. At this point the core-shell particles are tested for catalytic activity at the ensemble level to confirm the continuous nature of the pores in the silica shell. At this point the sample can be dispersed onto a microscope slide for single-molecule

characterization. If the etching does not reach the core surface, or if the ensemble activity is tested before the etching has occurred, then there will not be any ensemble activity observed.

These etched and calcined core-shell particles were retested for catalytic activity using the fluorescence microscopy technique, but again, not enough fluorescence signal was detected. The characterization of the porous silica shell by TEM is insufficient to determine if the shell is porous enough or the pores have reached the surface of the metal. Further characterization on the porous shell could include nitrogen adsorption/desorption and/or X-ray diffraction. These techniques would give more information on the pore sizes and distribution. However, these techniques also require about 10 milligrams of sample as a minimum, and the scale of the templated electrodeposition used yields only a few milligrams of sample per batch.

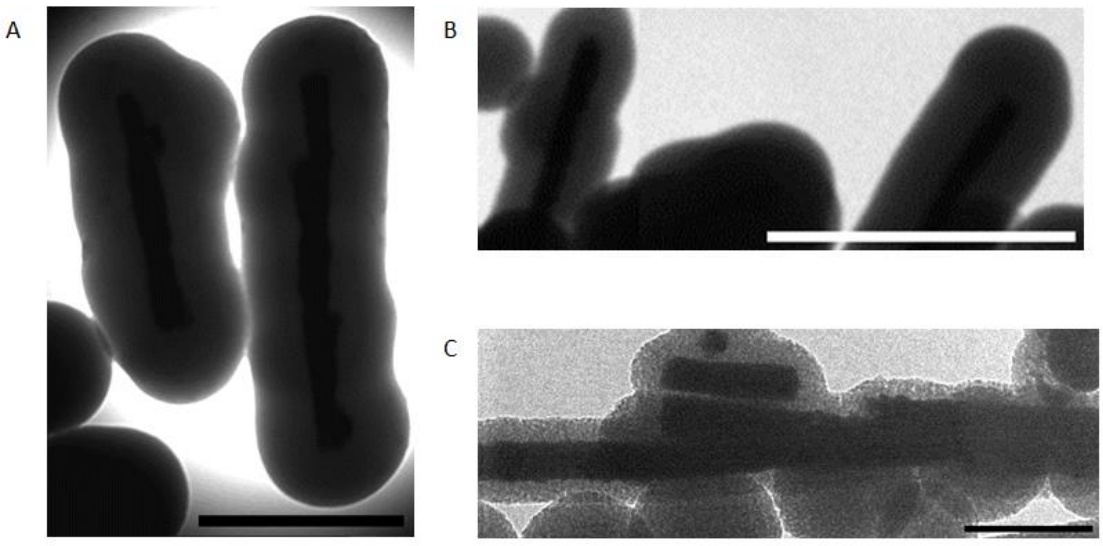

Figure 2.16 TEM images of Au rods with solid silica shell (A & B) and AuPt rods after etching to make mesoporous silica (C). Scale bars are 500 nm in A &B, but 200 nm in C.

2.6.4 Making Single Crystal Domains of Au and Pt

One of the challenges with the electrodeposition method is that the metallic deposits form in a polycrystalline manner, with domain sizes smaller than the resolution of the fluorescence sub-diffraction imaging technique. Experimentally, this should not be a problem as the polycrystalline rods are still catalytically active. However, the overall goal of the project is to get structure-activity correlations, specifically with the goal of comparing activity at the interface versus non-interface regions. Without a clearly defined interface, high resolution characterization would need to be performed, and ideally it would be performed at the single-particle level. Physical characterization on the same particles as used for the single-molecule measurements has only been demonstrated thus far at the SEM level, which is not capable of resolving a complex interface made of many small domains. To get around this problem, single crystalline particles can be used that will have a simpler interface, ideally epitaxial, that is easier to understand and does not require high resolution correlation at the single particle level.

The morphology of the metal deposits during electrodeposition is dependent upon the overpotential used, temperature, and any interacting additives in the bath used.[18] Tian et al, found that when a 2 wt % of gelatin was added to a commercial Au electroplating bath, that at high overpotentials (more than -1 V) a polycrystalline Au deposit forms, whereas when a lower overpotential is used (-0.7 V), the Au deposits are single crystalline.[27] I attempted to reproduce this result by adding 2 wt % gelatin to the Au bath I described previously, but the resulting rods were still polycrystalline.

Another strategy I attempted was to take the polycrystalline rods and anneal them so that the domains merge together. The first way I attempted to do this was by

electrodepositing Au into the AAO templates, then removing the bottom silver layer only so that the Au rods were still inside the AAO pores. Then I heated the template to anneal the Au inside. What I found is that at temperatures less than 300 ^{o}C, the Au morphology looks the same, and at higher temperatures, the alumina undergoes some transition and can no longer be dissolved in aqueous base, thus making extraction of the rods impossible. The other method I tried was to get the polycrystalline Au rods in solution, and grow a protective silica shell on them as described earlier. Then I annealed these rods for an hour at 500 ^{o}C, and removed the silica shell by heating to 90 ^{o}C in aqueous base. These rods are shown in Figure 2.17. As can be seen the domain sizes look larger compared to the unannealed Au rods in Figure 2.11B, but clearly a single crystal is not present. Additionally in this figure, it looks as if there could still be some shell material present that was not removed. Since harsh conditions were used to dissolve the silica all of it should be removed. It is possible that Au silicides could have formed between the Au and some Si-containing material. Young et al. showed that Au can form silicides with Si at temperatures as low as 200 ^{o}C.[28]

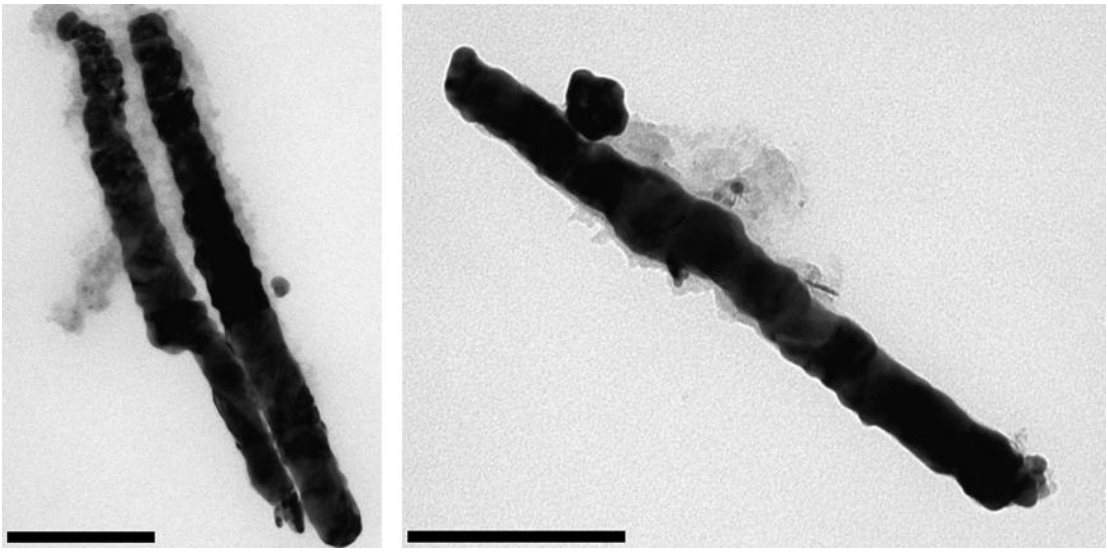

Figure 2. 17 TEM images of polycrystalline Au rods that were encapsulated in a silica shell and annealed at 500 ^{o}C before shell removal and imaging. Scale Bars are 200 nm.

A challenge still remains in that for the polycrystalline, bimetallic rods, some alloying could still occur as the voids between the domains collapse. However, it is known that for a pure Au-Pt interface some diffusion across the interface will occur at high enough temperatures. Bolk et al showed that this can happen at temperatures greater than 900 ^{o}C. By using his high temperature data and extrapolating down to 500 ^{o}C the effect of Au and Pt diffusion across the interface will be negligible.[29]

In the future, the fluorescence experiments could be attempted using a TEM grid as the particle support, thus allowing a higher degree of physical characterization to correlate to the catalysis results. This could enable more complex interface structures to be explored, such as those between polycrystalline materials, and enable new scientific conclusions.

2.7 Au and Pt Microstripe Arrays on Quartz

Another strategy I pursued for creating a nanoscale bimetallic interface was to use fabrication techniques since these techniques are already well developed due to their use in the semiconductor industry. My goal for this project was to use metal evaporation combined with lift-off photolithography to generate microscopic, intersecting stripes of Au and Pt on a quartz substrate. The quartz substrate was chosen so that catalysis on the fabricated metal features could be monitored on the microscope using the single-molecule fluorescence technique. Photolithography was chosen since it is relatively fast and inexpensive to implement, once a mask has been made, compared to electron beam lithography. One drawback to using photolithography is that the minimum feature size is limited by the optical resolution for the wavelength of light used in addition to some limitations from the photoresist used, yielding in this case a minimum feature size of ~200 nm. Nonetheless, the method is still useful in creating bimetallic interfaces that can be studied on the microscope since the height of the metal features is determined during an evaporation step and can be set to heights compatible with total internal reflection excitation. Au and Pt were chosen as the two metals to create the interface for the same reason as in the previous section.

2.7.1 Design of Au and Pt Microstripe Arrays

First, the design of the intersecting array was created using the L-Edit Auto-CAD software at Cornell's CNF. The first layer was used to denote where the position markers and the Au features would be deposited and the second layer was used to indicate where the Pt features would be placed. An orthogonal, intersecting array of nine stripes each of Au and Pt was chosen. Each metal had three stripes each

of widths of 250 nm, 500 nm, and 1000 nm that were spaced 7.5 µm apart. This array was repeated in a 3 x 3 grid with spacing of 400 µm between arrays. Also since 4 inch quartz wafers were used, this whole array was replicated in another 3 x 3 grid each spaced 1 inch apart so that 9 samples could be produced per wafer. The schematic diagram of this design is shown in Figure 2.18. Later the wafer would be diced so each 1 square inch piece would have 9 intersecting arrays in the center that could be studied on the optical microscope.

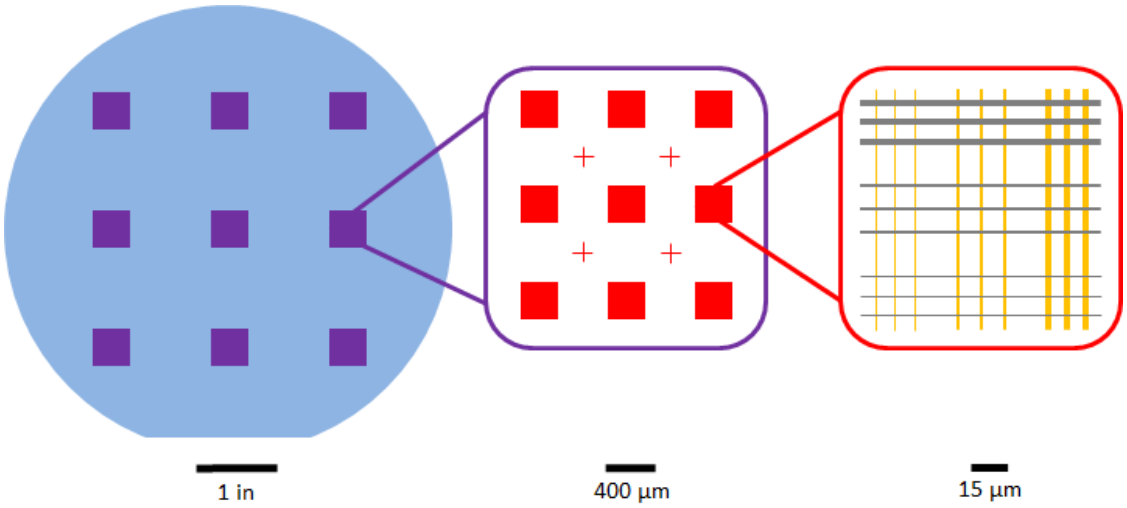

Figure 2.18 Schematic diagram of Au and Pt stripes on a quartz wafer. In the far right box the Au stripes are represented in yellow and the Pt stripes in grey.

2.7.2 Experimental Implementation of Microstripe Arrays

Each layer of the Auto-CAD template was appropriately scaled for use with a 4x reduction stepper and written into separate regions of a blank reticle using the Heidelberg DWL2000 Mask Writer. 1 mm thick quartz wafers were used after an initial attempt using 0.5 mm thick wafers revealed that they were too brittle and broke easily. Additionally, the 1 mm thick quartz wafers were the same thickness as the microscope slides used for making microfluidic reactors for use on the microscope. This common thickness made it easier to align and incorporate the nanofabricated arrays into a flow cell for use on the microscope.

Since robotic systems were used to coat, expose, and develop the wafers, it was necessary to mark the edges and the outermost part of the back of the wafers with a black sharpie since the robotic systems make their alignments based on optical detection and the unmarked quartz alone does not have enough contrast. The Gamma Automatic Coat-Develop tool was used to coat 85 nm of an antireflection coating onto the quartz wafers, followed by 600 nm of UV 210 photoresist. A soft bake was performed for 60 seconds at 130 ^{o}C in close proximity mode. The reticle and coated wafers were aligned to the first layer and exposed using 248 nm light on the ASML 300C DUV 4x reduction stepper. A post exposure bake for 90 seconds at 130 ^{o}C in close proximity mode was performed on the wafers before being developed in the Gamma tool. The developing step used 0.26 N developer using 4 puddles at 120 seconds each. This many iterations of developing ensured that there was sufficient undercut in the antireflection layer, especially since the feature sizes were small. This enabled the liftoff procedure to work smoothly.

A CVC SC4500 electron-gun evaporator was used to deposit Au through the

photoresist onto the wafer. First a 5 nm thick film of Ti was deposited at 0.3 Å/s to serve as an adhesion layer to prevent the Au film from delaminating from the quartz surface. Ti was chosen over Cr as the adhesion layer because Cr more easily forms alloys with Au, and the goal was to study catalysis on a pure gold surface. Next, 26 nm of Au was deposited at 0.3 Å/s. The photoresist was removed by soaking in AZ300T solvent overnight. The wafers were rinsed and dried, and the whole process was repeated for the second layer. 25 nm of Pt was nominally deposited at 0.1 – 0.5 Å/s. Pt is a more difficult material to evaporate and the rate is hard to keep constant. The final photoresist was removed as before. The wafers were coated with a protective layer of photoresist before being cut into 1 inch squares using a dicing saw.

2.7.3 Fabrication Results

An optical dark field image and an SEM image of two of these arrays can be seen in Figure 2.19. As can be seen in the images, the alignment of the two layers are not exact in each case, but there are still intersections between all combinations of the Au and Pt stripes of each size. Also one of the layers shows up much more clearly in both images. This could be due to their actually being a greater or lesser thickness of Pt deposited despite both layers nominally being 25 nm thick. At this point, one piece was incorporated into a flow cell by using epoxy to connect additional pieces of 1 mm thick quartz on either end to make it long enough to span the hole in the microscope stage. As was done before, double sided tape and a coverslip were used to complete the flow channel.

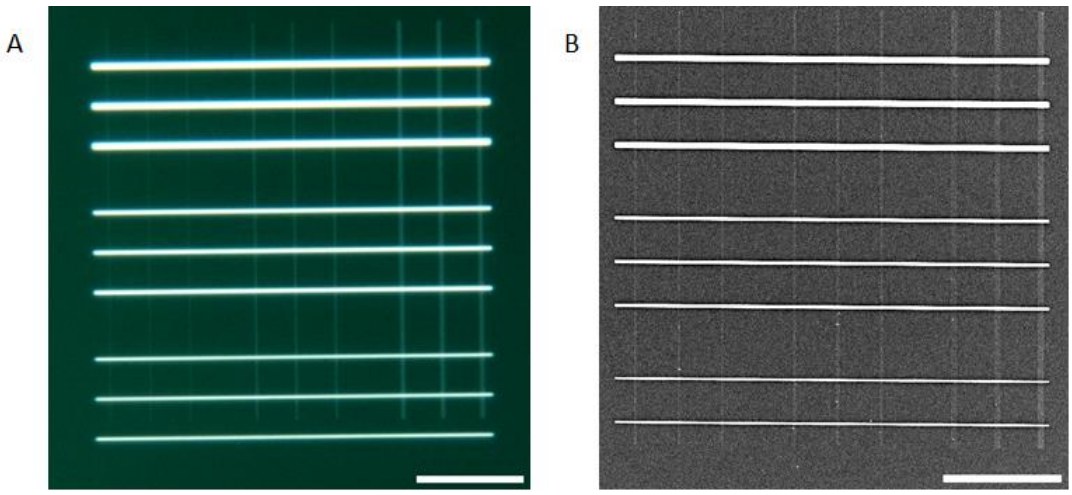

Figure 2.19 Optical dark field image (A) and SEM image (B) of Au and Pt microstripe array. Scale bars are both 20 μm.

2.7.4 Single-molecule Catalysis Measurements on Au and Pt Microstripe Arrays

A Au and Pt microstripe array quartz piece was constructed into a flow channel. It was then mounted on the optical microscope to conduct fluorescence microscopy experiments. Figure 2.20A shows a fluorescence image of the arrays under TIR excitation at 532 nm and emission collected at 580 +/- 30 nm. As can be seen in the images, the Pt stripes also emit light in the same spectral region as the resorufin for which the optical filters were set. As was the case with the electrodeposited rods, there is the possibility of fluorescence quenching on the surface of the metal features. To test for this, 5 nM of resorufin was flowed in and the fluorescence image was retaken as can be seen in Figure 2.20B. The line profiles highlight the differences in fluorescence intensity on and off of the metal stripes. If the fluorescence of the resorufin was quenched there should be a lower relative fluorescence on the metal than off of it. Since the emission from the metal features over the background is the same with and without resorufin present, fluorescence quenching does not seem to be an issue. It is still possible that despite there being 5

nM resorufin in bulk solution, that very little is actually bound to the surface of the metal. Because of experimental limitations the concentration of resorufin cannot be raised much higher. Also without any method to measure surface coverage of the dye, an adsorption isotherm and binding constant cannot be obtained.

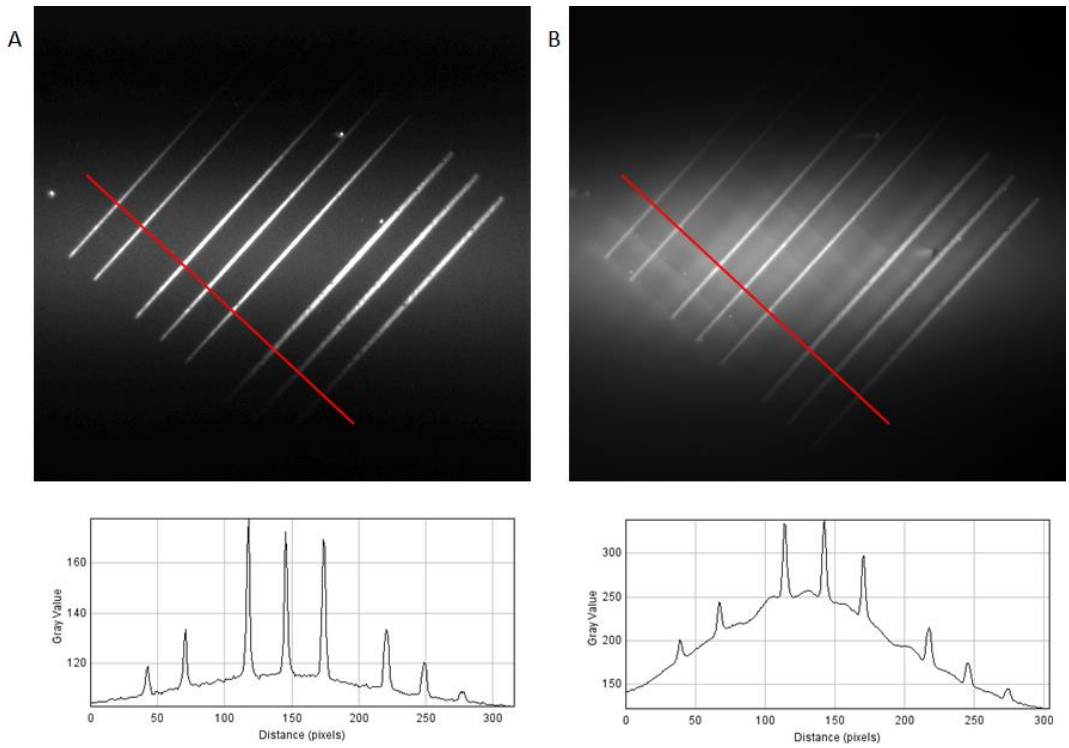

Figure 2.20 Optical fluorescence image of Au and Pt microstripe arrays with only buffer in flow channel (A) and with 5 nM resorufin in flow channel (B).

Next the arrays were used to catalyze amplex red oxidation in the presence of hydrogen peroxide. Since the total amount of catalyst on each quartz square was small, it was not possible to detect catalytic activity at the ensemble scale, thus the single-molecule catalysis measurements were attempted without even knowing if the material was active. First a control fluorescence movie was recorded in which only 60

mM hydrogen peroxide and 10 mM pH 7.3 phosphate buffer were flowed through the channel. Fluorescence movies were then recorded with 5, 20 and 100 nM amplex red in addition.

Since the metal features were large and occupied most of the window, the mainsharpshooter analysis previously used on the nanoparticles was not appropriate since it only looks for fluorescent bursts from small, localized areas of a few pixels in size. This analysis method was used in the previous chapter for the Au nanoparticles. The mainsharpshooter algorithm searches for fluorescent bursts within a small area by monitoring the integrated intensity of that area over time. If too large of an area is chosen, the signal from the fluorescent bursts will be lost in the noise of the surrounding area. To overcome this challenge, iQPALM analysis was used which searches the entire frame for fluorescence signal. However, one drawback to the iQPALM analysis is that it requires the fluorescent spots to be against a dark background. Since the Pt stripes showed up bright in the fluorescence imaging mode, the background was not completely dark. To correct for this, an average image was taken every 2.5 minutes and subtracted from each individual frame. These background subtracted images much more closely resemble a uniform dark background. iQPALM analysis was then performed on these background subtracted movies and the results are shown in Figure 2.21 with the analysis from the control frames plotted in A and from the 5 nM AR catalysis frames in B. As can be seen, there are many more fittings localized on the metal features, however, there was no appreciable difference in the frequency of events coming from the control versus the three catalysis conditions. Additional analysis on the control frames showed that the bright pixels where the metal features were had greater noise than the background

pixels. This means it is more likely to have a higher intensity pixel on the metal than off of it, even in the absence of blinking from fluorescent molecules. This could be the reason for the majority of the localizations landing on the stripes. Regardless of the threshold used, the frequency of events are similar in both control and catalysis conditions. Additionally, several points along the bright metal stripes were taken and analyzed using the localized mainsharpshooter analysis described earlier. However the fluorescence intensity versus time trajectories from these points only show noise, meaning that the events picked up in iQPALM were noise and the threshold was too low. This means that either the metal stripes are not catalytically active or that the fluorescence signal from the surface adsorbed product molecules cannot be detected.

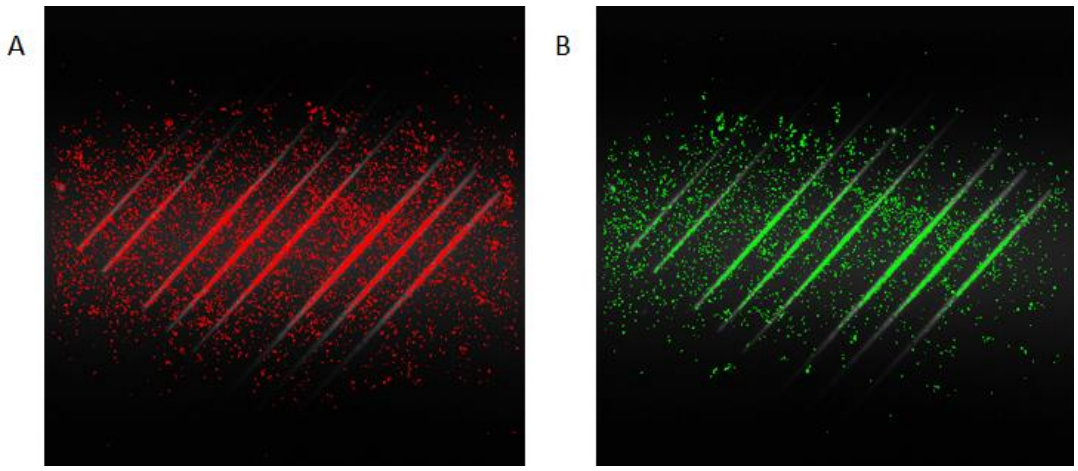

Figure 2.21 Fluorescence image of Au and Pt microstipe array with control fittings overlaid in red (A) and with fittings resulting from catalysis conditions in green(B).

2.7.5 Challenges Remaining for Microstripe Arrays

One of the challenges remaining for this project is that ensemble activity still needs to be measured. Previously the ensemble activity was measured by placing the

one square inch quartz piece with the metal stripes into a beaker with the reaction solution. Over a period of many hours and after one night, the solution was removed to have its visible spectrum recorded, which did not change during this time period. Another more sensitive way to measure the ensemble activity would be to use the flow cell, introduce the reaction solution, then stop the flow and use fluorescence microscopy to look for an increase in the background due to fluorescent product accumulation. Since this uses a much smaller volume, it should be easier to detect activity.

Another challenge is the detection of single fluorescent product molecules. Previously for the larger Au nanoparticles and the electrodeposited rods, a mesoporous silica shell was added to aid in fluorescence detection. That growth process was monitored and characterized by TEM. Since these metal stripes are connected to the quartz substrate, they cannot be imaged in TEM. The sample could be carbon coated and imaged using SEM, but the resolution is not high enough to see if there is a porous structure, and the carbon coating would have to be burned off after imaging, before proceeding to the next step. Another possibility was to spin cast a thin film of mesoporous silica over the whole structure.

Over 20 years ago Kresge et al. found that mesoporous silica could be formed by mixing silica precursors with different surfactants to control the final structure after baking.[30,31] Since then the method has been modified and adapted to make mesoporous silica thin films by making a sol-gel precursor solution and spin casting it onto a substrate. I reproduced one such procedure in which the sol-gel precursor was made from deionized water, ethanol, hydrochloric acid, cetyltrimethylammonium bromide (CTAB), and tetraethylorthosilane (TEOS) in place of tetramethylorthosilane

(TMOS).[32] The ethanol is a better solvent for the CTAB and is also more volatile. As the solution is spun, the ethanol evaporates faster causing the CTAB to exceed its critical micelle concentration in water, which leads to the ordered structure formation.

I prepared the sol-gel and spin cast it onto chips of a silicon wafer with a native oxide present at 6,000 RPM. Then it was baked to solidify the structure and remove the surfactant. The silicon substrate was used to test the synthetic procedure instead of quartz or glass so that the film thicknesses could be characterized by ellipsometry which requires a change in refractive index between the layers to work. The resulting thickness was just over 200 nm. Using the initial precursor solution and increasing the rotational casting rate to 10,000 RPM did not achieve a significant change in film thickness. Since ~100 nm thick film would be ideal, I diluted the precursor solution by a factor of two in ethanol and recast it at 6,000 RPM, which resulted in a thickness of 120 nm. An important point is that by changing the precursor solution the resulting pore structure could be affected.

I also made and cast a slightly different sol using the same precursors but in different ratios according to another published procedure.[33] Both of these sols used CTAB as the surfactant to direct the porous structure. The nature of that structure was still unclear without further characterization. The ratio of reagents in the precursor solution can affect the final morphology. In order for the films to be useful, they must allow molecules to diffuse from one face to the other. A test was conducted in which these two films were cast on indium-doped tin oxide (ITO) coated quartz slides. They were connected as the cathode in an electrochemical cell containing the Au bath for electrochemical deposition. A negative voltage was applied but no current was passed, whereas on an uncoated ITO slide 64 $\mu A/cm^2$ was passed, indicating that these

silica films were insulating the ITO from the solution.

Following a third procedure, I made another precursor sol in which the surfactant used was a triblock copolymer, F127, that consists of end blocks of ethylene oxide with a center block of propylene oxide.[34] The ratio of the reactants was chosen to give a rhombohedral structure which will have contintuous pores from one face of the film to the other. Another different feature about this procedure compared to the other ones was that the spin casting was performed under ~60-70% humidity to slow the evaporation rate. Using our equipment this condition was best replicated by pouring boiling water into the bottom of the spin coater bowl before use and coving the top lid vent with a wet paper towel. The sol was cast onto an ITO coated quartz slide at 4,500 RPM. After a long annealing procedure followed by calcination, the slide was test for cathodic current in the Au deposition bath. A current resulted in which 16 $\mu A/cm^2$ was passed, thus confirming the continuous structure of the pores from substrate to the top face. Although the thickness of this film was not measured by ellipsometry, a flow cell of 40 nm spherical Au covered by this continuously porous silica film was prepared and used to record a fluorescence movie under catalytic conditions. After analysis, some of the 40 nm Au particles could be imaged by their catalytic activity, however there were other localized spots that showed catalytic-like behavior where no Au particles were present. This result shows that using spin cast porous silica thin films is promising for use in aiding fluorescence detection, although more work needs to be done to understand where the false signals originate from. In the future this thin film method could be applied to the Au and Pt microstripe arrays to enable detection of the catalytic activity.

Additionally, I also tried using a PMMA thin film to aid in fluorescence

detection. A thin film was cast at 2,000 RPM from 5 g/L of M_w = 15,000 PMMA in chloroform. After casting it was annealed for 3 hours at 145 ^oC, and the resulting film thickness was 64 nm as measured by ellipsometry. A new microscope slide flow cell was constructed in which 40 nm spherical Au particles were dispersed and then covered with the PMMA film described above. A fluorescence movie was recorded under catalytic conditions. However, upon analysis, the underlying Au particles cannot be imaged based on their catalytic activity, thus the PMMA film is unlikely to aid in fluorescence detection.

2.8 Au/Pd Core-shell Nanoparticles

Using colloidal nanoparticle synthesis, I also made Au/Pd core-shell nanorods to investigate the effect on catalytic activity due to the presence of a second metal on the core particle. Unlike the other catalyst schemes where an exposed bimetallic junction was the region of interest to study, for this set of experiments the interface between the two metals was buried. Except for cases of incomplete, sub-monolayer coverage of a Pd shell, this means that any direct measurement of activity at the interface is impossible. However, the effect of the interface, although buried, can still be probed by repeating catalytic activity measurements as a function of Pd shell thickness for a fixed sample of Au cores. This experimental design also has the benefit of being able to examine the effect of the interface at a fixed distance away since the core metal will still affect the properties of the shell by modifying it electronic structure and introducing strain. At low shell thickness the effect of the interface will be most pronounced, and at very high shell thicknesses, the particle should just behave as if it were completely Pd since the Au interface will be too far

removed from the surface to have an effect. Another benefit of this experimental design is that the spatial resolution for examining the interfacial effect is determined by the sample preparation and characterization by TEM which has a couple of nm resolution compared to using single-molecule fluorescence microscopy which has ~30 nm spatial resolution.

Au nanorods were chosen as the core particles because they have already been studied as shown in the last chapter and also by Zhou et al.[35] The rods are good as cores since they have a narrow diameter distribution which means that the Pd growth can be measured by comparing the diameter before and after it has been added. Another advantage of using rods as cores instead of spherical particles is that the rods show an activity gradient along its length with higher activity in the center and dropping off towards the ends.[35] This activity gradient is proposed to originate from an underlying defect density gradient arising from the rods' initial growth kinetics. The experiment of imaging catalytic activity of core-shell bimetallic rods also allows for the measurement of the activity gradient as a function of Pd shell thickness. This can lead to an understanding of how the Pd overgrowth occurs and what effect it has on catalytic activity. For example, if the shell growth is epitaxial, then at low shell coverage, the surface structure of the Au can be transferred to the Pd and a similar gradient might be observed.

2.8.1 Colloidal Growth and Purification of Au Nanorods

The Au nanorods were produced using seed mediated growth following a modified procedure from Murphy et al.[36] I produced Au seeds by taking 20 mL of

aqueous solution containing 0.25 mM in both chloroauric acid and trisodium citrate and adding 0.6 mL of freshly prepared 0.1 M sodium borohydride. This addition of excess reducing agent quickly results in the formation of small, sub-5 nm Au particles. The Au seed solution was left to sit for several hours so that the excess borohydride could decompose. After this time the seed solution could be used for up to a couple of months without affecting the final rod morphology.

2 L of Au growth solution was prepared by making a 40 ^{o}C solution containing 0.1 M CTAB and 0.25 mM chloroauric acid. Aggregation can occur if the chloroauric acid is added to the CTAB solution at too high of a concentration so this mixture was made by combining 1 L of 0.2 M CTAB with 1 L of 0.5 mM chloroauric acid, both at 40 ^{o}C. This mixture has a dark orange color due to the Au-CTAB complex. To this solution 1.12 mL of 1 M ascorbic acid was added and stirred in, which causes the gold to go from the +3 to the +1 oxidation state, and the solution becomes clear. 90 mL of this solution was removed and put in one bottle, and 180 mL was removed and put in another. 10 mL of the Au seeds were added to the bottle with 90 mL of Au growth solution and stirred. After around 10-30 seconds 20 mL of this mixture was added to the bottle with 180 mL of Au growth solution and stirred in. After ~30 seconds all of this solution was added to the large batch of Au growth solution and stirred in. This solution was divided into two 1 L glass bottles and held at 40 ^{o}C overnight which produces a mixture of mostly faceted pseudo-spherical particles but also some rods and a lesser amount of platelets.

After the particles were produced, the rods needed to be separated from the majority of the spherical particles. After sitting overnight, the solution was slowly poured out of the glass bottles and into a beaker for storage. 10 mL of water was

added to the empty bottle and swirled to extract the Au rods that had adsorbed onto the bottom of the glass bottle. This solution is brown in color as compared to the solution that had been poured off that is reddish-purple in color. The Au particle mixture solution can be poured back into the glass bottles and left to sit overnight so that more rods can be extracted the next day. At and after day 4 of repeating this, the rod yield significantly decreases. The main differences between this and the previously published procedure are that the method I used is greatly scaled up to produce higher rod yields and the purification method by glass adsorption results in much higher rod purity. This purification method is an extension of the previously reported method in which the rods are obtained by taking the bottommost fraction of the growth solution. The rods produced using this method are shown in Figure 2.22A.

Although the procedure described above is reliable, the rods resulting from it average just under 400 nm in length. Longer rods were more desirable since in order to be able to measure the activity gradient along the rod, they need to be much longer than the spatial resolution of the measurement. I tried two additional procedures to increase the Au rods' length. In the first method, a 10% aliquot of the previously produced Au rods were used as seeds for an additional seeded growth in 200 mL of Au growth solution. The resulting rods are indeed longer than the initial ones but there is also a significant increase in diameter from 21 to ~80 nm. Also the ends of the new rods are more faceted. These rods can be seen in Figure 2.22B.

For the second method the ratio of the final dilution into the Au growth solution was changed. Three trials were conducted in which the final dilution ratio was increased to 3, 5, and 10 times what the original procedure called for. The rods resulting from the 3x increased dilution averaged 512 nm in length, while those from

the 5x batch averaged 567 nm in length. Both had similar diameters to the original. The rods resulting from the 10x batch resembled those resulting from undergoing an additional growth step in that they were longer but also much wider. The procedure used to make the 5x batch was used in all following Au rod syntheses, and the rods can be seen in Figure 2.22C. However much of the following work on the AuPd core shell synthesis was performed on the original Au rods, which happened before this method was developed.

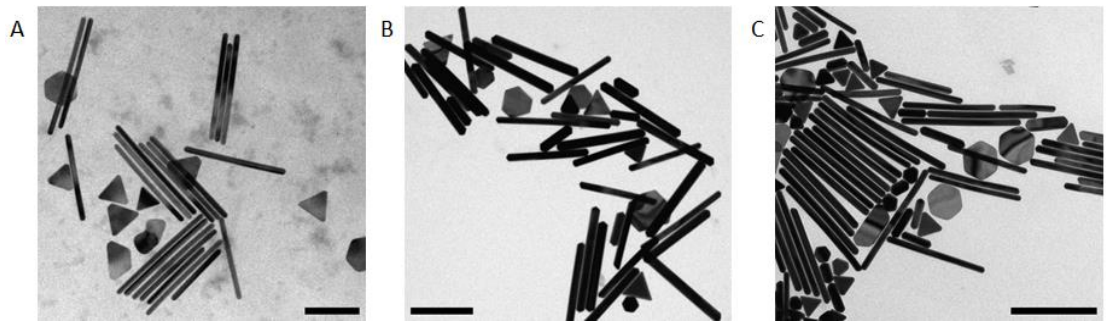

Figure 2.22 TEM micrographs of the original Au nanorods resulting from (A) the original procedure, (B) from undergoing and additional growth step, and (C) from having the last dilution ratio increased by a factor of five. The scale bar in A is 200 nm and in B and C they are 500 nm.

2.8.2 Growth of Pd Shell on Au Nanorods as Cores

In order to add a Pd shell onto the Au rods shown above, a Pd growth solution was prepared based of the method of Li.[37] This method was chosen because it also relies on CTAB as the stabilizing ligand, which means that ligand exchange on the Au rods would not be required. The Pd growth solution consisted of 0.5 mM $PdCl_2$, 50 mM HCl, 2.3 mM ascorbic acid, and 0.1 M CTAB. This solution was made fresh right before it was used because if left overnight, Pd particles will form even without seeds present. Also it was made and kept at 40 ^{o}C to keep the CTAB soluble.

Varying amounts of this solution were mixed with a fixed amount of Au rods. The amount of Au rods was defined by the concentration of the Au rod solution as measured by its absorption peak near 500 nm through a 1 cm path length cell and an appropriate volume in mL so that the product of the two equaled 3.625. This way of defining one batch was done so that the same amount of Au rods could be used resulting from a different synthesis with a slightly different concentration. The Au rod solution and the Pd growth solution were mixed and kept at 40 ^{o}C for several hours before the AuPd, core-shell rods were collected by centrifugation, and characterized by TEM. The sample resulting from addition of 10 mL of Pd growth solution to one batch of Au rods is shown in Figure 2.23. As can be seen, the outer Pd shell shows up with a lower contrast as compared with the Au cores. A calibration curve was created by measuring the amount of shell added versus the amount of Pd growth solution used. The results are shown in Figure 2.24. For the larger shell samples, the Pd growth is measured by an increase in the cross sectional area to give a linear calibration, but for the thin shell range it is simply measured by the particle diameter. For the cross sectional area gained versus Pd growth solution plot, the thin shell values deviate from the trend of the thicker shell values. A possible reason for these points lying lower could be due to the Pd having preferential growth on the ends of the rods. By changing the kinetics of the Pd shell growth this effect could be mitigated since Li showed that the morphology of the Pd shell on spherical Au particles could be manipulated by changing the growth kinetics.[37] However, this project proceeded with the conditions described above.

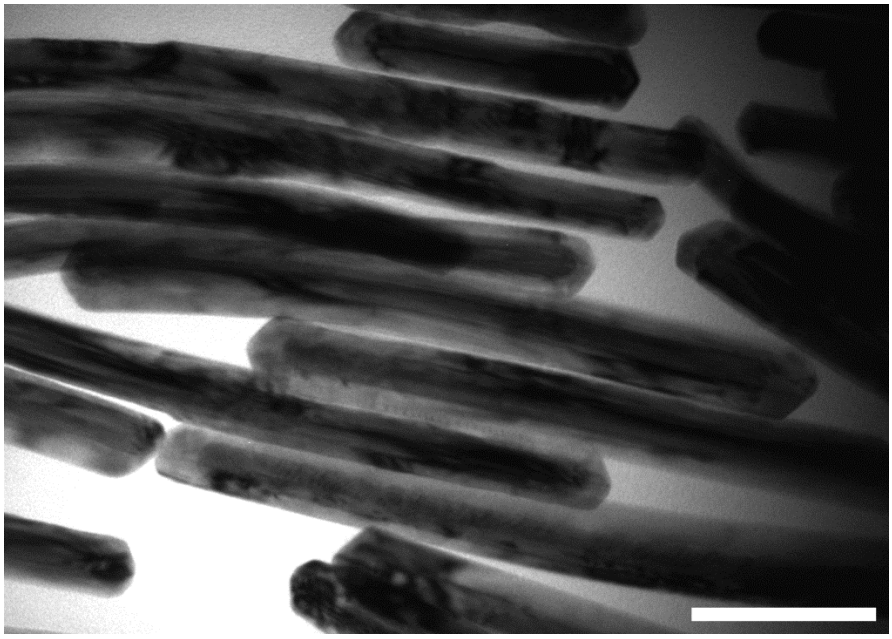

Figure 2.23 TEM micrograph of AuPd, core-shell nanoparticles resulting from addition of 10 mL of Pd growth solution to one batch of Au rods. The scale bar is 100 nm.

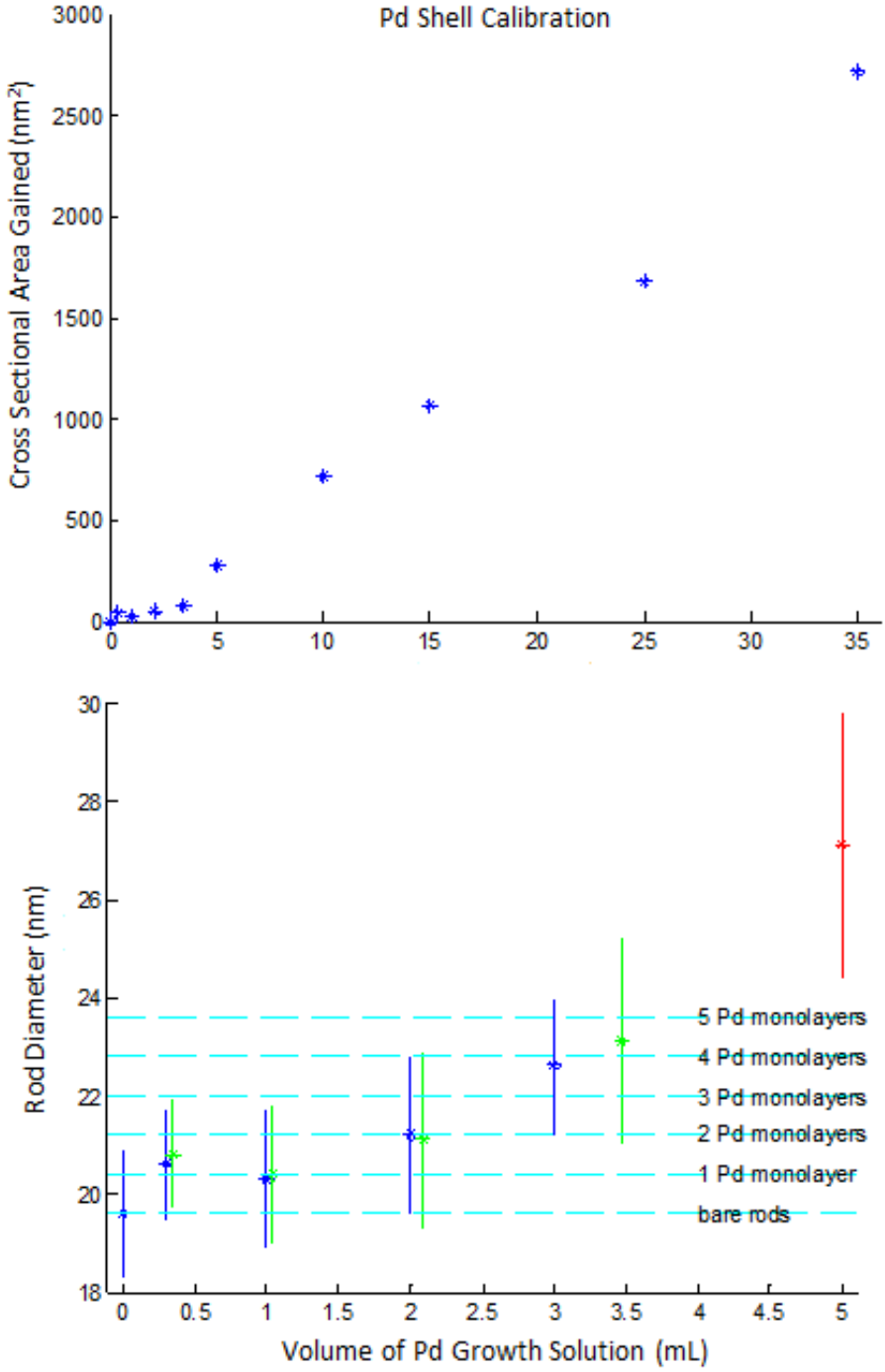

Figure 2.24 Calibration plot for Pd shell overgrowth versus amount of Pd growth solution used for a fixed batch of Au rods as cores. In the lower plot the horizontal dashed lines represent the rod diameters expected for the incremental values for Pd monolayers. The different colors represent syntheses that were performed on the same Au rod core samples.

Another interesting observation in the thin Pd shell range was the formation of bent AuPd core shell rods as can be seen in Figure 2.25. The reason for this behavior is most likely due to a combination of lattice mismatch and preferential growth of the Pd on one side of the Au rod. Since Pd has smaller lattice spacing than Au, compression strain will be introduced on the Au as the Pd is added. If the growth is unbalanced, the rod bends towards the side with more Pd. The concentration of the ligand, CTAB, was changed between 0 and 0.1 M, and the growth was repeated to test if the Pd shell could be directed more symmetrically or more to one side. At 0 CTAB, the Pd does not grow onto the Au rods and large Pd aggregates form, and at non-zero CTAB concentration, there is always a similar population of slightly bent rods. Additional work could be pursued in which the reaction kinetics are changed to try to control the amount of bent rods. These rods could be useful to study at the single particle level to examine the effects of induced strain on catalytic activity. Although the diameter of the rod is close to the spatial resolution of the single-molecule imaging technique, it may be possible to measure the difference in catalysis on the inside and outside of the bent rods where the strains on the Au are in opposite directions. Additionally, the Pd growth could be performed on the larger diameter Au rods shown in Figure 2.22B to see if those will also bend. The wider core will make it stronger and less likely to bend, but the increased width also will give spatial resolution across the width of the rod.

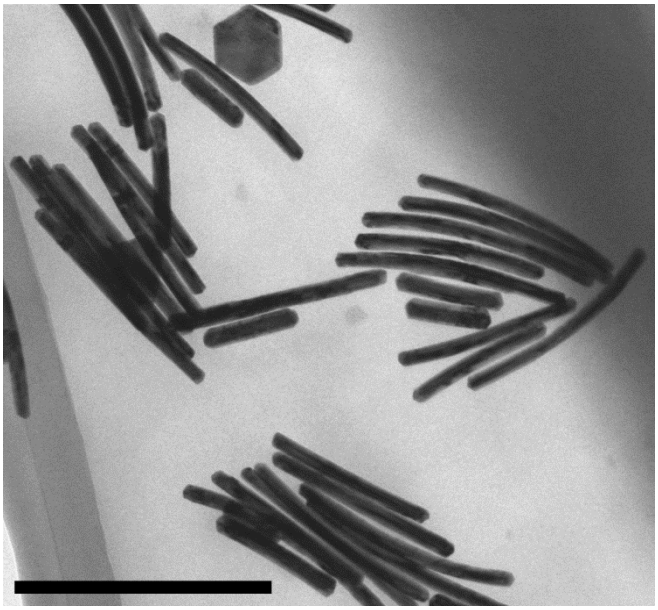

Figure 2.25 TEM micrograph of AuPd core-shell particles resulting from the addition of 5 mL of Pd growth solution to one batch of Au rods. The scale bar is 500 nm.

2.8.3 Modified Methods for Mesoporous Silica Growth

Again, as before, the AuPd core-shell particles were tested and confirmed as catalysts by measuring ensemble activity. The bare particles were also used as catalysts for single-molecule measurements, but there was not any fluorescence signal detected. The strategy of using a mesoporous silica shell to enable fluorescence detection was pursued as described before. However, for these particles, I also utilized a modified synthetic procedure in which steps were combined to yield mesoporous silica after the growth step without the need for etching. Previous reports in the literature show that CTAB can direct the structural evolution of silica during its growth.[30,38,39] I modified these procedures to perform a shell growth that only has one 30-minute step and yields mesoporous silica. Half a batch of AuPd rods shown in Figure 2.25 were mixed in a 20 mL solution of 50 mM CTAB, 50% vol. water and

ethanol. To this solution, 100 µL of 0.1 M NaOH and 300 µL of 10% tetraethylorthosilane (TEOS) were added. The solution was stirred for 30 minutes and the particles recovered by centrifugation. These conditions lead to fast growth kinetics which were necessary since a high nucleation rate was necessary since the particles had not been functionalized. However, these conditions also led to many multi-core particles and a non-conformal coating of the shell to the core. The resulting particles are shown in Figure 2.26. After calcination at 500 ^{o}C for one hour to remove the CTAB, the particles are catalytically active when measured at the ensemble level. However due to the multi-core issue and the non-conformal coating, this method was not used for particles being studied at the single-particle level.

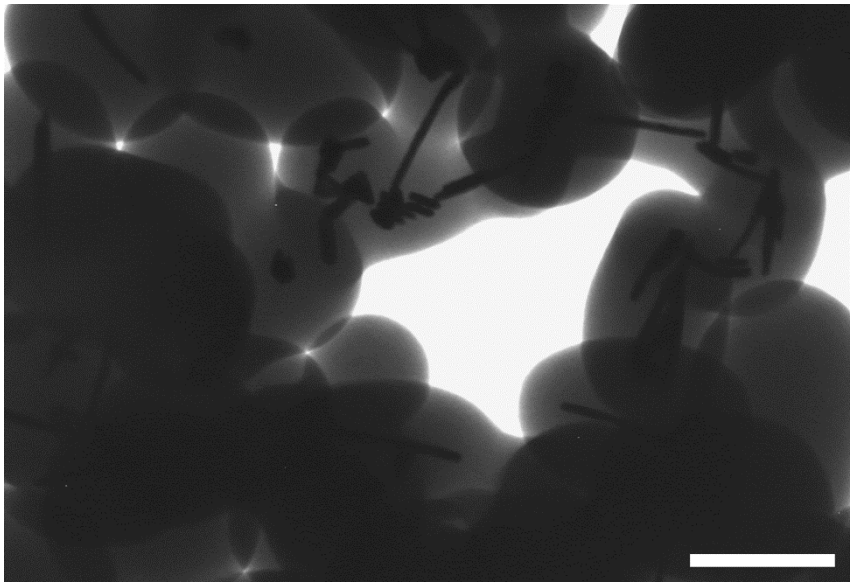

Figure 2.26 TEM micrograph of fast one-step mesoporous silica growth. The scale bar is 500 nm.

Another method I experimented with for the shell growth was more similar to the traditional two-step silica shell growth used on the spherical Au particles, except

that instead of centrifuging the particles and changing solvents between the slow and the fast growth steps, the procedure was continued in the original pot without purification or solvent exchange. For this method 3 batches of AuPd cores were each placed in 25 mL of water. To these 350 μL of $1:10^4$ MPTMS:ethanol was added to functionalize the surface of the particles with a silane group for further silica growth. After one night, 0.5 mL of 0.5% wt. of pH 11.1 sodium silicate solution was added, which initiates a slow silica growth on the functionalized particle surface. After another night 0.5, 1.0, or 1.5 mL of 10% vol. TEOS in ethanol solution was added to each batch and left for one more night. The particles were recovered by centrifugation and characterized by TEM. Surprisingly, regardless of the amount of TEOS added, all three batches had silica shell thicknesses of just over 40 nm. Also if the particles were left for more than one night, the silica shell thickness did not change. An additional silica growth step was attempted using the already coated particles as seeds, but the shell thickness remained the same. These particles were etched in the presence of CTAB as were the spherical Au particles with a silica shell to form the porous structure. The $AuPdSiO_2$ core-shell-shell particles can be seen after the one-pot growth step in Figure 2.27A, and after etching in B. The waviness in the contrast of the shell indicates that pores have been formed. At this point the particles were calcined at 500 ^oC for an hour to remove the ligands. This process causes the Pd to oxidize which is no longer catalytic. The particles were briefly treated with a solution of sodium borohydride to reduce the PdO back to metallic Pd. The $AuPdmSiO_2$ ($mSiO_2$ = mesoporous silica) core-shell-shell particles were confirmed to be catalytically active with ensemble testing, which further validates that the pore structure reached the AuPd particle.

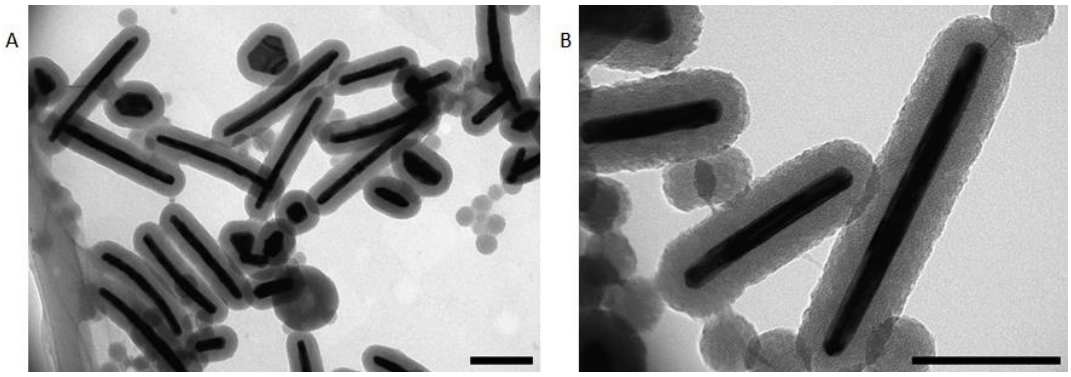

Figure 2.27 TEM micrographs of one-pot silica shell growth on AuPd particles (A) and after etching in the presence of CTAB to form the mesoporous structure (B). Both scale bars are 200 nm.

2.8.4 Challenges Remaining for AuPd Core-shell Particles

Even though the AuPdmSiO_2 particles are catalytically active for ensemble measurements, single particle catalysis data was not able to be obtained. It is likely that more work needs to be done with the mesoporous silica shell so that it can enable fluorescence detection of the product molecules. However, another member of the Chen lab has been working with Pd nanorods synthesized by a hydrothermal method and has successfully obtained preliminary single-molecule catalytic data by coating the particles with a mSiO_2 shell. Additionally, for the samples with thin Pd shells, high resolution TEM characterization would be helpful to better understand the non-uniform coverage of the Pd shell. This could enable better understanding of how it contributes to the bending of the rods and also to how it affects catalytic activity. Future work could be performed to try to synthesize wider AuPd bent rods, and also the kinetics of the Pd shell growth could be manipulated by changing temperature, concentrations, ligands, and reducing agents to see if other morphologies of AuPd

core-shell particles are possible, and what effect they have on catalytic performance.

2.9 References

(1) Wang, D.; Li, Y.: Bimetallic Nanocrystals: Liquid-Phase Synthesis and Catalytic Applications. *Advanced Materials* **2011**, *23*, 1044-1060.

(2) Yu, W.; Porosoff, M. D.; Chen, J. G.: Review of Pt-based bimetallic catalysis: from model surfaces to supported catalysts. *Chem Rev* **2012**, *112*, 5780-817.

(3) Dal Santo, V.; Gallo, A.; Naldoni, A.; Guidotti, M.; Psaro, R.: Bimetallic heterogeneous catalysts for hydrogen production. *Catalysis Today* **2012**, *197*, 190-205.

(4) Sankar, M., Dimitratos Nikilaos, Miedziak, Peter J., Wells, Peter P., Kiely Christopher J., Hutchings, Graham J.: Designing Bimetallic Catalysts for a Green and Sustainable Future. *Chemistry Society Reviews* **2012**, *41*, 8099-8139.

(5) Ferrando, R.; Jellinek, J.; Johnston, R. L.: Nanoalloys: From Theory to Applications of Alloy Clusters and Nanoparticles. *Chem Rev* **2008**, *108*, 845-910.

(6) Mott, D.; Luo, J.; Njoki, P. N.; Lin, Y.; Wang, L.; Zhong, C.-J.: Synergistic activity of gold-platinum alloy nanoparticle catalysts. *Catalysis Today* **2007**, *122*, 378-385.

(7) Lee, H.; Habas, S. E.; Somorjai, G. A.; Yang, P.: Localized Pd Overgrowth on Cubic Pt Nanocrystals for Enhanced Electrocatalytic Oxidation of Formic Acid. *J Am Chem Soc* **2008**, *130*, 5406-5407.

(8) Liu, F.; Lee, J. Y.; Zhou, W.: Template Preparation of Multisegment PtNi Nanorods as Methanol Electro-Oxidation Catalysts with Adjustable Bimetallic Pair Sites. *The Journal of Physical Chemistry B* **2004**, *108*, 17959-17963.

(9) Cui, C.-H.; Yu, J.-W.; Li, H.-H.; Gao, M.-R.; Liang, H.-W.; Yu, S.-H.:

Remarkable Enhancement of Electrocatalytic Activity by Tuning the Interface of Pd–Au Bimetallic Nanoparticle Tubes. *ACS Nano* **2011**, *5*, 4211-4218.

(10) Alayoglu, S.; Tao, F.; Altoe, V.; Specht, C.; Zhu, Z.; Aksoy, F.; Butcher, D. R.; Renzas, R. J.; Liu, Z.; Somorjai, G. A.: Surface Composition and Catalytic Evolution of Au x Pd1−x (x = 0.25, 0.50 and 0.75) Nanoparticles Under CO/O_2 Reaction in Torr Pressure Regime and at 200 °C. *Catalysis Letters* **2011**, *141*, 633-640.

(11) Al-Mawlawi, D.; Liu, C. Z.; Moskovits, M.: Nanowires formed in anodic oxide templates. *Journal of Materials Research* **1994**, *9*, 1014-1018.

(12) C. Hulteen, J.; Martin, C. R.: A general template-based method for the preparation of nanomaterials. *Journal of Materials Chemistry* **1997**, *7*, 1075-1087.

(13) Chen, P., Zhou, Xiaochun, Andoy, Nesha May, Han, Kyu-Sung, Choudhary, Eric, Zou, Ningmu, Chen, Guanqun, Shen, Hao: Spatiotemporal Catalytic Dynamics within Single Nanocatalysts Revealed by Single-molecule Microscopy. *Chemistry Society Reviews* **2014**, *43*, 1107.

(14) Han, K. S.; Liu, G.; Zhou, X.; Medina, R. E.; Chen, P.: How Does a Single Pt Nanocatalyst Behave in Two Different Reactions? A Single-Molecule Study. *Nano Letters* **2012**, *12*, 1253-1259.

(15) Martin, B. R.; Dermody, D. J.; Reiss, B. D.; Fang, M.; Lyon, L. A.; Natan, M. J.; Mallouk, T. E.: Orthogonal Self-Assembly on Colloidal Gold-Platinum Nanorods. *Advanced Materials* **1999**, *11*, 1021-1025.

(16) Wang, Y.; Hernandez, R. M.; Bartlett, D. J.; Bingham, J. M.; Kline, T. R.; Sen, A.; Mallouk, T. E.: Bipolar Electrochemical Mechanism for the Propulsion of Catalytic Nanomotors in Hydrogen Peroxide Solutions†. *Langmuir* **2006**, *22*, 10451-10456.

(17) Qin, L.; Banholzer, M. J.; Xu, X.; Huang, L.; Mirkin, C. A.: Rational Design and Synthesis of Catalytically Driven Nanorotors. *J Am Chem Soc* **2007**, *129*, 14870-14871.

(18) *Modern Electroplating*; Schlesinger, M., Paunovic, Milan, Ed.; Wiley, 2010, pp 736.

(19) Keller, F., Hunter, M. S., Robinson, D. L.: Structural Features of Oxide Coatings on Aluminum. *Journal of The Electrochemical Society* **1953**, *100*, 411.

(20) Diggle, J. W.; Downie, T. C.; Goulding, C. W.: Anodic oxide films on aluminum. *Chem Rev* **1969**, *69*, 365-405.

(21) Gerein, N. J.; Haber, J. A.: Effect of ac Electrodeposition Conditions on the Growth of High Aspect Ratio Copper Nanowires in Porous Aluminum Oxide Templates. *The Journal of Physical Chemistry B* **2005**, *109*, 17372-17385.

(22) Katzmann, J.; Härtling, T.: Nanorod Formation by Photochemical Metal Deposition in Nanoporous Aluminum Oxide Templates. *The Journal of Physical Chemistry C* **2012**, *116*, 23671-23675.

(23) Masuda, H., Satoh, M.: Fabrication of Gold Nanodot Array Using Anodic Porous Alumina as an Evaporation Mask. *Japanese Journal of Applied Physics* **1996**, *35*, L126.

(24) Choi, J.; Sauer, G.; Nielsch, K.; Wehrspohn, R. B.; Gösele, U.: Hexagonally Arranged Monodisperse Silver Nanowires with Adjustable Diameter and High Aspect Ratio. *Chemistry of Materials* **2003**, *15*, 776-779.

(25) Zheng, W.; He, L.: Distance-Dependent Fluorescence Quenching of Conjugated Polymers on Au/Ag Striped Nanorods. *The Journal of Physical Chemistry C* **2010**, *114*, 17829-17835.

(26) Reineck, P.; Gómez, D.; Ng, S. H.; Karg, M.; Bell, T.; Mulvaney, P.; Bach, U.: Distance and Wavelength Dependent Quenching of Molecular Fluorescence by Au@SiO_2 Core–Shell Nanoparticles. *ACS Nano* **2013**, *7*, 6636-6648.

(27) Tian, M.; Wang, J.; Kurtz, J.; Mallouk, T. E.; Chan, M. H. W.: Electrochemical Growth of Single-Crystal Metal Nanowires via a Two-Dimensional Nucleation and Growth Mechanism. *Nano Letters* **2003**, *3*, 919-923.

(28) Young, T. F.; Chang, J. F.; Ueng, H. Y.: Study on annealing effects of Au thin films on Si. *Thin Solid Films* **1998**, *322*, 319-322.

(29) Bolk, A.: Kirkendall effect and diffusion in the gold-platinum system—II: The concentration penetration curves and the diffusion coefficients. *Acta Metallurgica* **1961**, *9*, 643-652.

(30) Kresge, C. T.; Leonowicz, M. E.; Roth, W. J.; Vartuli, J. C.; Beck, J. S.: Ordered mesoporous molecular sieves synthesized by a liquid-crystal template mechanism. *Nature* **1992**, *359*, 710-712.

(31) Beck, J. S., Vartuli, J. C., Roth, W. J., Leonowicz, M. E., Kresge, C. T., Schmitt, K. D., Chu, C. T-W., Olson, D. H., Sheppard, E. W., McCullen, S. B., Higgins, J. B., Schlenker, J. L.: A New Family of Mesoporous Molecular Sieves Prepared with Liquid Crystal Templates. *J Am Chem Soc* **1992**, *114*.

(32) Fu, Y.; Ye, F.; Sanders, W. G.; Collinson, M. M.; Higgins, D. A.: Single Molecule Spectroscopy Studies of Diffusion in Mesoporous Silica Thin Films. *The Journal of Physical Chemistry B* **2006**, *110*, 9164-9170.

(33) Nishiyama, N.; Tanaka, S.; Egashira, Y.; Oku, Y.; Ueyama, K.: Enhancement of Structural Stability of Mesoporous Silica Thin Films Prepared by Spin-Coating. *Chemistry of Materials* **2002**, *14*, 4229-4234.

(34) Lee, U. H.; Yang, J.-H.; Lee, H.-j.; Park, J.-Y.; Lee, K.-R.; Kwon, Y.-U.: Facile and adaptable synthesis method of mesostructured silica thin films. *Journal of Materials Chemistry* **2008**, *18*, 1881.

(35) Zhou, X.; Andoy, N. M.; Liu, G.; Choudhary, E.; Han, K.-S.; Shen, H.; Chen, P.: Quantitative super-resolution imaging uncovers reactivity patterns on single nanocatalysts. *Nat Nano* **2012**, *7*, 237-241.

(36) Murphy, C. J.; Thompson, L. B.; Chernak, D. J.; Yang, J. A.; Sivapalan, S. T.; Boulos, S. P.; Huang, J.; Alkilany, A. M.; Sisco, P. N.: Gold nanorod crystal growth: From seed-mediated synthesis to nanoscale sculpting. *Current Opinion in Colloid & Interface Science* **2011**, *16*, 128-134.

(37) Li, J.; Zheng, Y.; Zeng, J.; Xia, Y.: Controlling the size and morphology of Au@Pd core-shell nanocrystals by manipulating the kinetics of seeded growth. *Chemistry* **2012**, *18*, 8150-6.

(38) Gorelikov, I., Matsuura, Naomi: Single-Step Coating of Mesoporous Silica on Cetyltrimethyl Ammonium Bromide-Capped Nanoparticles. *Nano Letters* **2008**, *8*, 5.

(39) Nooney, R. I.; Thirunavukkarasu, D.; Chen, Y.; Josephs, R.; Ostafin, A. E.: Self-Assembly of Mesoporous Nanoscale Silica/Gold Composites. *Langmuir* **2003**, *19*, 7628-7637.